Cavity enhanced optical processes in microsphere resonators

DISSERTATION

zur Erlangung des akademischen Grades
doctor rerum naturalium
(Dr. rer. nat.)
im Fach Physik

eingereicht an der
Mathematisch-Naturwissenschaftlichen Fakultät I
Humboldt-Universität zu Berlin

von
Herr Dipl.-Phys. Andrea Mazzei
geboren am 24.03.1978 in Pescia (PT) - Italien

Präsident der Humboldt-Universität zu Berlin:
Prof. Dr. Christoph Markschies

Dekan der Mathematisch-Naturwissenschaftlichen Fakultät I:
Prof. Dr. Christian Limberg

Gutachter:

1. Prof. Dr. Oliver Benson
2. Prof. Dr. Vahid Sandoghdar
3. Prof. Dr. Thomas Elsässer

eingereicht am:	10. Februar 2007
Tag der mündlichen Prüfung:	19. April 2007

Abstract

Optical microcavities play an important role in a manifold of optical processes, ranging from Cavity Quantum Electrodynamics (QED) to photonics and sensing. A very efficient way to trap light is by means of total internal reflection inside a rotational symmetric geometry.

This work presents an extensive study of the physical properties of silica microsphere resonators. Microspheres with diameters ranging from 30 to 100 μm have been produced. These resonators support so called whispering-gallery modes. These modes feature Q-factors as high as 10^9, corresponding to a finesse of 3×10^6 for spheres with a diameter of about 80 μm. These are to date among the highest available Q-factors, leading to cavity lifetimes of up to few μs. A near-field microscope and a confocal microscope are used as tools to unequivocally identify the mode structure related to the sphere topography, and for excitation and detection of single quantum emitters. A procedure has been developed to optimize the coupling of light by means of frustrated total internal reflection in a prism to a single mode selectively (in particular the so called fundamental mode).

In a next step the high field enhancement of the cavity modes can be exploited to observe ultra-low threshold nonlinear phenomena in silica glass. Here, stimulated Raman scattering is studied. A record ultra-low threshold of 4.5 μW could be observed, for a sphere with a Q-factor exceeding 10^9. The mode structure of the laser is investigated by means of a near-field probe. The interaction of the probe itself with the lasing properties is investigated in a systematic way: quenching of the lasing activity by enhancement of scattering losses through the tip was observed. This opens up new possibilities for detection of small particles.

Microcavities also constitute one of the building blocks of Cavity QED, where the basic system is a single dipole interacting with a single mode of the electromagnetic field. In this thesis the coupling of a radiative dipole to the whispering-gallery modes has been intensively studied, both theoretically and experimentally. The controlled coupling of a single nanoparticle to the whispering-gallery modes is demonstrated, then first results in coupling a single quantum emitter to a microsphere are reported. Since the experiments are performed at room temperature, there is always a manifold of modes involved in the optical processes. The resonant interaction with these modes, predominantly the whispering-gallery modes, is exploited to enhance photon exchange between two nanoparticles.

Finally a novel analogy between a system composed of a single atom interacting with one cavity mode on one side and intramodal coupling in microsphere resonators induced by a near-field probe on the other side is presented and experimentally explored. It is found that the induced coupling regimes reflect the different regimes of weak and strong coupling typical of Cavity QED. The transition between the two coupling regimes is observed, and a previously observed unexpectedly large coupling rate is explained.

Keywords:
Cavity QED, Nanooptics, Near-field Optics, Microscopy

Zusammenfassung

Optische Mikrokavitäten spielen eine wichtige Rolle in einer Vielzahl von optischen Prozessen, von der Resonator-Quantenelektrodynamik über Anwendungen in der Photonik bis hin zur optischen Detektion von Nano- und Mikroteilchen. Licht kann sehr effizient durch totale interne Reflektion, z.B. in rotationsymmetrischen Anordnungen, gespeichert werden.

Diese Arbeit beschreibt eine ausführliche Untersuchung der physikalischen Eigenschaften von Mikrokugelresonatoren aus Quarzglas. Hierfür wurden Mikrokugeln mit Durchmessern zwischen 30 und 100 μm hergestellt. Die gemessene Güte dieser Mikroresonatoren überstiegen 10^9, was bei einer Kugelgröße von 80 μm einer Finesse von mehr als 10^6 entspricht. Bis heute sind diese Güten die höchsten gemessenen Güten in optischen Resonatoren überhaupt: die Speicherzeit der Photonen im Resonator erreicht Mikrosekunden. Als experimentelle Hilfsmittel wurden in dieser Arbeit ein Nahfeld- und ein Konfokalmikroskop benutzt, um die Struktur der Moden bezüglich der Topographie des Resonators eindeutig zu identifizieren. Gleichzeitig wurden diese Instrumente eingesetzt, um einzelne Quantenemitter zu detektieren und anzuregen. Eine Prozedur zur Optimierung der Kopplung von Licht mittels frustrierter totaler interner Reflektion an einzelne Moden des Resonators, insbesondere an die sogenannte fundamentale Mode, wurde entwickelt.

In einem nächsten Schritt wurde die starke resonante Überhöhung des elektromagnetischen Feldes in den Moden des Resonators ausgenutzt, um nichtlineare Prozesse mit extrem niedrigem Schwellenwert im Quarzglas zu beobachten. Speziell wurde in dieser Arbeit die Raman-Streuung untersucht. Ein Schwellenwert von 4.5 μW für Raman-Lasing wurde für eine Kugel mit einer Güte von über 10^9 gemessen, was einen Rekordwert darstellt. Mittels einer Nahfeldsonde wurde die Modenstruktur eines solchen Mikro-Ramanlasers gemessen und der Einfluß der Nahfeldsonde auf die Lasereigenschaften systematisch untersucht. Ein *Quenching* der Laseraktivität aufgrund der Verstärkung der Streuverluste durch die Nahfeldsonde wurde beobachtet. Dieser Effekt eröffnet potentiell neue Möglichkeiten für die Detektion kleiner Teilchen.

Mikroresonatoren stellen auch einen Grundbaustein der Resonator-Quantenelektrodynamik dar, in der das fundamentalste System ein einzelner Emitter in Wechselwirkung mit einer einzelnen Resonatormode ist. In dieser Arbeit wurde die Kopplung von einem einzelnen strahlenden Dipol an die Moden von einem Mikrokugelresonator sowohl theoretisch als auch experimentell untersucht. Die kontrollierte Kopplung von einem einzelnen Nanoteilchen an die sogenannten *whispering-gallery* Moden eines Mikrokugelresonators wurde nachgewiesen. Erste Ergebnisse in der Kopplung eines einzelnen Emitters an die Moden des Resonators wurden erzielt. Die resonante Wechselwirkung mit Resonatormoden wurde ausgenutzt, um den Photonentransfer zwischen zwei einzelnen Nanoteilchen dramatisch zu verstärken.

Schließlich wurde die bislang unbeachtete Analogie zwischen dem Quantensystem eines einzelnen Emitters in Wechselwirkung mit einer einzelnen Resonatormode und dem klassischen System zweier gekoppelter Moden experimentell untersucht. Es stellte sich heraus, dass die aus der Resonatorquantenelektrodynamik bekannten Kopplungsregime der starken und schwachen Kopplung in Analogie auch an einem klassischen System beobachtet werden können. Der Übergang von schwacher zu starker Kopplung wurde beobachtet, und bislang gemessene unerwartet hohe Kopplungsraten konnten in der neuen Interpretation einfach erklärt werden.

Schlagwörter:
QED in Mikroresonatoren, Nanooptik, Nahfeldoptik, Mikroskopie

Contents

List of Figures

Chapter 1

Introduction

Optical microcavities confine light to microscale volumes. This ability can be exploited in many fields in engineering as well as in fundamental physics. In quantum information a long storage time of photons and a strong interaction of light with tiny amounts of matter - down to the single atom level - is essential. In microcavities, nonlinear optical effects can be tremendously enhanced due to a strong field amplification. The narrow linewidth of resonances opens the way to small and robust filters and optical sensors. Today microcavities are already build-in elements for every day life: for instance in the narrow-spot laser in a CD or a DVD player. The confinement of light in optical microcavities can typically be provided by three effects: Bragg scattering, total internal reflection and the photonic bandgap effect. A number of different forms and materials are used to implement these effects. Semiconductor micropillars, which are formed by sandwiching two small Bragg mirrors, play an important role in efficient single photon sources, as they offer a geometry suitable to incorporate single quantum emitters [Ger96, SPY00]. In 1991 a new type of microlaser was presented, which exploited a resonant structure in the form of a disk, where light was confined by total internal reflection [MLS+91]. Photonic crystal cavities are gaining more and more terrain particularly in the field of quantum communication and information [VLMS01, VY03]. Figure 1.1 sketches these cavities.

Optical microcavities also constitute one of the building blocks for Cavity Quantum Electrodynamics (QED) experiments. Ever since Purcell's seminal work [Pur46], in 1946, it has been clear that the spontaneous emission rate of a radiating dipole is not an intrinsic property of the dipole itself, but depends on its environment. A change in the density of state of the electromagnetic field in the medium surrounding the dipole (for instance due to the presence of a cavity) will affect its decay lifetime, enhancing or inhibiting it. This phenomenon is known as the Purcell effect [Pur46]. If the interaction between

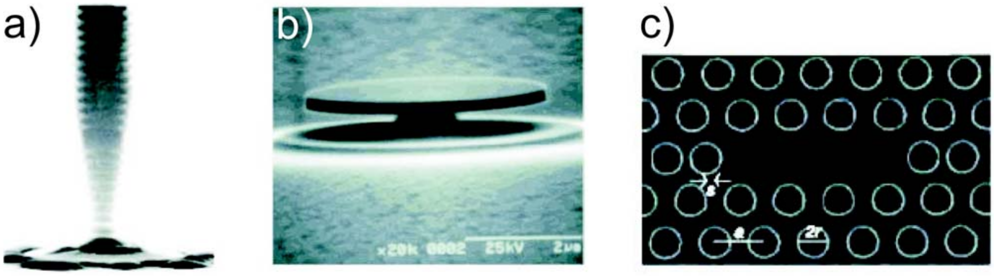

Figure 1.1: Different types of optical microcavities: a) micropillar cavity [PVZ+02], b) microdisk cavity [MKB+00], and c) photonic crystal cavity [YSH+04]

the dipole and the cavity is further enhanced by a resonant structure, a regime may be entered in which the dipole and the cavity exchange one energy quantum in a periodical way. This is the so called Rabi-oscillation. In this case the irreversible spontaneous decay process is transformed into an oscillatory behavior [SKV02].

In Cavity QED, the most basic system is given by a single dipole interacting with a single mode of a cavity [SK89, Ber94]. The first experiments were performed in the field of atomic physics, mainly by using Rydberg atoms in Fabry-Perot microcavities [Kle81, GRGH83, RTB+91, MWM85]. All these experiments suffer from the difficulty to position the emitter in a controllable way into a certain cavity mode [GKHW01]. Experiments that use solid state quantum emitters allow positioning of the emitter within the cavity with subwavelength precision by exploiting microstructuring techniques [BHA+05]. Single quantum dots, for instance, can be grown inside many solid state microcavities, e.g. in micropillar cavities [PVZ+02, VY03, SPY01]. Recently the regime of strong coupling has been reached in these systems [RSL+04]. Microdisks offer higher Q-factors, and coupling of quantum dots to these cavities has been reported [MKB+00], also here the regime of strong coupling has been reached [PSM+05]. The disadvantage is that once the emitter has been positioned it cannot be moved any longer, so that it is impossible to change or optimize its coupling to the modes of the cavity. This is even more difficult when envisioning positioning of more then one emitter.

Another special type of microcavity also relying on total internal reflection exploits a spherical form. Light is trapped along a path close to the equator, as shown in figure 1.2.

This principle has an acoustical analogy: in the cathedral of St. Paul in London, at the base of the dome, there is a circular gallery with a diameter of

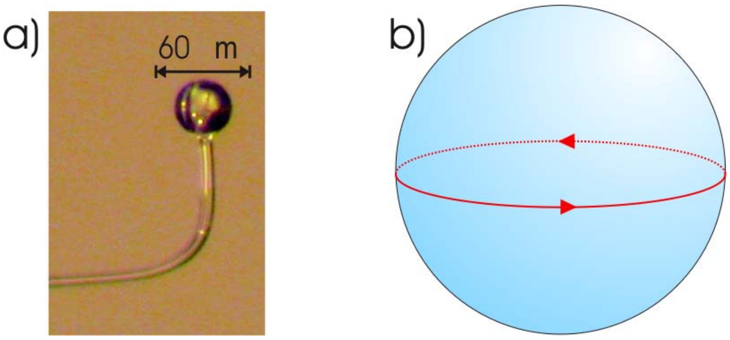

Figure 1.2: a) Photograph of a silica microsphere taken via an optical microscope. b) Sketch of a light ray guided by total internal reflection along the equator of a microsphere

about 33 m. If a person whispers along the gallery, the sound can be heard at any point close to the wall, even on the opposite side. If one speaks directly to the center of the gallery, nothing can be heard. It was realized that the sound waves are guided by the walls of the gallery: i.e. a whisper along the gallery can excite the acoustic eigenmodes of the circular dome, which are called whispering-gallery modes [Ray78, Ray10]. In 1989 a Russian group managed for the first time to observe an optical analog to whispering-gallery modes in small spheres melted from silica glass [BGI89]. There, first hints of possible uses of these cavities, like microoptic filtering or microlaser, were given. Much of the early research on spherical microcavities even before that time was performed on liquid droplets systems, motivated by the need of understanding light scattering from clouds or colloidal suspensions. These efforts led Gustav Mie to a classification of a family of resonances, called Morphology Dependent Resonances, that emerge when observing light scattering from small particles [Mie08, BW64]: for certain dimensions of the particles and certain wavelengths of the incoming light, the scattered light presented strong resonances. The whispering-gallery modes can be classified as a special class of these resonances: their distinguishing characteristic is that they feature extremely high quality factors exceeding 10^9, combined with mode volumes as small as 100 μm^3 [RA96, GMS$^+$06]. In such a situation the electric field per photon in a cavity mode is strongly enhanced: an input power of 1 mW can result in a circulating power of up to 1 GW/cm^2. This strong field enhancement makes these cavities ideal to study non-linear phenomena. Effects like stimulated Raman and Brillouin scattering at very low thresholds (on the order of 1 mW of input power) were first observed in liquid microdroplets by Richard Chang and Anthony Campillo [QC86, LHEC90, ZC90]. Already, this threshold was comparable to or less than other nonlinear devices, such as nonlinear silica fiber lasers [Agr01] and hydrogen-filled laser cavities [MPARaC01].

In this work an effort is made to study the physics of optical microcavities with techniques developed in scanning near-field optical microscopy. A versatile system has been developed, which allows to study enhanced nonlinear optical phenomenon, to control the coupling of a single nanoparticle to single modes of the electromagnetic field and also to highlight analogies between cavity QED and scattering in optical microresonators. Figure 1.3 shows a simplified sketch of the experimental setup.

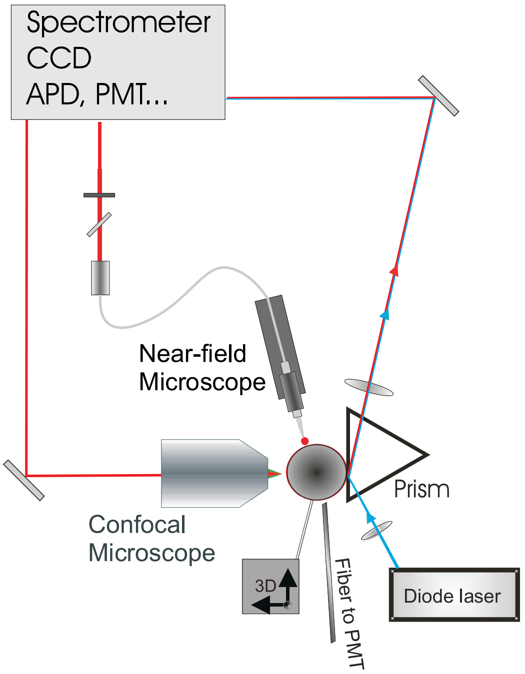

Figure 1.3: Schematic depiction of the experimental setup used in this work. Light is coupled to the whispering-gallery modes of a microsphere via a prism. The coupling of active material and the mode structure of the microsphere can be investigated by means of a confocal microscope or a near-filed microscope.

This work is divided into seven chapters. Following is a short description of each chapter:

- **Chapter 2**. In this chapter the optical properties of microsphere resonators are depicted. An analytical introduction to the whispering-gallery modes is given, and the important parameters of the resonators are introduced and explained. Finally, two possibilities of coupling light to the whispering-gallery modes are described.

- **Chapter 3**. In this chapter the experimental tools are described and the principles of confocal and near-field microscopy are reviewed. The procedure for the production of silica microspheres is illustrated. In this work a novel method for optimization of the coupling of light to whispering-gallery modes via a prism coupler has been developed, and is presented here.

- **Chapter 4**. In this chapter a first application of microsphere resonators is given: Raman lasing of a glass microresonator with a record ultra-low threshold. Scanning near-field optical microscopy is applied to investigate the mode structure of the laser, the relation between pump and lasing mode, and to prove single mode operation. The interaction between the near-field probe and the laser can lead to quenching of the lasing activity, resulting in a net force acting on the probe itself. A theoretical model for this interplay is developed. Additionally, a possible use of the system for detection of small particles is described.

- **Chapter 5**. This chapter is divided in two parts. First, the coupling of a single radiating dipole to the high-Q modes of a microsphere resonator is investigated theoretically. Detailed calculations of the coupling efficiency to a single mode of the microcavity are performed. The controlled coupling of a single nanoparticle attached at the end of a near-field probe to a microsphere is then demonstrated. In the second part of the chapter, the first experimental realization of cavity enhanced long-distance energy transfer between two single nanoparticles via shared whispering-gallery modes is demonstrated.

- **Chapter 6**. A near-field probe introduced into the evanescent field of one mode can scatter light back into the sphere in the counterpropagating mode, or in a continuum of lossy modes. In this chapter a so far unexplored analogy to a single dipole coupled to a microcavity is highlighted. The different coupling regimes are investigated and described in terms of Purcell effect and in terms of strong coupling regime typical in Cavity QED.

- **Chapter 7**. In this final chapter, first results in the controlled coupling of a single molecule to the high-Q modes of a microsphere resonator are shown. Follow-up experiments with single molecules and microcavities are proposed.

Chapter 2

Whispering-Gallery Modes

In this chapter a theoretical overview of the properties of a spherical microcavity and of whispering-gallery modes (WGMs) is given. Microsphere resonators offer optimal optical properties and are easy to fabricate. Their Quality factors are among the highest observed to date, and the mode volumes can be exceedingly small, approaching λ^3. The first indirect evidence of coupling of light to the WGMs dates back to 1961, where the stimulated emission of Sm^{++} ions embedded in spherical samples of CaF_2 was observed [GKL61]. By means of polarization analysis and time resolved measurement the contribution of the WGMs could be established. Since then, scattering of light by small spheres has been extensively studied, both theoretically and experimentally [BC88, BH98]. WGMs can be analytically described as a subgroup of morphology dependent resonances [BW64]. Alternatively, in a simple geometrical picture WGMs arise due to constructive interference of light rays trapped by total internal reflection within a microcavity. A number of different forms and materials can be used to produce cavities supporting WGMs [NKR+04, PC03].

2.1 Optical Properties of Microsphere Resonators

In this section an overview of the main properties of optical microcavities is given. References for a more detailed mathematical description will be given in the discussion.

2.1.1 Quality factor

The Quality factor, or Q-factor, is generally defined as the ratio of stored energy to the power loss [Jac89]:

$$Q = 2\pi \frac{\text{Stored energy}}{\text{Power loss}}. \tag{2.1}$$

It is a measure for how long a photon can be stored inside the cavity. Microsphere resonators can offer Q-factors as high as 10^9. The Q-factor can be also defined as the width of the resonance $\Delta\lambda$ divided by the resonant wavelength λ_0, or equivalently as:

$$Q = \frac{\lambda_0}{\Delta\lambda} = \omega_0 \tau \tag{2.2}$$

where ω_0 is the angular frequency ($\omega_0 = 2\pi c/\lambda_0$) and τ is the photon life time in the cavity. Thus, for optical frequencies in the visible range a photon can remain confined in the cavity for up to a few microseconds. To give a sense of the performance of these cavities, one can make an acoustic analogy. The human ear can best hear frequencies between 1 kHz and 3.5 kHz: at such frequencies a cavity with an Q-factor comparable to the optical example would resonate the sound for almost one week!

In a real cavity the Q-factor is given by the sum of the Q-factors determined by all the possible loss channels:

$$\frac{1}{Q} = \sum_i \frac{1}{Q_i}. \tag{2.3}$$

The main limitations to the Q-factor originate from absorption and surface scattering as well as from the in- and outcoupling device, when the sphere radius is greater then 5 μm. For smaller spheres radiation losses present in a curved dielectric cavity dominate [GPI00, BK03].

2.1.2 Free Spectral Range and Finesse

The Free Spectral Range (FSR) of a cavity is usually defined as the frequency spacing of its axial cavity modes [BW64]. In a microsphere resonator, where there are no axial modes and where the mode spectrum is more complex, the FSR can be defined as the spacing between modes with the same transverse structure. In analogy with a Fabry-Perot cavity, where the FSR is given by the speed of light divided by the length of the optical path of one round trip, for a microsphere resonator with radius R one can say:

$$\begin{aligned}\Delta\nu_{FSR} &= \frac{c}{2\pi NR} \\ \Delta\lambda_{FSR} &= \frac{\lambda^2}{2\pi NR}\end{aligned} \tag{2.4}$$

where N is the refractive index of the dielectric. For a silica microsphere resonator with a radius of $R = 20\ \mu$m and a refractive index $N = 1.46$ this would correspond to a FSR of $\Delta\lambda_{FSR} = 2.1$ nm at a wavelength $\lambda = 620$nm.

Related to the FSR and to the Q-factor is the Finesse, which can be defined as the ratio of the FSR and the resonance linewidth $\delta\nu$:

$$F = \frac{FSR}{\delta\nu} = 2\pi Q\frac{FSR}{\omega_0}. \tag{2.5}$$

The finesse of a cavity is a parameter which provides much information. It is related to the number of round-trips of the photon in the cavity, and it is used to describe the ability of the cavity to discriminate between two different modes. It also allows to calculate the amount of energy amplification in a resonant system: if ρ is the ratio of circulating power left after one round-trip (without an incident field) the the finesse is given by:

$$F \approx \frac{2\pi}{1-\rho}. \tag{2.6}$$

2.1.3 Mode Volume

The mode volume of a cavity is, together with the Q-factor, one of the most important parameters to pay attention to when observing nonlinear phenomena and studying Cavity QED effects. A small mode volume means that the energy of the electromagnetic field is stored in a small portion of space and results in a high optical energy density. The mode volume is defined as [BGI89, GPI00]:

$$V_{mode} \approx \frac{(\int_{V_Q} \epsilon(\vec{r})|E|^2 d^3\vec{r})^2}{\int_{V_Q} |E|^4 d^3\vec{r}} \tag{2.7}$$

where $\epsilon(\vec{r}) = N^2(\vec{r})$ is the dielectric constant of the material at $\vec{r}$, $\vec{E}$ is the cavity field and V_Q is the integration volume. For a microsphere with a radius of 25μm the mode volume is about $400\mu\text{m}^3$.

2.2 Analytical Expression for WGMs

The intent of this section is to summarize the analytical expressions for the modes of the electromagnetic field inside a microsphere resonator. The mathematical basis was developed by Gustav Mie in 1908, to explain the variety in colors of absorption and scattering exhibited by small gold particles suspended in water [Mie08]. Here a slightly different approach will be used, developed by Born and Wolf [BW64]. The problem can be set in this way: one has to solve Maxwell's equation when a plane monochromatic wave is incident upon a spherical surface. This solution also applies to diffraction by any number of identical spheres which are separated by a distance which is large compared to the wavelength. This theory also finds application in solving problems like the theory of rainbows, solar corona, the effect of clouds and fogs etc.

2.2.1 Representation of the Field in Terms of Debye's Potential

The problem to be solved is that of a plane, linearly polarized, monochromatic wave incident on a dielectric homogeneous sphere of radius R with a dielectric constant $\epsilon^{(II)}$. The geometry of the problem is sketched in figure 2.1. The problem will be solved in an appropriate coordinate system (spherical polar coordinates), and the fields will be represented as the sum of two "subfields": one, such that the electric vector has no radial component, the other such that the magnetic vector has no radial component.

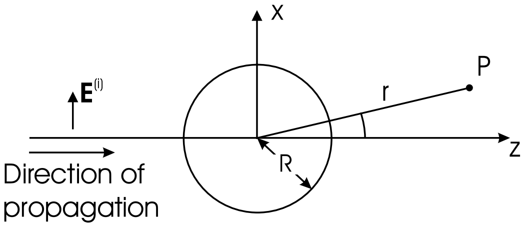

Figure 2.1: Diffraction of light by a small sphere. This figure displays the geometry of the problem.

The sphere is immersed in a homogeneous medium of dielectric constant $\epsilon^{(I)}$ and both the medium and the sphere are non-magnetic. Assuming a time dependence $e^{\imath\omega t}$ for the electric and for the magnetic field, the time-independent parts of the electric and magnetic vectors are related to each other in the following way:

$$\begin{aligned} \nabla \times \ \mathbf{H} &= -k_1 \ \mathbf{E} \\ \nabla \times \ \mathbf{E} &= -k_1 E = k_2 \ \mathbf{H} \end{aligned} \tag{2.8}$$

where

$$\begin{aligned} k_1 &= \frac{i\omega}{c}\left(\epsilon + i\frac{4\pi\sigma}{\omega}\right) \\ k_2 &= \frac{i\omega}{c} \end{aligned} \tag{2.9}$$

where σ is the conductivity. The square of the wave number k is given by $k^2 = -k_1 k_2$. All quantities which are related to the medium 1 are denoted by the superscript (I), while the quantities of medium 2 are denoted by the superscript (II). As the medium surrounding the sphere is assumed to be nonconducting, one has $\sigma^{(I)} = 0$. Assuming that the amplitude of the incoming electric field is normalized to unity $|\mathbf{E^{(i)}}| = |e^{ik^{(I)}z}| = 1$ and with reference to figure 2.1 for the definition of the axis, the six components of the electric and magnetic field vectors can be written as:

$$\begin{aligned} E_x^{(i)} &= e^{ik^{(I)}z}, \\ H_y^{(i)} &= \frac{ik^{(I)}}{k_2^{(I)}} e^{ik^{(I)}z}, \\ E_y^{(i)} &= E_z^{(i)} = H_x^{(i)} = E_z^{(i)} = 0. \end{aligned} \tag{2.10}$$

The boundary conditions require the tangential component of the field to be continuous across the surface of the sphere, i.e. at $r = a$:

$$\begin{aligned} E_{tang}^{(I)} &= E_{tang}^{(II)} \\ H_{tang}^{(I)} &= H_{tang}^{(II)}. \end{aligned} \tag{2.11}$$

This implies that outside the sphere one has not only the incoming field $\mathbf{E^{(i)}}$, $\mathbf{H^{(i)}}$, but also a scattered field $\mathbf{E^{(s)}}$, $\mathbf{H^{(s)}}$, so that the field outside the sphere is given by $\mathbf{E} = \mathbf{E^{(i)}} + \mathbf{E^{(s)}}$ (and analog for the magnetic field), while the field inside the sphere is denoted as $\mathbf{E^{(w)}}$. The problem can then be written in spherical polar coordinates:

$$\begin{aligned} x &= r\sin\theta\cos\phi \\ y &= r\sin\theta\sin\phi \\ z &= r\cos\theta \end{aligned} \tag{2.12}$$

so that the fields expressions 2.8 can be transformed into:

$$
\begin{aligned}
-k_1 E_r &= \frac{1}{r^2 \sin\theta}\left[\frac{\partial(rH_\phi \sin\theta)}{\partial\theta} - \frac{\partial(rH_\theta)}{\partial\phi}\right] \\
-k_1 E_\theta &= \frac{1}{r\sin\theta}\left[\frac{\partial H_r}{\partial\phi} - \frac{\partial(rH_\phi \sin\theta)}{\partial r}\right] \\
-k_1 E_\phi &= \frac{1}{r}\left[\frac{\partial(rH_\theta)}{\partial r} - \frac{\partial H_r}{\partial\theta}\right]
\end{aligned}
\tag{2.13}
$$

for the electric field, and

$$
\begin{aligned}
k_2 H_r &= \frac{1}{r^2 \sin\theta}\left[\frac{\partial(rE_\phi \sin\theta)}{\partial\theta} - \frac{\partial(rE_\theta)}{\partial\phi}\right] \\
k_2 H_\theta &= \frac{1}{r\sin\theta}\left[\frac{\partial E_r}{\partial\phi} - \frac{\partial(rE_\phi \sin\theta)}{\partial r}\right] \\
k_2 E_\phi &= \frac{1}{r}\left[\frac{\partial(rE_\theta)}{\partial r} - \frac{\partial E_r}{\partial\theta}\right]
\end{aligned}
\tag{2.14}
$$

for the magnetic field. The boundary conditions are now:

$$
\begin{aligned}
E_\theta^{(I)} &= E_\theta^{(II)} \\
E_\phi^{(I)} &= E_\phi^{(II)}
\end{aligned}
\tag{2.15}
$$

for $r = a$, and analog equations hold for the magnetic field components. The solutions of the field equations 2.13 and 2.14 will be written as superposition of two linearly independent fields (${}^e\ \mathbf{E}$, ${}^e\ \mathbf{H}$) and (${}^m\ \mathbf{E}$, ${}^m\ \mathbf{E}$) each satisfying 2.13 and 2.14 so that:

$$
\begin{aligned}
{}^eE_r &= E_r, \\
{}^eH_r &= 0 \\
{}^mE_r &= 0, \\
{}^mH_r &= H_r
\end{aligned}
\tag{2.16}
$$

It is clear that these solutions are consistent with the equations 2.13 and 2.14, and that they represent orthogonal fields. For the solutions to represent physical fields, an additional condition has to be satisfied, namely $\nabla\cdot{}^e\mathbf{H} = 0$. The solution with vanishing radial magnetic field is called *transverse electric wave* and that with vanishing radial electric field is the *transverse magnetic wave*. These solutions can be derived from two scalar potentials ${}^e\Pi$ and ${}^m\Pi$

respectively, called Debye's potentials (for a proof of this see [BW64]). In terms of these potentials the electric and magnetic fields are given by:

$$\begin{aligned} E_r &=^e E_r + {}^m E_r = \frac{\partial^2 (r\,{}^e\Pi)}{\partial r^2} + k^2 r\,{}^e\Pi \\ E_\theta &=^e E_\theta + {}^m E_\theta = \frac{1}{r}\frac{\partial^2 (r\,{}^e\Pi)}{\partial r \partial\theta} + k_2 \frac{1}{r\sin\theta}\frac{\partial (r\,{}^m\Pi)}{\partial\phi} \\ E_\phi &=^e E_\phi +^m E_\phi = \frac{1}{r\sin\theta}\frac{\partial^2 (r\,{}^e\Pi)}{\partial r \partial\phi} - k_2 \frac{1}{r}\frac{\partial (r\,{}^m\Pi)}{\partial\theta} \end{aligned} \tag{2.17}$$

for the electric field and

$$\begin{aligned} H_r &=^m H_r + {}^e H_r = k^2 r\,{}^m\Pi + \frac{\partial^2 (r\,{}^m\Pi)}{\partial r^2} \\ H_\theta &=^m H_\theta + {}^e H_\theta = -k_1 \frac{1}{r\sin\theta}\frac{\partial (r\,{}^e\Pi)}{\partial\phi} + \frac{1}{r}\frac{\partial^2 (r\,{}^m\Pi)}{\partial r \partial\theta} \\ H_\phi &=^m H_\phi + {}^e H_\phi = k_1 \frac{1}{r}\frac{\partial (r\,{}^e\Pi)}{\partial\theta} + \frac{1}{r\sin\theta}\frac{\partial^2 (r\,{}^m\Pi)}{\partial r \partial\phi} \end{aligned} \tag{2.18}$$

where both potentials ${}^e\Pi$ and ${}^m\Pi$ are solutions of the wave equation

$$\nabla^2\Pi + k^2\Pi = 0. \tag{2.19}$$

To ensure that the fields are continuous at the boundary of the spherical surface one must impose that the following components of the Debye potentials have to be continuous over this surface:

$$k_1 r\,{}^e\Pi, \qquad k_2 r\,{}^m\Pi, \qquad \frac{\partial (r\,{}^e\Pi)}{\partial r}, \qquad \frac{\partial (r\,{}^m\Pi)}{\partial r}. \tag{2.20}$$

To find a solution for equations 2.17 and 2.18 on can make the *Ansatz* that the solution has the form

$$\Pi = R(r)\theta(\theta)\Phi(\phi) \tag{2.21}$$

where the functions R, Θ and Φ are solutions of the following set of equations:

$$\begin{aligned} \frac{d^2(rR)}{dr^2} + \left(k^2 - \frac{\alpha}{r^2}\right) rR = 0 \\ \frac{1}{\sin\theta}\frac{d}{d\theta}\left(\sin\theta\frac{d\Theta}{d\theta}\right) + \left(\alpha - \frac{\beta}{\sin^2\theta}\right)\Theta = \quad 0 \\ \frac{d^2\Phi}{d\phi^2} + \beta\Phi = 0 \end{aligned} \tag{2.22}$$

where α and β are integration constants. As the field has to be a single-valued function of the position, certain conditions on Π have to be imposed, and these conditions will result in some constraints on the functions R, Θ and Φ. For the equation on Φ in 2.22 the most general solution is given by:

$$a\cos(\sqrt{\beta}\phi) + b\sin\sqrt{\beta}\phi \tag{2.23}$$

with the constraint that

$$\beta = m^2 \tag{2.24}$$

with m an integer number, so that the solution can be written as:

$$\Phi(\phi) = a_m\cos(m\phi) + b_m\sin m\phi. \tag{2.25}$$

The equation for $\Theta(\theta)$ is the equation for spherical harmonics. Since the solution has to be single-valued the condition $\alpha = l(l+1)$ has to be satisfied. The solution is given by Legendre-polynomials:

$$\Theta(\theta) = P_l^{(m)}(\cos(\theta)). \tag{2.26}$$

Only the part $R(r)$ remains: this can be transformed into the Bessel equation. The most general solution is:

$$rR(r) = c_l\psi_l(kr) + d_l\chi_l(kr). \tag{2.27}$$

where the $\psi(kr)$ and $\chi(kr)$ are proportional to the spherical Bessel's functions $J_{l+1/2}(kr)$ and to the Neumann's functions $N_{l+1/2}(kr)$:

$$\psi_l(kr) = \sqrt{\frac{\pi kr}{2}}J_{l+1/2}(kr), \qquad \chi_l(kr) = -\sqrt{\frac{\pi kr}{2}}N_{l+1/2}(kr). \tag{2.28}$$

The complete solution for $\Pi(r,\theta,\phi)$ is then given by:

$$\begin{aligned} r\Pi(r,\theta,\phi) = \sum_{l=0}^{\infty}\sum_{m=-l}^{+l}[c_l\psi_l(kr) + d_l\chi_l(kr)]\times \\ \times[P_l^{(m)}(\cos(\theta))][a_m\cos(m\phi) + b_m\sin m\phi] \end{aligned} \tag{2.29}$$

where a_m, b_m, c_l and d_l are arbitrary constants that have to be determined on the basis of the boundary conditions. From this expression the electric and the magnetic field inside and outside the sphere can be calculated. With regard to an incoming plane, linearly polarized wave, the incident field can be expressed as:

$$\begin{aligned} r\,{}^{e}\Pi^{(i)} &= \frac{1}{k^{(I)2}}\sum_{l=1}^{\infty} i^{l-1}\frac{2l+1}{l(l+1)}\psi_l(k^{(I)}r)P_l^{(1)}(\cos\theta)\cos\phi \\ r\,{}^{m}\Pi^{(i)} &= \frac{1}{k^{(I)2}}\sum_{l=1}^{\infty} i^{l-1}\frac{k^{(I)}}{k_2^{(I)}}\frac{2l+1}{l(l+1)}\psi_l(k^{(I)}r)P_l^{(1)}(\cos\theta)\sin\phi \end{aligned} \tag{2.30}$$

The boundary conditions 2.20 can be written in a more explicit way as:

$$\begin{aligned}\frac{\partial}{\partial r}[r({}^e\Pi^{(i)} + {}^e\Pi^{(s)})_{r=a}] &= \frac{\partial}{\partial r}[r^e\Pi^{(w)}]\\ \frac{\partial}{\partial r}[r({}^m\Pi^{(i)} + {}^m\Pi^{(s)})_{r=a}] &= \frac{\partial}{\partial r}[r^m\Pi^{(w)}]\\ k_1^{(I)}[r({}^e\Pi^{(i)} + {}^e\Pi^{(s)})_{r=a}] &= k_1^{(II)}[r^e\Pi^{(w)}]\\ k_1^{(I)}[r({}^m\Pi^{(i)} + {}^m\Pi^{(s)})_{r=a}] &= k_1^{(II)}[r^m\Pi^{(w)}]. \end{aligned} \tag{2.31}$$

This leads to the following expressions for the potentials from which one can derive the scattered field and the field inside the sphere. If $\zeta_l(kr) = \psi_l(kr) - i\chi_l(kr)$:

$$\begin{aligned} r^e\Pi^{(s)} &= \frac{1}{k^{(I)2}}\sum_{l=1}^{\infty} {}^eB_l\zeta_l^{(1)}(k^{(I)}r)P_l^{(1)}(\cos\theta)\cos(\phi)\\ r^m\Pi^{(s)} &= \frac{1}{k^{(I)}k_2^{(I)}}\sum_{l=1}^{\infty} {}^mB_l\zeta_l^{(1)}(k^{(I)}r)P_l^{(1)}(\cos\theta)\sin(\phi)\\ r^e\Pi^{(w)} &= \frac{1}{k^{(II)2}}\sum_{l=1}^{\infty} {}^eA_l\psi_l(k^{(II)}r)P_l^{(1)}(\cos\theta)\cos(\phi)\\ r^m\Pi^{(w)} &= \frac{1}{k^{(II)}k_2^{(II)}}\sum_{l=1}^{\infty} {}^mA_l\psi_l(k^{(II)}r)P_l^{(1)}(\cos\theta)\sin(\phi) \end{aligned} \tag{2.32}$$

The coefficient B_l can be expressed in a convenient form by using the so called "sphere parameter" q and a complex refractive index of the sphere with respect to its surrounding medium $\hat{N}$ defined as:

$$\begin{aligned} q &= \frac{2\pi}{\lambda^{(I)}}a\\ \hat{N} &= \frac{k^{(II)}k_2^{(I)}}{k^{(I)}k_2^{(II)}} \end{aligned} \tag{2.33}$$

By denoting with a prime the derivative of a function with respect to its argument the coefficients B_l take the form:

$$\begin{aligned} {}^eB_l &= i^{l+1}\frac{2l+1}{l(l+1)}\frac{\hat{N}\psi_l'(q)\psi_l(\hat{N}q) - \psi(q)\psi_l'(\hat{N}q)}{\hat{n}\zeta^{(1)\prime}(q)\psi_l(\hat{N}q) - \zeta_l^{(1)}(q)\psi_l'(\hat{N}q)}\\ {}^mB_l &= i^{l+1}\frac{2l+1}{l(l+1)}\frac{\hat{N}\psi_l(q)\psi_l'(\hat{N}q) - \psi'(q)\psi_l(\hat{N}q)}{\hat{n}\zeta^{(1)}(q)\psi_l'(\hat{N}q) - \zeta_l^{(1)\prime}(q)\psi_l(\hat{N}q)} \end{aligned} \tag{2.34}$$

and the coefficients ${}^eA_l$ and ${}^mA_l$ can be derived by the boundary conditions. In this way, the fields arising from the scattering of a plane wave by a small particle can be completely calculated. From this derivation an important feature of the fields can be pointed out: they depend on two integer numbers l and m, and resonances can be found. The resonances come from the fact that the denominator in the coefficient B_l has zeros at any root of the transcendental equation

$$\hat{N}\zeta^{(1)'}(q)\psi_l(\hat{N}q) - \zeta_l^{(1)}(q)\psi_l'(\hat{N}q) = 0 \tag{2.35}$$

The roots of this equation are numbered by a third integer number $n = 1, 2, 3\ldots$ A set of natural frequencies corresponds to the allowed set of values of the sphere parameter q, known as the modes of oscillation. The mode with $n = 1$ is the mode with the lowest frequency. It is also interesting to note that for large l the function $\zeta_l(kr)$ can be approximated by e^{ikr}, where $k \approx \frac{2\pi}{\lambda}\sqrt{1 - N^2}$, where N is the refractive index of the sphere. Since $N > 1$ k is complex, the field is no longer a propagating field, but decays exponentially. Such a field is called evanescent. The typical decay length of an evanescent field is about a wavelength. This is the field that allows access to the modes inside the sphere

At this point, having calculated the field expression of the whispering-gallery modes, one can calculate the mode volume using formula 2.7. This is quite a cumbersome calculation, and an approximation formula has been obtained [GPI00, BGI89]:

$$V_{mode} \approx 3.4\pi^{3/2}\frac{\lambda}{2\pi N}^{3} l^{11/6}\sqrt{l - m - 1} \tag{2.36}$$

This expression is valid only if $n = 1$. For a silica microsphere resonator (where N=1.46) with a radius of 22 μm, assuming $n = 1$, $l = 300$, $m = l$ and $\lambda = 670$ nm, this formula delivers a mode volume of 250 μm^3. This can be compared to the total volume of the sphere is 44602 μm^3 to have a good example of the strong field confinement in microsphere resonators.

2.3 Approximate Expressions for WGMs

The expressions of the electromagnetic fields in a microsphere resonator derived in the former section are rather complicated. It was shown that one has two main classes of solutions, either transverse magnetic or transverse electric, and that the modes are univocally identified by three quantum numbers n, l, m, in analogy with atomic bound states. Only a special class of the derived modes belongs to the so called whispering-gallery modes, and present high Q-factors. The intent of this section is to give a more intuitive picture of the WGMs and of the meaning of the three quantum numbers, n, l, m.

2.3.1 Radial Intensity Distribution

The best way to give a more heuristical picture of the WGMs is to exploit geometrical optics. Consider a light ray of wavelength λ traveling inside a microsphere of refractive index N and radius $a \gg \lambda$ as depicted in figure 2.2 a). If the ray hits the surface with an angle γ bigger than $\gamma_{critical} = \arcsin(\frac{1}{N})$ then the ray will be totally internally reflected. Because of the spherical symmetry all successive reflections will also occur under the same angle, and leakage will occur only though diffractive effects (although leakage is expected to be exponentially small, and it becomes evident only in a wave-optics picture).

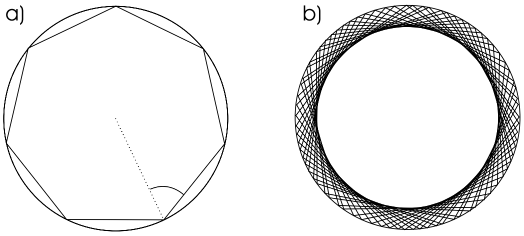

Figure 2.2: Geometrical representation of the WGMs. In a) the ray is trapped consistently, in (b) the ray only superimposes after 10 round trips.

If the number of reflections is an integer multiple l of the wavelength the light is trapped inside the sphere and constructive interference will result in build-up of a resonant mode. For large spheres where $a \gg \lambda$ the ray travels close to the sphere's surface, so that the total covered distance is approximately $2\pi a$. It is thus possible to give an approximated condition for the wavelength of a resonator mode: the phase must match after one round trip. This can be expressed as:

$$2\pi a \approx l\frac{\lambda}{N} \tag{2.37}$$

since in the resonator the ray has the wavelength λ/N. In terms of the size parameter $q = \frac{2\pi a}{\lambda}$ defined in section 2.2, the resonance condition is

$$q \approx l/N. \tag{2.38}$$

This can also be understood in another way. Considering the light ray in figure 2.2 as a photon, its momentum is given by

$$p = \hbar k = \hbar\frac{2\pi N}{\lambda} \tag{2.39}$$

If the ray strikes the surface at near-glancing incidence ($\gamma \approx \pi/2$), and is reflected l times, then the angular momentum is given by

$$\hbar l \approx ap = \hbar a \frac{2\pi N}{\lambda} \tag{2.40}$$

which is identical to $q \approx l/N$. This l is the same quantum number that appears in the previous section. Here it has an intuitive meaning, and can be associated with the angular momentum in the usual sense. The quantum number m can now immediately be interpreted as the z-component of this angular momentum, in a reference system where the photon propagates along the equator identified by the $x - y$ plane. Then it is:

$$m = l \cos\theta \tag{2.41}$$

It is intuitive to understand that for perfect spheres the modes are degenerate with respect to m, and this degeneracy is lifted when the resonator deviates from a perfect sphere.

If the light ray has a smaller angle of incidence on the sphere surface, then two round trips may be needed to have phase match. This means that the mode is deeply penetrating inside the sphere, and creates a different set of resonances, with a different wavelength but the same l. This is related to the radial component of the photon momentum, and can be connected to the quantum number n, which correspond to the roots of equation 2.35. The higher n, the more the intensity peak in the radial intensity distribution moves towards the center of the sphere. In figure 2.3 the radial intensity distributions for different n are sketched. It can be seen that the higher n, the more the mode leaks out of the sphere. This will correspond to lower Q-factors for modes with higher n.

2.3.2 Angular Intensity Distribution

The angular intensity distribution in the azimuthal direction (identified by ϕ) is rather simple, and can be directly deduced by the field expressions, which is either $\sin m\phi$ or $\cos m\phi$. The number of maxima in the ϕ direction is thus simply $2m$. This explains also the meaning of the quantum number m. In figure 2.4 a plot of the azimuthal intensity distribution is plotted for a whispering-gallery mode with $n = 1$ and $m = l = 9$.

In the polar direction, identified by θ the intensity distribution is a bit more complicated, the field being described by angular spherical functions. If the resonator is big enough (i.e. if the radius $a \gg \lambda$) then it is possible to

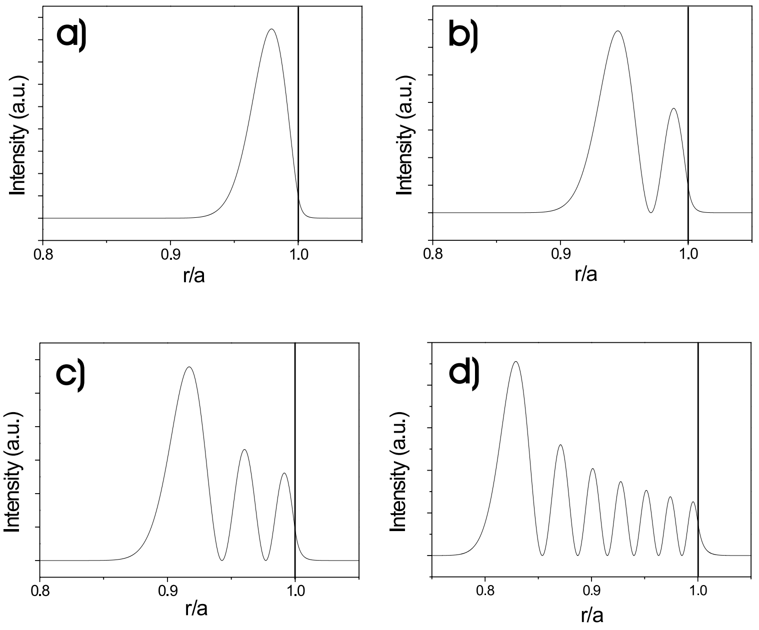

Figure 2.3: Radial intensity distribution for a whispering-gallery mode in a sphere of radius a with a) n=1, b) n=2, c) n=3 and d) n=7. The black line depicts the interface glass/air.

use a quasi-classical approach [GI94b]. The case $l - m = 0$ is the simplest situation, in which one can approximate [AS72]:

$$\frac{P_l(\cos\theta)}{(2l-1)!!} = \sin^l\theta \approx \exp[-\frac{l(\theta-\pi/2)}{2}] \tag{2.42}$$

If l is large this can be interpreted as a Gaussian beam having l/n reflections on the surface during one round trip inside the sphere. This Gaussian beam could be, for a perfect sphere, inclined at different angles. Due to the spherical symmetry this would result in a degeneration of the modes in m. In reality the spheres are never perfect, so that an equatorial plane can be defined. This also implies that the degeneracy in m is lifted. As a result, as the difference between l and m grows, the polar intensity distribution becomes a rapidly oscillating function of θ with a sharp cutoff at $\theta_{max} = \pi/2 \pm \arccos(m/l)$. An approximation can be made for large l and $m \simeq l$ [KDS$^+$95]:

$$I_{lm}(\theta,\phi) \propto |H_{l-|m|}(l^{1/2}\cos\theta)\sin^{|m|}\theta\exp(im\phi)|^2 \tag{2.43}$$

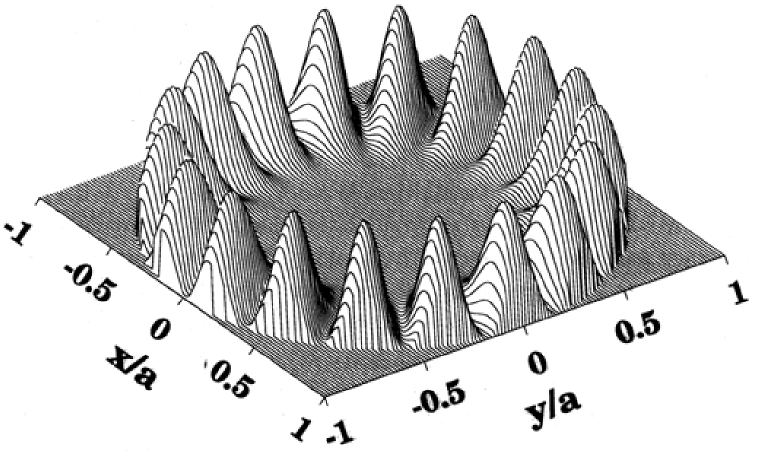

Figure 2.4: Azimuthal intensity distribution for a whispering-gallery mode with n=1 and m=l=9. The radius of the sphere is normalized to 1[Col94].

where $H_{l-|m|}$ is an Hermite polynomial of order $l-|m|$. From this equation, a mode with quantum numbers n, l, m has $l-|m|+1$ lobes in the polar intensity distribution. This distribution is centered around $\theta = 0$, being defined by the symmetry axis of the deformed spheroid. A plot for some $l-m$ values is reported in figure 2.5.

The quantum number m varies in the range $-|l| \leq m \leq +|l|$. The modes having $m < 0$ are simply propagating in the opposite direction as the modes with $m > 0$. Usually modes with the same and opposit m are degenerate. However, a scatterer can induce a coupling between these modes: as a result, the degeneracy is lifted, and the coupled modes behave like two coupled oscillators. The resonance is splitted to a doublet, with a frequency spacing between the two peaks which is proportional to the coupling rate. Chapter 6 is dedicated to the study of the properties of intramodal coupling. The mode with $n = 1$ and $m = l$ has the smallest mode volume, and is called *fundamental whispering-gallery mode* (FWGM) of a microsphere resonator. This is the most interesting mode since it presents the highest field per photon: this means that nonlinear phenomena are most pronounced in the fundamental mode.

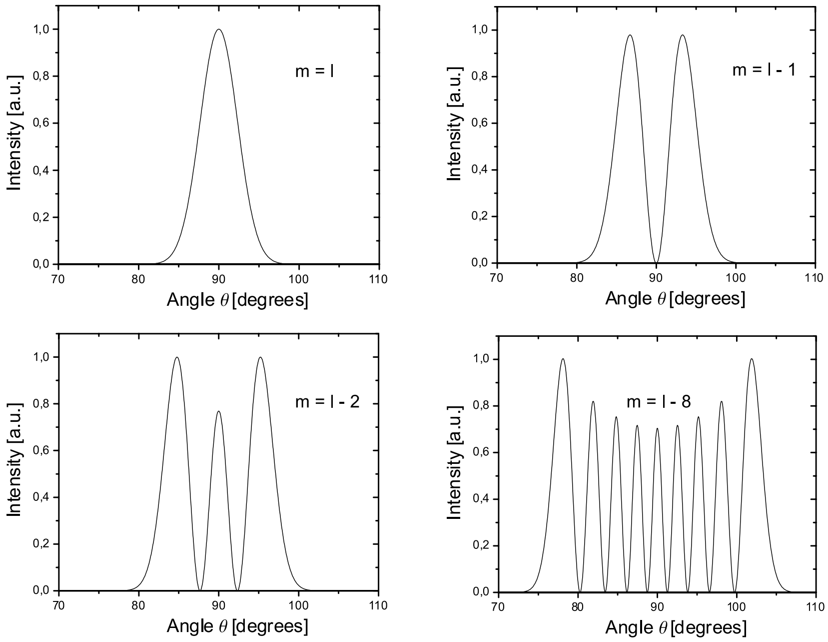

Figure 2.5: Polar intensity distribution for different $l - m$ values.

2.3.3 Spectral Properties of the Whispering-Gallery Modes

The former approximations have some disadvantages. On the one hand, the geometric optics approximation is valid only for big sphere parameters $q \to \infty$. On the other hand, all polarization information is lost. Additionally the rate of leakage is not available. It is possible, however, to gain some more information through an asymptotic analysis [SB91] to express the condition $q \approx l/N$ as an inverse series expansion in $L^{-1/3}$, where $L = l + 1/2$. If $q_{n,l}$ is the size parameter q associated to the resonance identified by the quantum numbers n and l [SB91]:

$$Nq_{n,l} = L + 2^{-1/3}\alpha_n L^{1/3} - \frac{P}{(N^2-1)^{1/2}} + \left(\frac{3}{10}2^{-2/3}\right)\alpha_n^2 L^{-1/3} \\ -\frac{2^{-1/3}P(N^2-2P^2/3)}{(N^2-1)^{3/2}}\alpha_n L^{(-2/3)} + O(L^{-1}) \qquad (2.44)$$

where $P = N\,(1/N)$ for transverse electric (transverse magnetic) modes, and α_n are the roots of the Airy function $Ai(-z)$ for $n = 1, 2, \ldots$

In [Sch93] it's shown that the accuracy of this series expansion can be better than 10^{-4} for $n = 1$ and $l > 50$. From the formula 2.44 an expression for the free spectral range (FSR) of the resonator can be deduced:

$$FSR = \frac{c}{2\pi a}[q_{n,l+1} - q_{n,l}] \approx \frac{2}{2\pi a N}. \tag{2.45}$$

The total internal reflection process is also responsible for a frequency shift between the TE and the TM modes. Different polarizations experience different phase-shifts under reflection on an interface. This shift can be expressed as [SB91]:

$$c_{TE/TM} = \frac{a_{n,l} - b_{n,l}}{FSR} \approx \frac{\sqrt{N^2-1}}{N} \tag{2.46}$$

where $a_{n,l}$ ($b_{n,l}$) is the sphere parameter for a TE (TM) mode. The constant $c_{TE,TM}$ depends only on the refractive index of the sphere N, and relates TE and TM modes with the same n and l. The TE mode has the higher frequency (or lower wavelength).

At this point, only one more approximation is needed to have a full picture of the whispering-gallery modes: modes with the same l but different m would be degenerate for a perfect sphere. In the real world, however, microsphere resonators are never perfectly spherical. This lifts the degeneracy. This problem is addressed in [GI94a], where it is shown that an arbitrary spherical function can be described as an inclined fundamental mode which is preceding. Modes with different m will then have a different frequency as they run over different perimeter lengths of the inclined ellipse of elipticity ϵ. A first order of approximation for this frequency shift leads to [SB91]:

$$\frac{\Delta\omega}{\omega} = \pm\frac{\epsilon^2(l^2-m^2)}{4l^2} \tag{2.47}$$

where $\Delta\omega$ denotes the difference in frequency between a mode with a certain m and the fundamental mode of the same family (same n and l). The positive sign in equation 2.47 denotes an oblate spheroid, the negative sign denotes a prolate one.

2.4 Efficient Coupling to Whispering-Gallery Modes

As shown in section 2.2 the natural modes of a sphere are well confined inside the sphere itself. The reciprocity theorem holds that if no light is coupled out of the sphere, then there is no trivial way to couple light into it. The solution to this hurdle is offered by the evanescent field (see the end of section 2.2).

If a light ray is grazing the sphere's surface, and it has the same k vector as the k vector of the evanescent field of the modes, than light can tunnel into the modes. In other words, an efficient coupling to the modes requires matching of the k vectors. There are several ways to obtain this: prism couplers [BGI89], fiber tapers [KCJB97], eroded monomode fibers [DKL$^+$95], angle polished single mode fibers [IYM99] and pedestal antiresonant reflecting waveguides [LLL$^+$00]. In this work two possibilities have been exploited: the prism coupler or the angle polished single mode fiber. In the following section, both coupler devices are described and their advantages and limitations are pointed out.

2.4.1 Prism Coupler

In a prism coupler an evanescent field can be created by launching a light ray under an angle Ψ bigger than the total internal reflection angle defined by $\Psi_{tot} = \arcsin \frac{1}{N_{prism}}$, where N_{prism} is the index of refraction of the prism (see figure 2.6). In air, close to the interface where the light ray is totally internally reflected, there is an evanescent field, whose k vector can be decomposed into two components perpendicular and parallel to the surface [CMD72]:

$$\begin{aligned} k_{\perp} &= \frac{2\pi}{\lambda}(1 - (N_{prism} \sin \Psi)^2)^{1/2} \\ k_{\parallel} &= \frac{2\pi}{\lambda}(N_{prism} \sin \Psi). \end{aligned} \tag{2.48}$$

If the incidence angle $\Psi > \Psi_{tot}$, then the perpendicular component of k is purely imaginary, and the electric field $\mathbf{E(r)} \propto e^{i(\mathbf{kr}-\omega t)}$ is no longer propagating in the direction perpendicular to the prism surface, but decays exponentially with the increasing distance from the surface. In order to couple light to the whispering-gallery modes of a microsphere the component $k_{\parallel}$ of the evanescent field has to be matched to the same component of the evanescent field of the modes:

$$\frac{2\pi}{\lambda} N_{prism} \sin \Psi = \frac{2\pi}{\lambda} N_{sphere} \sin \gamma, \tag{2.49}$$

where γ is the angle depicted in figure 2.2. This angle is for whispering-gallery modes of almost $\pi/2$, so one can approximate $\sin \gamma \approx 1$ and the condition 2.49 for the launching angle Ψ becomes:

$$\sin \psi \simeq \frac{N_{sphere}}{N_{prism}}. \tag{2.50}$$

For this condition to be satisfied, the refractive index of the prism has to be bigger than the refractive index of the sphere. In this work a prism made of flint glass was used. At a wavelength of about 620 nm, Silica has a refractive index of 1.46, while Flint glass has 1.72. Therefore, the optimal angle for coupling to the high-Q modes is given by $\psi = 59°$.

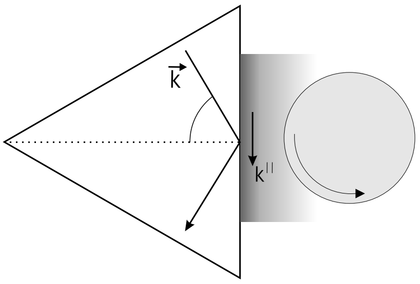

Figure 2.6: Efficient coupling to the whispering-gallery modes of a microsphere resonators by means of a prism coupler.

A prism with an internal angle of 60° is then chosen, so that the light ray can be launched almost perpendicularly to the prism surface. This fact, and an antireflection coating on the prism surface minimize the reflection losses. The condition 2.49 holds only for the fundamental mode as was proven in [GI99] and [GI94b], where the optimal coupling conditions for different whispering gallery modes were studied. From symmetry considerations it can be seen that the inclination angle with respect to the equatorial plane should be 0°.

The efficiency of the coupling depends not only on the incidence angle, but also on the distance between the sphere and the prism. The transmitted signal is a superposition of the incoming photons with the photons that are resonating into the whispering gallery modes. At the in- and output port they can interfere. On the other end the prism itself will introduce losses in the cavity. Three different regimes are usually distinguished, depending on the ratio of the internal losses of the sphere (characterized by the cavity decay rate τ_0^{-1}) to the losses induced by the coupler (described by the cavity coupling rate τ_k^{-1}):

- If $\tau_0^{-1} > \tau_k^{-1}$, the system is said to be in **under-coupled** regime, and the amplitude of the cavity leakage field is much smaller than the amplitude of the field transmitted by the prism;
- In the so called **over-coupled** regime, the rate of cavity coupling exceeds the cavity decay rate: $\tau_0^{-1} < \tau_k^{-1}$. Then the amplitude of the cavity decay field is larger than the transmitted pump field, and in

the case of strong over-coupling can reach a value of up to twice the waveguide amplitude;

- when $\tau_0^{-1} = \tau_k^{-1}$, the system is said to be in the **critical coupling** condition: the entire incoming signal is transferred to the resonator.

2.4.2 Polished Fiber Coupler

The prism coupler is a stable and practical device, but still may have some limitations. It is a quite bulky object compared to the microspheres and it requires collimating optics, which makes it less flexible. Therefore, in some experiments a polished fiebr coupler has been used, where the fiber has been polished under a specific angle. The first evidence of coupling to whispering-gallery modes of a microsphere resonator via a polished fiber and a theoretical description of the process can be found in [IYM99]. Since light is transported in the core of an optical fiber by total internal reflection, one can consider exploiting the evanescent field that is generated at the core's surface. First attempts to do this using an eroded optical fiber [DKL$^+$95] could not offer small dimensions and flexibility. If one polishes a fiber, however, the field at the tip will also be totally internally reflected and then escape from the fiber. If the microsphere is positioned in the range of the evanescent field from the core area, then an efficient energy exchange between the single mode fiber and the whispering-gallery modes of the microsphere can take place. A sketch of the setup is shown in figure 2.7.

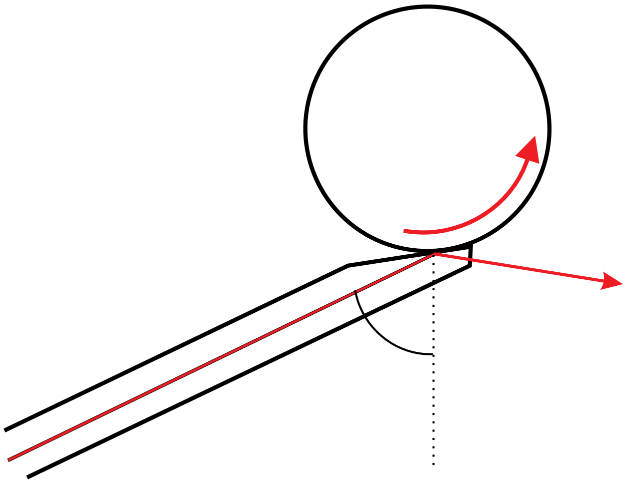

Figure 2.7: Efficient coupling to the whispering-gallery modes of a microsphere resonator by means of a polished fiber coupler.

Analog to the prism coupler the condition to match the evanescent field of the coupler to the evanescent field of the modes is:

$$\Phi = \arcsin\left(\frac{N_{sphere}}{N_{fiber}}\right) \tag{2.51}$$

where $N_{fiber(sphere)}$ is the refractive index of the fiber (sphere). The refractive index of the sphere is known, but the definition of the refractive index of the fiber is a bit more cumbersome, since the guided wave in the core no longer exists after it is reflected out of the fiber at the interface with the sphere. Nevertheless, as confirmed by the experiments´, one can make a simple approximation and consider N_{fiber} to be equal to that of a regular fiber, given by [IYM99]:

$$N_{fiber} = \frac{\beta}{k} = N_2\left[1 + \Delta(\frac{\nu}{V})^2\right] \tag{2.52}$$

where $k = 2\pi/\lambda$ is the wave vector, $\Delta = (N_2 - N_1)/N_1$ is the relative refractive index difference between the index of the cladding (N_1) and that of the fiber (N_2), V is the normalized frequency and ν the transverse decay constant.

This kind of coupler will be useful when working with single molecules, where a greater flexibility in the system is required.

Chapter 3

Experimental Setup: Methods and Instruments

This chapter provides a brief overview of the instruments and methods used in the experiments. Since the main goal of this work is the controlled coupling of radiating dipoles to the high-Q modes of a microsphere resonator, the requirements for the experimental instrumentation are quite stringent. The interaction of the high-Q modes with the external world is strongly dependent on the geometry of the system, for instance on the relative position between the sphere and the coupler. Nanometer precision is thus required to optimize all the parameters. The ability to work with single molecules is required, and tools to interact with the evanescent field of the high-Q modes of the resonators are essential for performing any experiment. Further details of the experimental tools can be found in [Göt04].

3.1 The Microsphere Spectroscopy Unit

In figure 3.1 a photograph of the experimental setup is shown.

The core of the setup is constituted by the microsphere itself. A prism has been chosen as an output coupler. The prism has the advantage of being a stable and robust coupler. The coupling geometry is fixed and optimized once, and does not require constant readjustment. Since working with single nanoparticles constitutes on of the main part of this work, the ability to identify, excite and detect single emitters down to the single molecule level is essential. The optimal tool to offer this performances is a confocal microscope. Finally, the need of unequivocal mode identification and the evanescent nature of the modes outside the sphere require the implementation of a Scanning Near-field Optical Microscope (SNOM), which also revealed itself

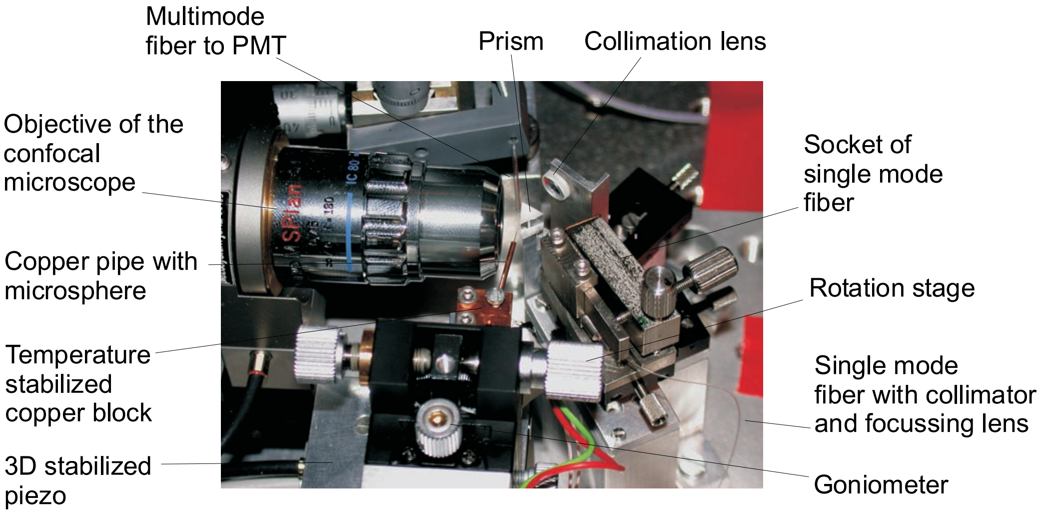

Figure 3.1: A photograph of the experimental setup.

as a powerful tool in the manipulation of single nanoparticles.

3.2 The Confocal Microscope

An important part of this work requires the ability to work with single molecules as emitters. An optimal tool to excite and detects single nanoparticles as single molecules or single quantum dots is a confocal microscope. The idea of confocal microscopy is to isolate the signal coming from one specific point from the contribution of the overlaying or nearby positioned scatterers.

The peculiar geometry of the microsphere spectroscopy unit, composed of the microsphere itself, the coupler and the multimode fiber necessary to detect photons scattered out of the microsphere imposes several conditions on the design of the confocal microscope. The microscope must be set up in an horizontal arrangement with a defined height, moveable with μm precision in all three spatial directions. For this reason commercial microscopes do not fit in the experimental setup, and a hand-made microscope was used. The details of the setup can be found in [Göt04]. A brief overview of the principles of confocal microscopy is given here, and the experimental setup is described.

3.2.1 Principles of Confocal Microscopy

A schematic depiction of confocal microscopy is shown in figure 3.2. The selection of light from one point and the rejection of light from all other points leads to very high contrast images in confocal microscopy. The disadvantage of this selectivity is the loss of the ability to look at a bigger portion of the sample at one time. Gaining information on a bigger area requires scanning the sample (or the excitation beam through the sample, as in the case here described) and an extenisive experimental time frame for the formation of a complete image.

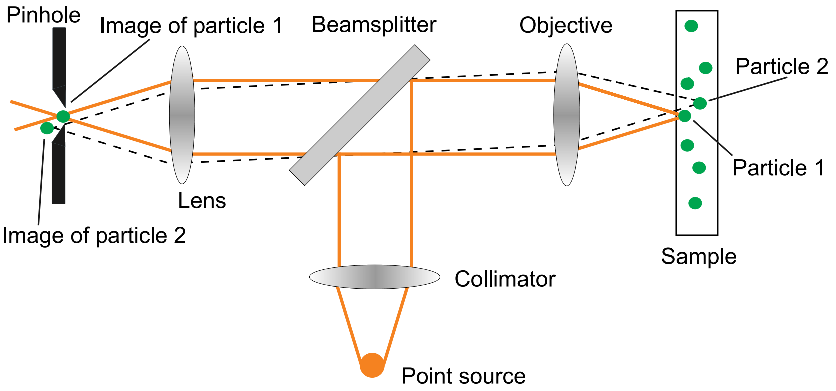

Figure 3.2: The principle of confocal microscopy [Göt04].

A point source is focussed on the object plane (e.g. on particle 1 in figure 3.2) of a microscope objective within the sample. The objective will form an image of the sample on a pinhole in the conjugated plane of the sample. The pinhole has the function of selecting out the light coming from different scatterers (e.g. particle 2 in figure 3.2) which is focussed on a different point and can thus not be transmitted through the pinhole. The *point spread function* (PSF) is the intensity pattern from a point source created by an optical system, e.g. a lens at its focal plane. This function determines the resolution of the optical system. For instance, for a circular aperture, the PSF is given by an Airy disk [Web96], so that the distance between the intensity maximum and the first dark fringe is

$$\Delta x = 0.61 \frac{\lambda}{NA} \tag{3.1}$$

where λ is the wavelength and NA the numerical aperture of the objective. Two objects are then just resolved if the intensity maximum of one falls into the first dark fringe of the other. Another advantage of confocal microscopy is that both illumination and detection are described by the same PSF, so that the the resolution becomes [Web96]:

$$\Delta x_{conf} = 0.44 \frac{\lambda}{NA}, \tag{3.2}$$

which shows the better performance of confocal microscopy.

3.2.2 Image Generation

The image generation is done by scanning the confocal spot across the sample. There are two possibilities: either one scans the sample itself or scans the excitation beam across the sample while leaving the sample fixed. Here, due to the complexity of the system studied, the second option is chosen.

A schematic depiction of the setup is shown in figure 3.3. A telecentric lens system is used to let the beam pivot around the back focal plane of the microscope objective. This results in a lateral movement of the excitation beam. For more details see [Göt04, Paw95, GC97].

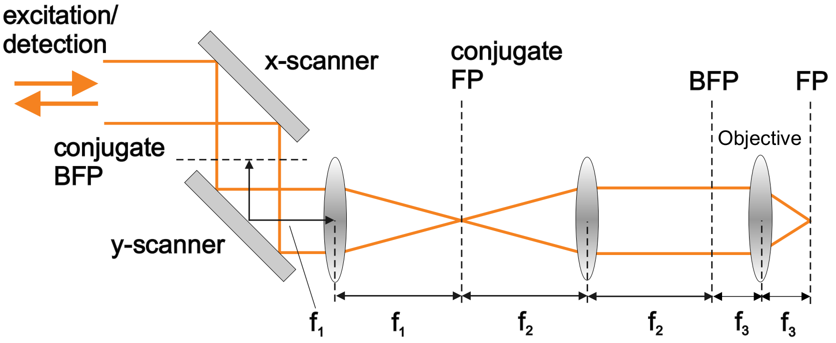

Figure 3.3: Beam scanning configuration: the x- and y-scanner mirrors (mounted on galvo drives) let the excitation beam pivot around a fixed point in the back focal plane (BFP) of the objective. This movement is transformed in a lateral displacement of the beam on the sample.

To show the performance of the confocal microscope the fluorescence image of single terrylene molecules embedded in a p-terphenyl crystalline matrix is shown in figure 3.4. Here the single molecules are oriented perpendicularly to the observation plane, so that the dipole emission pattern is clearly visible (this is also a typical signature of a single dipole emission) [PZH$^+$04].

3.3 The Scanning Near-field Optical Microscope

In this work a very important role is played by the near-field of the modes of the resonator. Therefore it is essential to have an instrument capable of interacting with this near-field in a controllable manner. The ideal tool is a Scanning Near-field Optical Microscope (SNOM). It is a very powerful tool: not only in the detection of the near-field of the high-Q modes, but

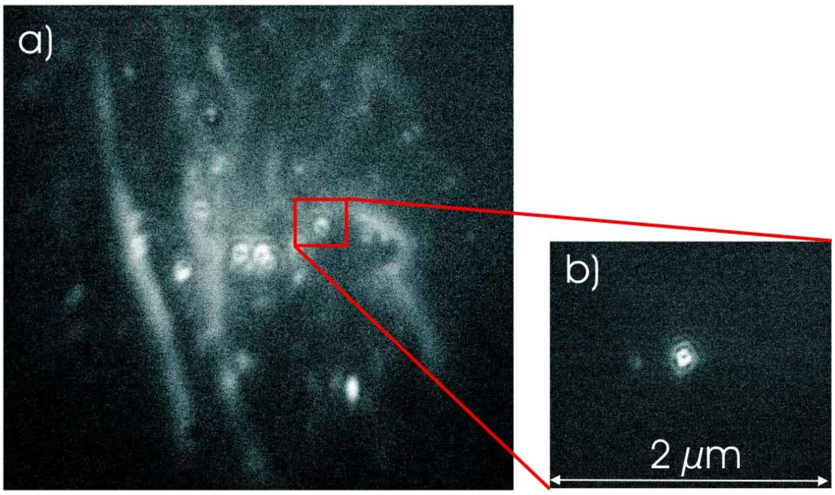

Figure 3.4: a) Confocal scan of a coverslip covered by spin coated terrylene molecules in a p-terphenyl film. The dipole emission pattern of a z-dipole of a single molecule is clearly recognizable. b) Confocal excitation of a single molecule.

also as a tool to position single nanoparticles in the evanescent field of the modes. Here, a very brief introduction to near-field microscopy is given. More details are provided in [Göt04]. The first realization of a SNOM was in 1984 ([LIHM84, PDL84]). A SNOM consists of a glass fiber tip which can be held at a fixed distance of few nanometers from a surface, which allows to simultaneously obtain optical and topographical information about the scanned sample. The optical resolution can be as good as a few tenths of nm [BT92], while the topographical resolution is determined by the diameter of the glass fiber tip. A second, powerful use for the SNOM is as a tool to position nanoparticles at will into a mode's field. As shown in [Kal02] it is possible to use a SNOM as a needle to pick up small particles from a surface.

3.3.1 Application of the Scanning Near-field Optical Microscope

As seen in paragraph 3.2 conventional optical imaging has a resolution restricted to about $\lambda/2$ because of diffraction. An oscillating dipole, however, not only promotes propagating waves, but also non-propagating evanescent waves [LK77]. These waves decay exponentially with growing distance from the radiating dipole. Access to the near-field with a subwavelength probe can transform evanescent photons into propagating photons through scattering, allowing thus to obtain information on an otherwise unaccessible region. In this work the near-field probe is a tapered glass fiber tip with an end-diameter of about 100 nm. The tip can be coated with aluminium, with a narrow aperture with subwavelength dimensions at the end. This is known as aperture SNOM: the aperture can be used as a nanoscopic light source to illuminate the sample through the evanescent field created at the aperture [BT92]. On the other hand the aperture can be used to collect scattered photons. In this work non-coated tips are used (known as apertureless SNOM [Oht98]).

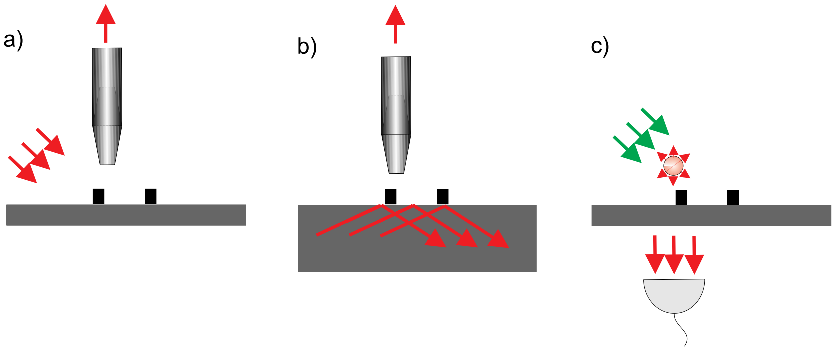

Figure 3.5: Different possible configurations of apertureless SNOM: (a) scattering SNOM, (b) photon tunneling SNOM, (c) active probe SNOM

Both aperture and apertureless SNOMs can be used in different configurations as shown in figure 3.5. One can globally illuminate the sample and use the tip as a detector, as in figure 3.5 a): in this case the near-field probe scatters the evanescent field created by the excitation light on the sample [ZMW95]. Modulation and lock-in techniques are needed to discriminate the true near-field signal from the background of excitation light. Another possibility is to illuminate the sample via total internal reflection as shown in figure 3.5 b). This configuration produces very low background, since only the light scattered in the junction between the tip and the sample can enter the fiber and be collected by a detector [CBB94]. This is the configuration exploited in this work to identify the whispering-gallery modes, as shown in section 3.5.

There are many other possible SNOM tips and SNOM configurations. An ultimate limit is active probe SNOM using a fluorescent nanoparticle [KHS$^+$01] or a single molecule [MHMS00], as shown in figure 3.5 c). If the nanoparticle is excited under far field illumination, then only the red-shifted fluorescence of the nanoparticle contributes to the image formation. The result is a high signal-to-noise ratio.

The distance between the SNOM tip and the scanned surface has to be stabilized with nanometer precision. This can be done by exciting the tip to oscillations of a few nanometers in amplitude. When the tip approaches a surface these oscillations are damped and phase-shifted. The oscillations can be detected optically as in atomic force microscopy, or electrically using piezoelectric elements. A feedback can be fed back to a piezoelectric positioning element. In this experiment the oscillations are excited and detected through a segmented ceramic piezo tube. A schematic depiction of the shearforce control loop is shown in figure 3.6. More details can be found in [Göt04].

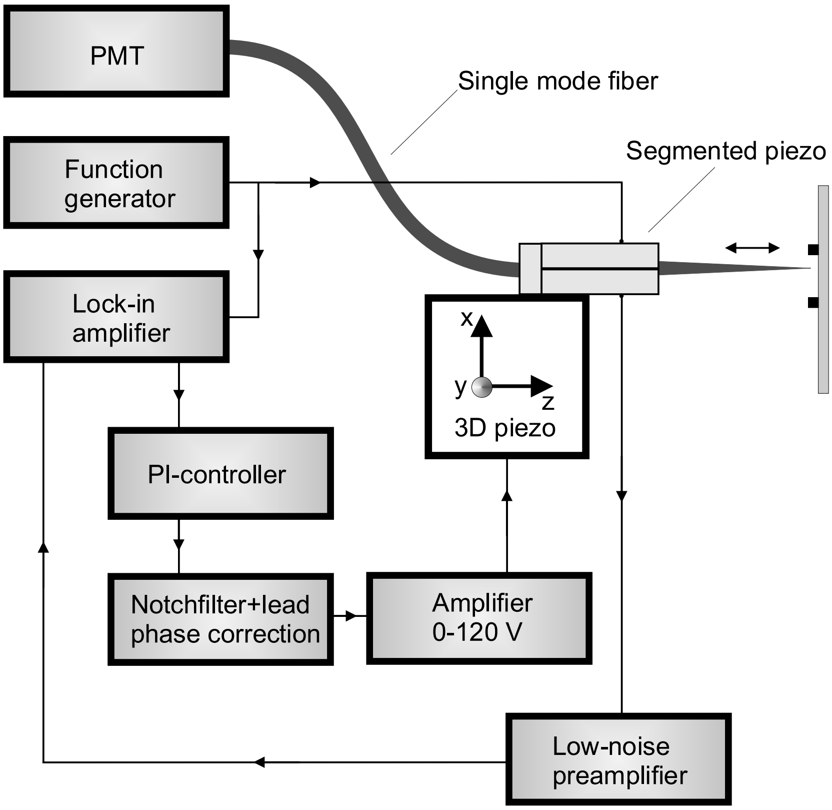

Figure 3.6: Block diagram of the shear-force control loop [Göt04].

For production of the SNOM tip used here a glass fiber tip was glued inside a micropipette held by a segmented ceramic piezo. When one of the segments is driven at the tip's resonance frequency its oscillation amplitude is strongly enhanced. The obtained signal is detected by another segment of the piezo tube. It is then amplified, filtered and demodulated with a lock-in amplifier, triggered by the driving function generator. A PI-controller is used to control the distance between the tip and the scanned surface. This signal also delivers the information about the surface's topography with a precision in the nanometer range.

3.3.2 Active Nano-probes

As pointed out in the previous section there is an additional use for SNOM probes. Attaching a single nanoparticle to the end of the tip allows for positioning of the same particle with nanometer precision. There are different methods to produce active nano-probes. The simplest one works well with particles that are larger than the tip, and is sketched in figure 3.7 a). In this case one starts with a coverslip with some nanoparticles dispersed on it, then by active positioning the tip can be moved above a single particle and then stuck through it. This was the optimal method to pick up single beads, polystyrene spheres which can be doped with dye molecules, with dimensions down to 200 nm. For smaller particles, or hard particles such as gold nanospheres, electrostatic bond or covalent bond to let the particle stick to the tip can be exploited [Kal02].

3.4 Production and Characterization of Silica Microspheres

Here the production and characterization of silica microspheres is briefly described. Silica microspheres with diameters ranging between 20 and 150 μm were produced, with Q-factors up to 1×10^9. It is most important to use silica glass with the lowest contamination possible. Metallic impurities will absorb in the ultraviolet region, whereas water contamination will spoil the Q-factor in the infrared region. Suprasil 300 glass rods (produced by Heraeus Quarzglas GmbH) with extremely low ion contamination are used (e.g. $OH^- \leq 1\, ppm$). The rods are cleaned in a 3-step process: first the rods are immersed in a solution of KOH-isopropanol to dissolve organic material present on the surface. In a second step the rods are put in a 40% nitric acid solution, to remove residual chemicals. The last step consists in immersion in a 40 % solution of hydrofluoric acid, to etch the outer layers of glass which still could be water contaminated. The longer the rods remain immersed in the acid, the more will be removed. A 30 minute immersion has consistently given good results. At this point the rods can be pulled into thin fibers (with a diameter of about 100 to 300 μm) with an oxy-hydrogen torch. The fibers are then cut into small pieces and glued into copper pipes by means of a superglue. The copper pipes will later have the important role of improving

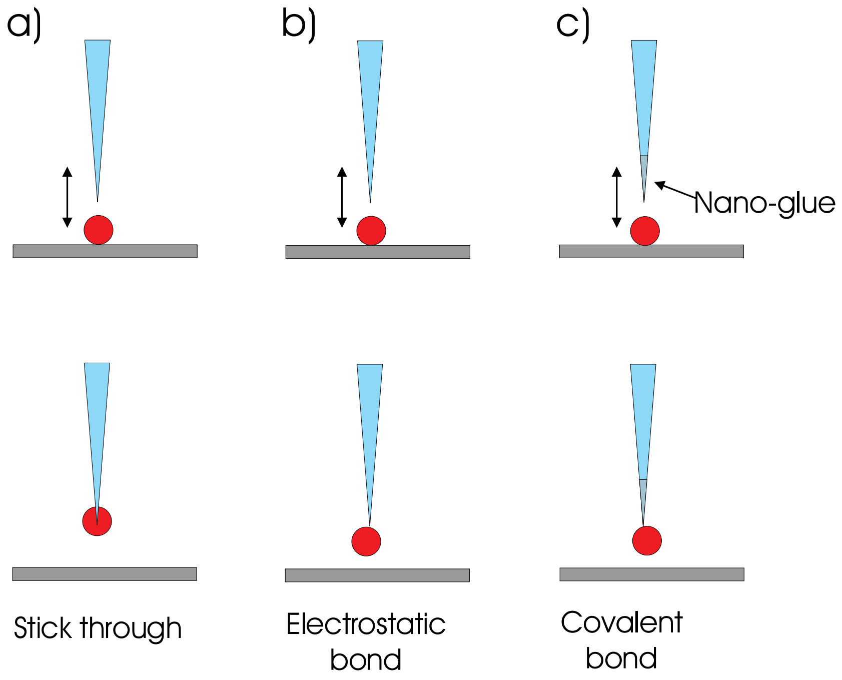

Figure 3.7: Different methods for picking up single nanoparticles with a near-field probe. In a) the stick-through method is shown. b) represent the pick-up method that exploits electrostatic force to let the particle stick to the SNOM tip, while in c) the tip is coated with a nano-glue before bringing it in touch with the nanoparticle.

thermal conduction for the temperature stabilization of the microsphere. The copper pipes are held horizontally in a 3-dimensional translation stage. A CO_2 laser is then focussed on the glass rod to melt it. First, the rod is pulled thinner with tweezers, then bent into a hook under gravity. Finally, the lower part of the rod melts and takes a spherical form because of surface tension. The setup is sketched in figure 3.8. Depending on how thin the rod is pulled, and on the speed with which the sphere is melted (which can be increased with laser power) the dimension of the sphere can be tuned with a precision of about 10 μm.

At the end of this process one will have a sphere attached to a thin stem. Care has to be taken during the melting process to ensure that the sphere sits in a good position on the stem, i.e. not too inclined or skew. This is because any inclination makes the coupling to the fundamental whispering-gallery mode more difficult. In the next section a method for optimizing the coupling to the high-Q modes will be presented.

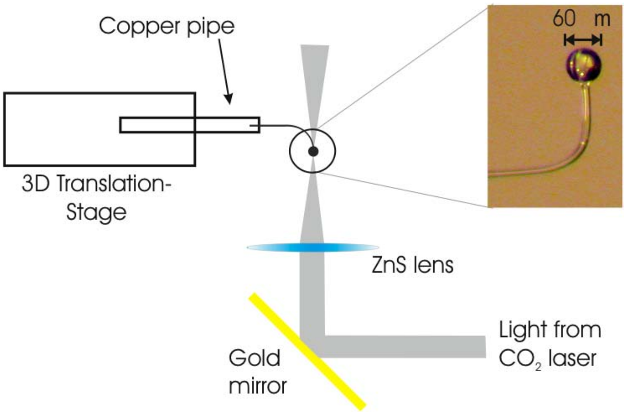

Figure 3.8: Setup for the production of silica microspheres

3.5 Optimizing Coupling to the Whispering-Gallery Modes

In a controlled experiment it is desirable to be able to optimize the coupling of light to a single WGM, specifically the fundamental mode in a routine and efficient manner. This allows for investigation of non-linear effects at extremely low pump powers, as all pump light is funneled into a single, highly confined mode. On the other hand, in experiments aiming at coupling of single quantum emitters to a single mode of an optical cavity, all photons in that particular mode should be coupled out with highest efficiency.

One main obstacle of spherical resonators (microspheres as well as microdiscs or toroids) compared to e.g. Fabry-Perot-type cavities is that there is no preferred direction into or out of which light can be coupled. Nevertheless, different methods have been developed to couple light to WGMs in spherical resonators. It was shown in chapter 2.4 how external couplers made from tapered fibers [KCJB97, LMSF01] as well as frustrated total internal reflection at a prism surface [GI94a] or at angle polished fibers [IYM99] have been used successfully. Also directional emission from nearly spherical resonators was demonstrated [LWFN03]. The theory of prism coupling to WGM's in spherical resonators was analyzed in detail in [GI99]. In most of the experiments in this work a prism coupler is used: this is the most flexible device, as it provides the ability for fine adjustment by convenient manipulation of the incident free beams [GI99]. Also, it allows one to control the Q-factor of the WGM over several orders of magnitude by varying the distance between the microsphere and the prism surface. External couplers, mandatory for spherical resonators, have to be aligned actively with respect to the geometrical symmetry axis of the resonators. Due to the production process, which is usually a melting procedure, there is always a small ellipticity (of a few %) and thus a well defined symmetry axis. Mismatch of the spatial alignment with respect to this *a priori* unknown axis rapidly decreases the efficiency of coupling.

A method determining the symmetry axis of a slightly non-spherical microsphere resonator and, hence, optimizing the coupling of light to the fundamental whispering-gallery mode (FWGM) when using a prism coupler is needed. In this work such a method was developed by mapping the intensity distribution of WGM's on the sphere's surface and the sphere's topography simultaneously with the use of a near-field probe. The basic experimental setup for SNOM mapping of whispering-gallery modes in a microsphere resonator is sketched in fig. 3.9. A microsphere of radius $r = 59$ μm is fabricated as described in the previous section. The microsphere is mounted on a translation stage combined with a goniometer and a rotation stage. As a first step the sphere is coarsely aligned with respect to the prism coupler. The beam from a narrow-band tunable diode laser (wavelength $\lambda = 670$ nm, linewidth $\delta\lambda < 300$ kHz, tuning range ≈ 60 GHz) is focussed to a small spot on the surface of the prism. A photodiode and a multimode fiber leading to a photomultiplier detect the transmitted light of the probe laser and the light which was scattered in resonance off the WGM's, respectively. The SNOM probe (similar to that used in [GBS01, GBS02]) is connected to a second photomultipier, which recorded the signal when mode mapping was performed.

With the help of the translation stages the microsphere is positioned into the evanescent field produced by total internal reflection from a diode laser beam at the prism coupler. The symmetry axis of the slightly non-spherical resonator is oriented approximately parallel to the stem. However, the exact orientation is not known *a priori*. An "optical equator" can be defined as the plane in which the FWGM propagates with a ring-like intensity distribution. If the optical equator is not exactly aligned with respect to the prism, the FWGM will not couple efficiently. Besides, the area on the sphere surface which is closest to the focal spot of the diode laser on the prism does not necessarily coincide with the position of the fundamental mode, as sketched in figure 3.10.

Coupling to higher order modes with $l \neq m$ is favorable in this configuration. Thus, two rotational degrees of freedom (characterized by the angle α and β in figure 3.10) are needed to adjust the sphere's optical equator.

Figure 3.11 a) shows the measured spectrum of the light detected by the multimode fiber when the diode laser is tuned over a range of 10 GHz. The photomultiplier, PMT1, (see figure 3.9) registers a spectrum with a set of

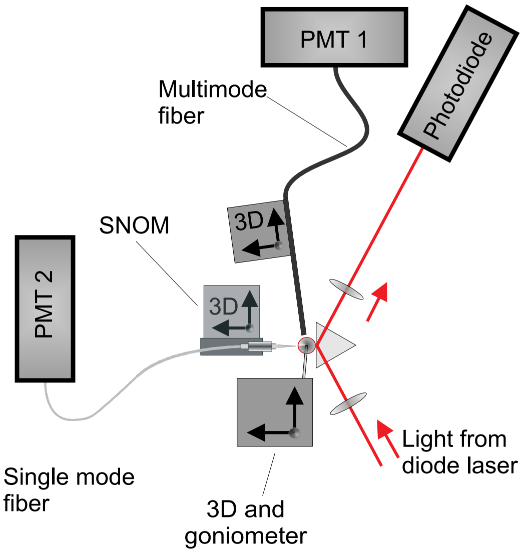

Figure 3.9: Schematic depiction of the experimental setup for SNOM mapping of the whispering-gallery modes of a microsphere resonator. The beam from a diode laser is focussed on the prism with a lens. A photodiode and a photomultiplier (PMT1) behind a multimode fiber allow recording spectra of the microsphere resonator which is mounted on a translation stage combined with a goniometer. The SNOM probe is connected to an additional photomultiplier (PMT2).

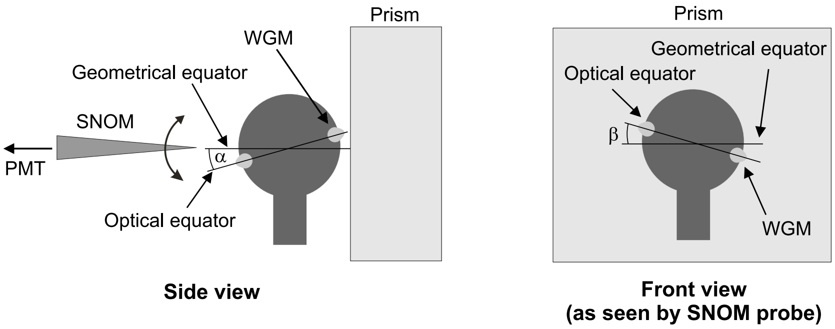

Figure 3.10: Schematic side and front view of the microsphere-prism system. The fundamental mode is inclined with respect to the horizontal plane due to the fabrication process and therefore does not couple efficiently to the prism.

equally spaced modes belonging to the same family, sharing the same l mode number, but differing in their m numbers.

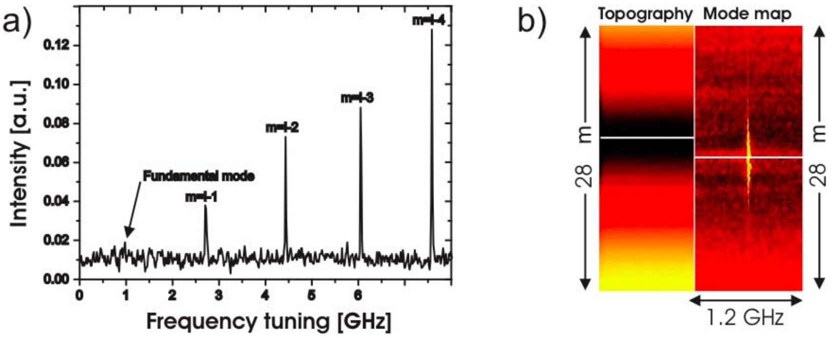

Figure 3.11: a) Recorded spectrum of modes with $m \leq l$ before optimization. The fundamental mode is hardly visible. b) Topographical-spectral (left, polar scan range 28 μm) and a spatial-spectral (right, spatial scan range 28 μm, spectral scan range: $\sim$ 1.2 GHz) mode map of the FWGM.

The splitting $\Delta\omega$ of the modes with different m is a function of the microsphere's ellipticity ϵ. It breaks the symmetry and separates the initially degenerate modes with different m numbers as described in section 2.3. In a non-spherical microsphere resonator (oblate spheroid) the lowest energy mode of a given family is the FWGM [GBS01]. The observed splitting of 1.6 GHz for this sphere of radius 59 μm is in agreement with an $\epsilon \simeq 0.04$. No further modes of the same family appear in the lower frequency side (not shown in figure 3.11 a). Obviously, in this measurement modes with a larger value of $l - m$ couple more efficiently than the FWGM, which can hardly be seen in the scattering signal recorded by the photomultiplier.

In order to optimize the coupling to the FWGM a mode mapping with the SNOM probe is performed. The distance between the probe and the microsphere is actively stabilized to approximately 10 nm using the shear-force method as explained in section 3.5. When scanning the probe across the surface of the sphere an optical signal is recorded. This is given by photons scattered into the near-field probe off the evanescent field of the WGM's. In addition, topographical information provided by the signal extracted from the control loop of the shear-force stabilization is obtained. The topographical information defines the "geometrical equator" (see figure 3.10), which is the cross-section of the horizontal plane (defined by the incident plane of the diode laser beam, which is parallel to the optical table) and the microsphere resonator. Next the SNOM probe was scanned in the direction perpendicular to the geometric equator along the sphere surface. At each point the laser frequency was tuned across the resonance of the FWGM and both the optical and topography signals were recorded. The resulting topographical-spectral and spatial-spectral maps are shown in figure 3.11 b). The topographical signal does not depend on the frequency of the diode laser as expected, but an optical signal from the FWGM is only detected in resonance. The single maximum of the measured intensity distribution of the WGM proves that the fundamental mode has been detected. White lines in the insets are plotted to highlight the geometric equator (topographical map) and the optical equator (spatial map). From the shift of the two lines with respect to each other it is possible to directly determine the angle α (see figure 3.10). Then, the microsphere is tilted with the rotation stage to annul the shift.

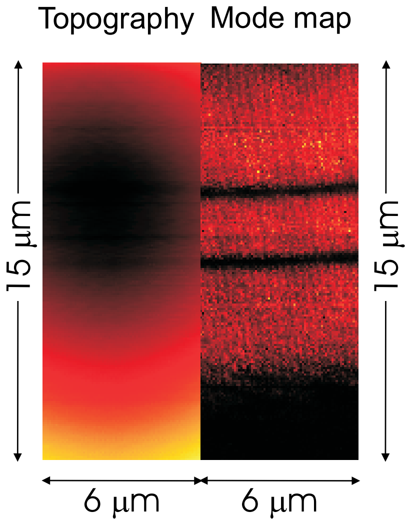

Figure 3.12: Two dimensional mode map. On the left the two-dimensional topography map of the microsphere is shown, while on the right a two-dimensional mode map showing the mode with $m = l - 2$ can be seen. The scan range for both figures is 15 μm along the polar direction, and 6 μm along the azimuthal one, from which β is calculated to be 3°. During the measurements the laser was continuously scanned around the resonance of the WGM.

The alignment of the second rotational degree of freedom (angle β in figure 3.10) can be done with the mode mapping technique. In order to do this a two-dimensional mode map similar to the one described in [GDBS01] is performed. Figure 3.12 shows a two dimensional map of the topography (left) together with a two dimensional map of the optical near-field (right). In this case the laser frequency was continuously scanned around the resonance of a WGM with $l - m = 2$, which explains the three maxima in the vertical direction of the intensity distribution. The derivation of the tilting angle β with respect to the horizontal axis is straightforward. By using the goniometer of the spectroscopy unit the microsphere can be tilted to compensate for the angle β.

Figure 3.13 shows a spectrum after the optimization procedure, i.e., the correction of the two tilting angles α and β. Insets again show a topographical-spectral and a spatial-spectral map. This figure has to be compared to figure 3.11: first, both white lines which indicate the geometrical and optical equator, respectively, are now collinear. This means that the microsphere resonator is perfectly aligned with respect to the prism coupler. Second, the spectrum shows that the coupling is now optimized for the FWGM, which is by far stronger than modes with $l \neq m$. An improvement of the coupling efficiency of the FWGM by at least two orders of magnitude was obtained. The fundamental mode is now symmetrically centered around the geometrical equator of the microsphere, and this position maximizes the overlap between the FWGM and the evanescent spot at the surface of the prism coupler. With prism couplers it was possible to obtain coupling efficiencies to high-Q WGM's exceeding 70 %. However, this is still not the ultimate limit of a prism coupler as mode matching could be further improved [GI99]. Besides, as is demonstrated by the comparison between figures 3.11 a) and 3.13 a), it is evident that in general identifying the fundamental mode only from the spectral information is not a simple process.

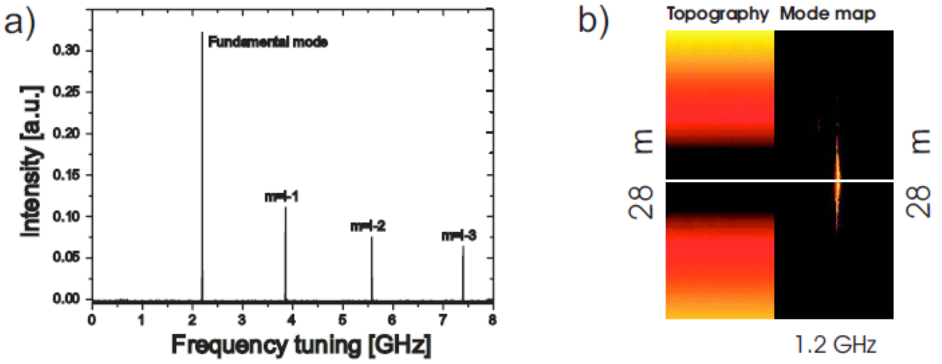

Figure 3.13: a) Recorded spectrum of modes with $m \leq l$ after optimization. Coupling to the fundamental mode is now strongest. b) Topographical-spectral (left, polar scan range 28 μm) and a spatial-spectral (right, spatial scan range 28 μm, spectral scan range: $\sim$ 1.2 GHz) mode map of the FWGM.

These results demonstrate that a near-field probe is a very versatile tool when investigating confined light in microresonators, but also makes it possible to implement a reliable procedure to align and optimize the coupling to the whispering-gallery modes. This is of paramount importance for experiments aiming to observe non-linear effects at extremely low pump powers [SKV02] or at the coupling of single quantum emitters to single modes [GdSMM$^+$03], where optical signals are on the single photon level. These two processes are discussed in chapters 4 and 5.

Chapter 4

Ultra-low Threshold Raman Laser

In this chapter the peculiar optical properties of a microsphere resonator, namely the extreme enhancement of non-linear effects, are studied. The lasing properties of an ultra-low threshold Raman laser made only from a glass microsphere are investigated. In addition, the influence of a scatterer on the lasing activity is studied. When studying non-linear phenomenon such as Raman scattering, silica would definitely be one of the least suitable material to choose: its second order nonlinearity coefficient χ_2 is zero due to the inversion symmetry, and the third order coefficient χ_3 is up to two orders of magnitude smaller than that of most other materials. On the other hand, silica has a very low absorption in the visible range, compensating for the low nonlinear coefficients. Additionally, nonlinear processes in a cavity can change radically. The high-Q of the modes combined with the small mode volumes lead to strong field enhancement and ultra-low thresholds for nonlinear phenomena. For a process such as stimulated Raman scattering thresholds on the order of a few μW could be observed. Here the relation between pump and lasing mode is investigated with the help of a near-field probe. The probe itself leads to an intricate interplay between lasing and scattering processes that is studied as well.

4.1 Stimulated Raman Scattering in Microcavities

Raman scattering was first observed by C.V. Raman in 1928 [RK28]. When detecting light scattered from a sample material, one generally finds that it contains frequencies different from those of the excitation source [BH98].

Incoming photons are inelastically scattered on the vibrational level of the molecule of the sample, or in other words a photon-phonon interaction occurs, and the scattered photon can loose or gain energy in this interaction [Boy92]. The phenomenon is usually described by taking advantage of the energy level system described in figure 4.1: in the Raman Stokes scattering there is a transition from the ground state g to a vibrational excited state n, via a virtual level n'. In this transition a photon with energy lower than the incoming photon is emitted.

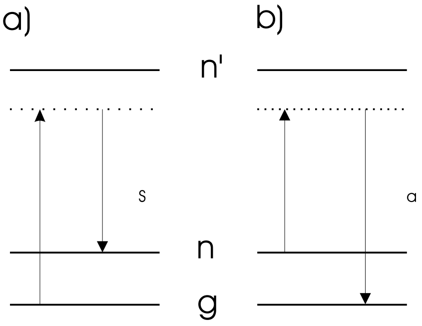

Figure 4.1: Energy level scheme describing the Stokes (in a)) and anti-Stokes (in b)) Raman scattering

In the anti-Stokes Raman scattering the molecule is initially in a higher vibrational level, and the photon emitted after excitation has a higher energy than the incoming photon, leaving the molecule in the ground state. Stokes radiation is easier to observe, since the Stokes process starts from a less energetic level than the anti-Stokes process. Raman scattering leads to both forward and backward scattered fields, since the momentum conservation in the process is intrinsically satisfied (the phonon dispersion relation is basically flat), and an optical phonon carrying the difference in wave-vector $\Delta k = k_p - k_s$ can be found for both backward and forward scattered light [Boy92]. This is quite important, since in a microcavity this leads to coupling of the Stokes radiation to both clockwise and counterclockwise propagating modes (as also observed in section 6). In a cavity, stimulated Raman scattering is favored. An important parameter for Raman scattering in microcavities is the gain spectrum, shown in figure 4.2: for glass this is very broad, about 10 THz, and has two maxima shifted by 13.9 and 14.3 THz from the pump frequency. This insures that there will be Stokes radiation resonant with the cavity, which has a typical FSR in the range of some hundreds of GHz. The gain coefficient of silica is very low, on the order of 10^{-11} cm/W. This is, however, compensated by the high Q-factors and the resulting strong field enhancement of the WGMs.

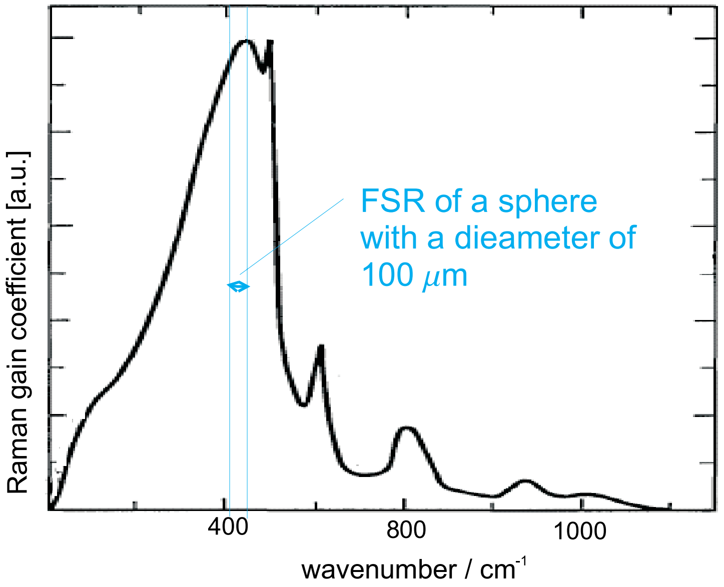

Figure 4.2: Raman gain Spectrum for silica glass [Sto89]. The blue lines show the free spectral range for a sphere with a diameter of 100 μm. The broadness of the gain spectrum ensure that there will always be a part of the Raman signal in resonance with the cavity.

The regime of Raman lasing is reached when the cavity roundtrip gain equals the cavity losses. A steady-state analysis of the equation describing the pump and the Stokes fields in the cavity leads to the following expression for the threshold of Raman lasing [KSM$^+$04]:

$$P_T = \Gamma \frac{4\pi^2 N^2 V_m}{g \lambda_p \lambda_s} \frac{Q_\kappa}{Q_{tot}^3}. \tag{4.1}$$

In this formula P_T is the threshold power *inside* the cavity, V_m is the mode volume, $\lambda_{p(S)}$ is the pump (Stokes) wavelength, N is the index of refraction of the sphere, Γ a factor taking into account the coupling between clockwise and counterclockwise propagating modes (whose value ranges between 1 and 2), g is the Raman gain in glass, Q_k is the coupling-limited Q factor of the sphere, and Q_{tot} the total Q-factor. This equation gives some important information about the process. The threshold value is proportional to the mode volume, and inversely proportional to the square of the Q-factor, which consequently plays a fundamental role. As a result it is desirable to work with small spheres and with low order modes to observe ultra-low thresholds. The same analysis also gives a formula for the intensity of the Stokes field

[KSM+04]:

$$I_{out} \propto \sqrt{\frac{Q_{tot}}{Q_k}}(\sqrt{P_{in}} - \sqrt{P_T})U(P_{in} - P_T) \tag{4.2}$$

The step function $U(P_{in} - P_T(\theta))$ ensures that when the pump power P_{in} is below threshold no lasing occurs. It should be stressed at this point that this is a complete classical analysis, where any possible gain enhancement due to cavity electrodynamics is neglected. A more detailed analysis of the Raman scattering process in microsphere resonators can be found in [Kra05].

4.2 Observation of Ultra-low Threshold Raman Lasing

To observe Raman lasing, silica microspheres are produced, with diameter in the range of few tens of micrometers. A prism is used to in- and out-couple light to the microsphere. The outcome of the prism is collimated via a lens, and sent to a spectrometer (Acton Research Spectra Pro 500i). A multimode fiber is held close to the microsphere to control the coupling between sphere and prism, and to measure the Q-factor. A schematic depiction of the experimental setup is shown in figure 4.3.

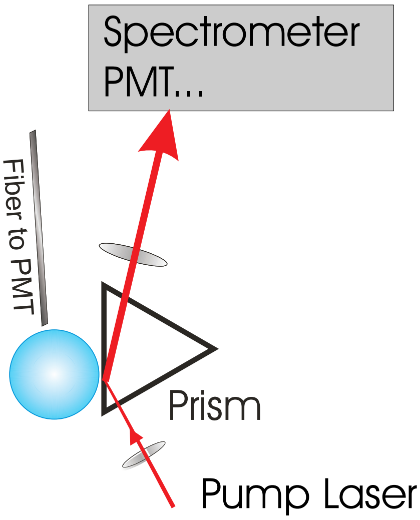

Figure 4.3: Scematic depiction of the experimental setup used for the observation of Raman lasing in a microsphere resonator.

A Ti:saphhire laser with a bandwidth of 500 kHz is used to pump the resonance. The laser is continuously scanned across the resonance. With a pump wavelength at λ_p =785 nm, the wavelength of the Stokes emission is expected to be at λ_S =814 nm. Filters are used to separate the pump light from the Stokes emission at the entrance slit of the spectrometer. First, a spectrum below and over threshold is recorded to make sure that the signal from the Stokes radiation is observable. While recording this spectrum an optical long-pass filter is used to select out the pump light. This is quite important to avoid artifacts in the spectrum which might be caused by the pump light. The result is shown in figure 4.4

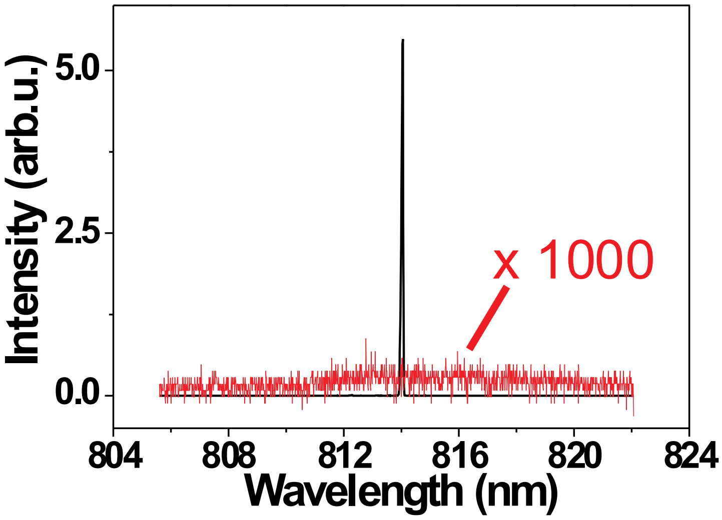

Figure 4.4: Spectrum of Raman lasing, recorded with pump power below (red curve) and above threshold (black curve). The spectrum taken at pump power below threshold is 1000 times amplified.

If the pump power is above threshold a distinct peak shifted by 13.4 THz from the pump frequency is observed. Below threshold only some scattered light is detected. The threshold behavior of the stimulated scattering process is then studied: the pump power is raised in small steps, and at each step a spectrum is recorded. The intensity of the lasing signal is then calculated from the area under the spectrum, while the pump power is measured just behind the prism (while the sphere is pulled away from the prism). A typical result of a threshold behavior is shown in figure 4.5.

For a sphere with a diameter of 70 μm and a Q-factor of 3×10^8 a threshold of only 7.5 μW could be observed. For spheres with Q-factors

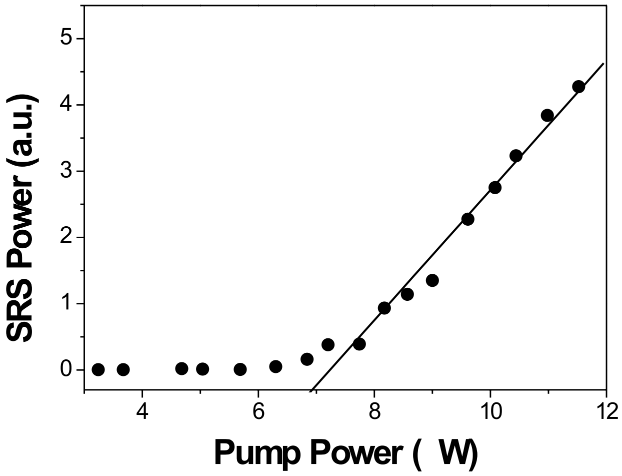

Figure 4.5: Stokes emission as function of the absorbed pump power. The signal is outcoupled via a prism and sent to a spectrometer. The imput pump power is measured just behind the prism. The used sphere has a diameter of 70 μm and a Q-fator of 3×10^8

exceeding 10^9, thresholds as low as 4.3 μW were detected. This value is the lowest threshold observed so far [1]. Next, the dependency of the threshold on the Q-factor of the sphere is measured. The sphere is moved closer and closer to the prism in order to change its Q-factor, and for each position the laser threshold is measured. The data are shown in figure 4.6, and show a very good superposition to the theoretical prediction calculated with the formula 4.1, shown by the red line in figure 4.6.

The lasing mode is found to have a well defined linear polarization, which follows the polarization of the pump laser. This was checked by inserting a polarizer at the entrance of the spectrometer when pumping above threshold, as shown in figure 4.7

In order to prove single mode operation of the laser, a mode mapping is performed following the procedure described in section 3.5. The setup is slightly modified, as shown in figure 4.8 in order to provide access to the microsphere for a SNOM probe.

Again, the laser is continuously scanned across a single WGM. The resonance is kept under control either by detecting the absorption dip in the transmitted pump beam, or by detecting the scattered light via the multi-

---

[1] Later, thresholds in the order of nW were observed in crystalline CaF_2 cavities [GM06]

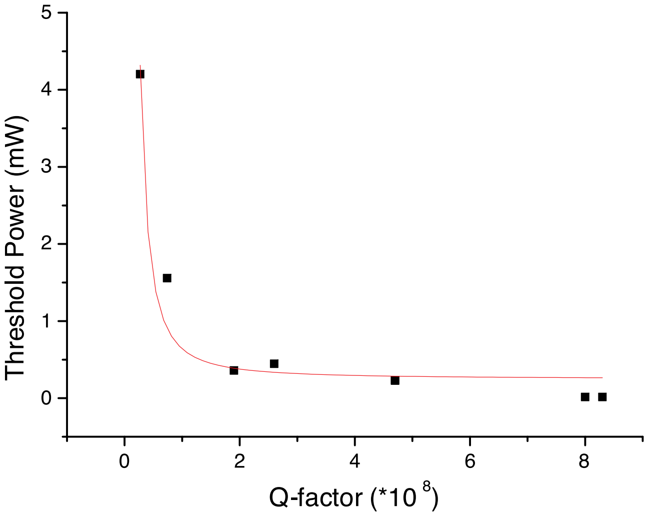

Figure 4.6: Threshold power as a function of the Q factor. The Q-factor is reduced by moving the microsphere towards the prism, and measured from the linewidth of the light detected by a multimode fiber held close to the microsphere.

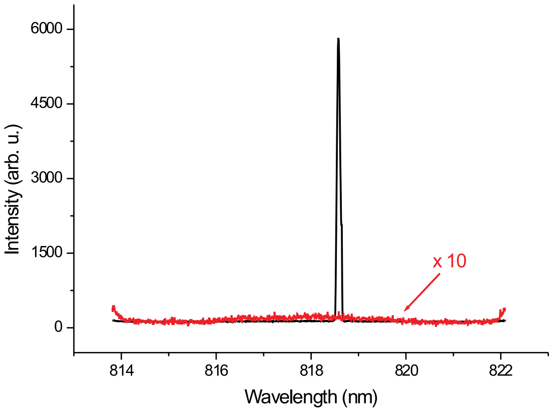

Figure 4.7: The lasing mode is linearly polarized, and has the same polarization as the pump mode (which is set to 0°). Red curve: spectrum with the polarizer set at 0°. Black curve: Polarizer set at 90°.

mode fiber. While scanning the laser a mode map is performed as described

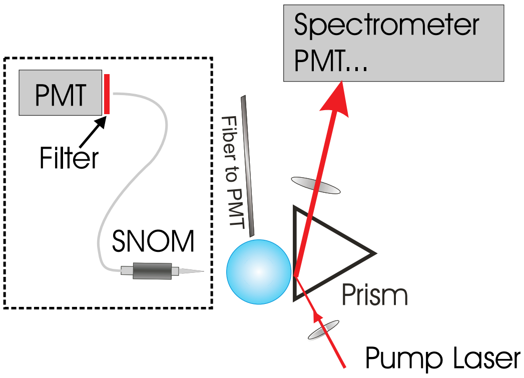

Figure 4.8: Setup for mapping the pump and lasing modes of a microsphere ultra-low threshold Raman laser.

in section 3.5. By using appropriate filters it is possible to detect the mode profile of the pump mode as well as of the lasing mode. Both the fundamental and the first order mode are investigated, and the results are shown in figure 4.9.

The first important result that one can observe from this measurement is that lasing is indeed single mode. In part a) and c) of figure 4.9 a mode map is shown with pump power below threshold. It is easy to identify scan a) with the fundamental mode, and scan c) with the first order mode, for which l-m=1. The red curve is the theoretical prediction for the polar intensity distribution obtained from the mode expression given in section 2.1, for the fundamental and for the first order mode respectively. Part b) and d) of figure 4.9 are mode maps detected by scanning the laser with a power of respectively 20 and 130 times the threshold pump power of 7.5 μW. It was carefully checked that all the pump light was filtered out in this measurement. As can be seen from the mode map shown in figure 4.9 the mode profile of the lasing mode is the same as of the pump mode which is expected by considering maximum mode overlap. Lasing mode profiles differing from the pump have never been detected, even for very high pump power. The only deviation that can be observed is at the intensity maximum of the lasing mode in the case of the fundamental mode. This deviation is due to the perturbation introduced in the mode by the near-field probe. In the following section this complicate interplay is theoretically modeled and compared to further experimental results.

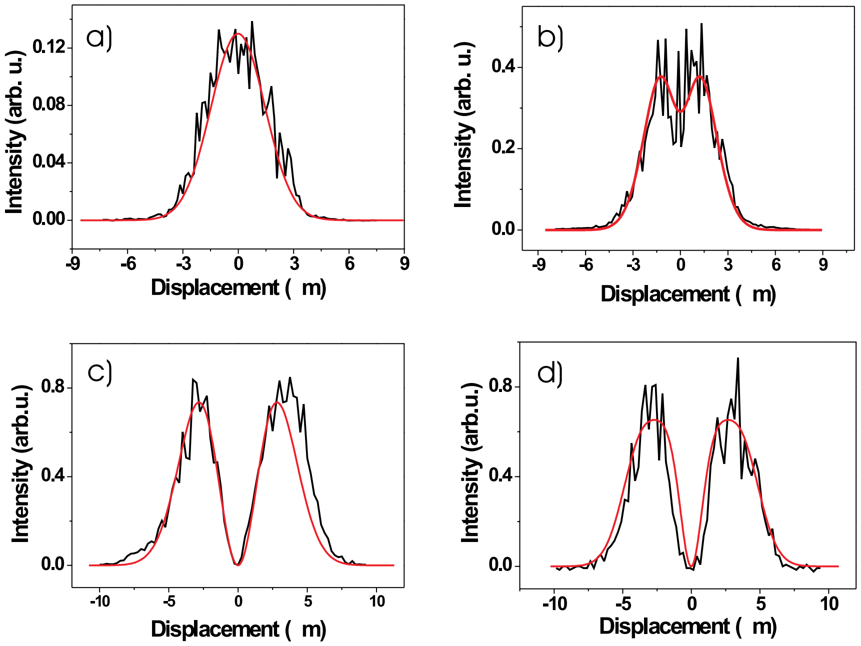

Figure 4.9: a) and c): mode maps of the pump modes; b) and d): mode maps of the lasing modes. In a) and b) one has $l - m = 0$ while in c) and d) one has $l - m = 1$. The pump power was 20 and 130 times $P_T = 7.5\,\mu W$, respectively. Red lines are theoretical fits.

4.3 Influence of a Controllable Scatterer on the Lasing Properties

4.3.1 Lasing Properties

Introducing a scatterer in the evanescent field of the WGMs automatically increases the losses in the cavity. This leads to a degradation of the Q factor, dependent on the dimension of the scatterer [GBS02] and on its position with respect to the mode profile. The total Q-factor of a microsphere can be calculated from all the different contributions to the losses as pointed out in section 2.1.1:

$$1/Q_{tot} = 1/Q_0 + 1/Q_\kappa + 1/Q_s(\theta) \tag{4.3}$$

In formula 4.3, Q_{tot} is the total Q-factor, Q_0 the intrinsic (absorption limited) Q-factor, Q_κ represents the contribution of the coupler, and Q_s is due to the scattering by the SNOM-probe. The dependence of Q_s on the probe position is easily inferred as $Q_s(\theta) = \overline{Q}_s/[H(l-m, \sqrt{l}\,cos\theta)sin(\theta)^l]$, with $H(n,x)$ being the normalized Hermite polynomial of order $l-m$ (which describes the intensity profile of the WGM in polar direction) and $\overline{Q}_s$ is the maximum reduction of the Q-factor. This means that the tip will influence the Q-factor mostly when it is positioned in the maximum of the mode, and will produce no effect if it is out of the evanescent field of the mode ($Q_s = \infty$). The threshold pump power given in equation 4.1 can be rewritten with an explicit dependence on θ in the following way [Kra05]:

$$P_T(\theta) = \Gamma \frac{4\pi^2 N^2 V_m}{g\lambda_p\lambda_s} \frac{Q_\kappa}{Q_{tot}(\theta)^3} \tag{4.4}$$

since the coupling-limited Q-factor Q_κ does not depend on the position of the tip. In an analog way, the intensity of the Stokes emission given in formula 4.2 has to be modified in the following way to take into account the position-dependent influence of the scatterer:

$$\begin{aligned} I_{out}(\theta) \propto \sqrt{\frac{Q_{tot}(\theta)}{Q_k}}(\sqrt{P_{in}} - \sqrt{P_T(\theta)})\times \\ \times H(l-m, \sqrt{l}cos(\theta))sin(\theta)^l U(P_{in} - P_T(\theta)). \end{aligned} \tag{4.5}$$

From these expressions one can see that the scatterer induced degrading of the Q-factor may have a great influence on the system. In fact, the Q-lowering will increase the threshold. This can even result in total quenching of the lasing activity. Plots of the expected lasing mode profile done with equation 4.5 are shown in figure 4.10 for the fundamental mode and for the first order mode.

To further investigate this phenomenon the pump power is reduced to only 5 times the threshold for the fundamental mode and 10 times the threshold for the first order mode. A mode map is then performed, the results being shown in figure 4.11. The red lines show the theoretically expected intensity profile, and fit very well to the experimental data. As one can see, the quenching of lasing activity occurs quite abruptly, with the intensity going to zero within a 0.5 μm shift of the tip.

4.3.2 SRS for Detecting Small Particles

The produced quenching of laser oscillation may be exploited for the detection of small particles. From the quenching intensity it is possible to derive the scattering rate of the quencher, and this gives information on the dimensions of the scatterer. Assuming a spherical scatterer with a radius r, the scattering cross section is given by

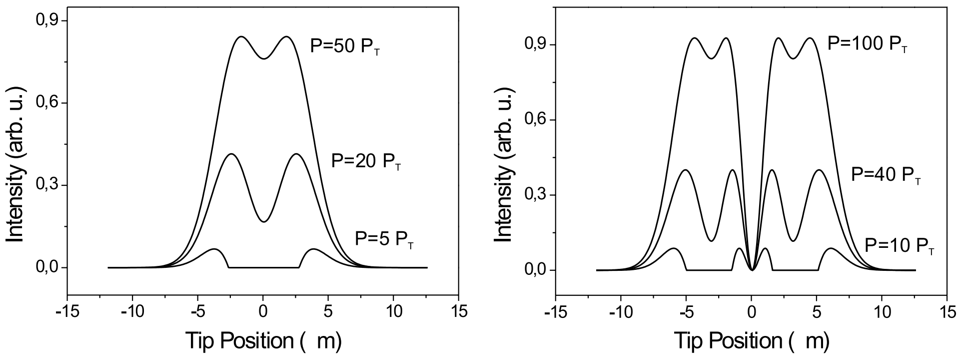

Figure 4.10: Expected fundamental (left) and first order (right) lasing mode profile for different pump powers when the tip is scanned through the mode. The quenching of the lasing intensity is caused by the Q-factor reduction induced by the tip itself.

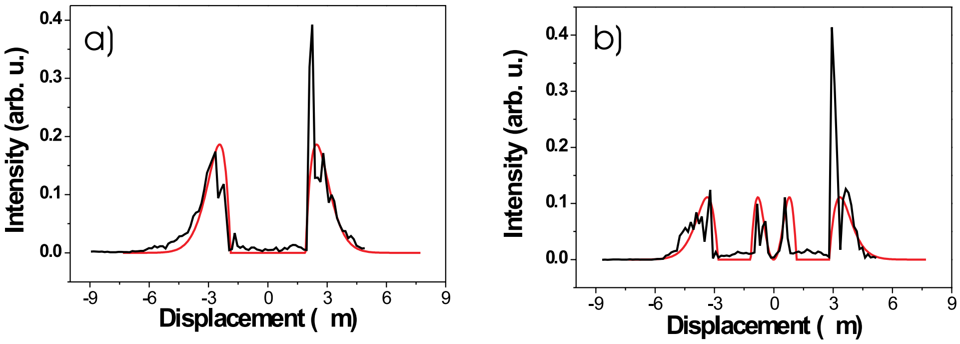

Figure 4.11: Quenching of the lasing activity caused by the controllable scatterer. In a) a mode map of the fundamental lasing mode is shown, at pump power 5 times the threshold power. In b) a mode map of the first order lasing mode is shown, at pump power 10 times the threshold.

$$\sigma(r) = \frac{8\pi}{3}\left(\frac{2\pi}{\lambda_S}\right)^4 r^6 \left|\frac{\epsilon-1}{\epsilon+2}\right|^2 \tag{4.6}$$

A model has been developed to estimate how much a spherical scatterer with a radius r would spoil the Q-factor of a microsphere in [Göt04], giving a qualitative understanding for the order of magnitude and for the dependencies of the quantities involved. It is assumed that the incident wave on the scatterer is a plane monochromatic wave. In a round trip the light travelling in a great circle around the equator will lose the energy ΔE when passing the scatterer. The loss can be expressed as the ratio of the areas:

$$\frac{\Delta E}{E_0} = \frac{\sigma \frac{I(d)}{I_0}}{A_{mode}} \tag{4.7}$$

where E_0 is the energy stored inside the resonator, A_{mode} is the cross section through the mode volume, $I(d)$ is the radial intensity distribution as described in section 2.3.1, normalized to the total intensity I_0. With some simple calculation one obtains the scattering decay constant τ_{sct} as

$$\tau_{sct} = \frac{t_{rt}}{-ln(1 - \frac{\sigma}{A_{mode}} e^{-2d/r^*})} \tag{4.8}$$

where r^* is the typical decay-length of the evanescent field and is given by the approximate expression $r^* \approx \lambda/2\pi \times \sqrt{1 - N^2}$. To account for this additional loss the Q-factor of the microsphere is modified by addition of the term

$$Q_{sct}(r, \theta) = \omega \tau_{sct}. \tag{4.9}$$

This can be combined with the formula 4.4 which provides the lasing threshold power. The threshold will be dependent also on the distance of the scatterer to the sphere's surface through the Q-factor induced by the scatterer:

$$P_T(\theta, r) = \Gamma \frac{4\pi^2 N^2 V_m}{g \lambda_p \lambda_s} \frac{Q_\kappa}{Q_{tot}(\theta, r)^3}. \tag{4.10}$$

The intensity of the laser emission will thus be reduced by a factor which is dependent on the distance of the scatterer from the surface in the following way:

$$\begin{aligned} I_{out}(\theta, r) \propto \sqrt{\frac{Q_{tot}(\theta, r)}{Q_k}} (\sqrt{P_{in}} - \sqrt{P_T(\theta, r)}) \times \\ \times H(l - m, \sqrt{l} cos(\theta)) sin(\theta)^l U(P_{in} - P_T(\theta)) \end{aligned} \tag{4.11}$$

Assuming a Poissonian statistics for the emitted Stokes photons, a reduction of intensity of 10% is greater than the least uncertainty, given by $\sqrt{I}$. With a microsphere with a Q-factor exceeding 10^8 it would possible to detect easily particles as small as 30 nm.

4.3.3 Estimation of Opto-mechanical Force

The strong intensity gradient observed when the laser is quenched by the insertion of a SNOM probe into the mode results in an opto-mechanical force acting on the probe itself. In figure 4.12 the change of the laser intensity versus the SNOM tip's position $\partial I(\theta)/\partial(r\theta)$ for the measurement of the fundamental mode (data in figure 4.12) is plotted. Due to the extension of the tip and the spatial mode profile the number of photons incident on the tip surface from either side per unit time is not equal. Thus, the recoil of the scattered photons produces a net force perpendicular to the optical equator of the sphere. The large intensity gradient due to quenching of laser emission therefore also gives rise to a large force gradient.

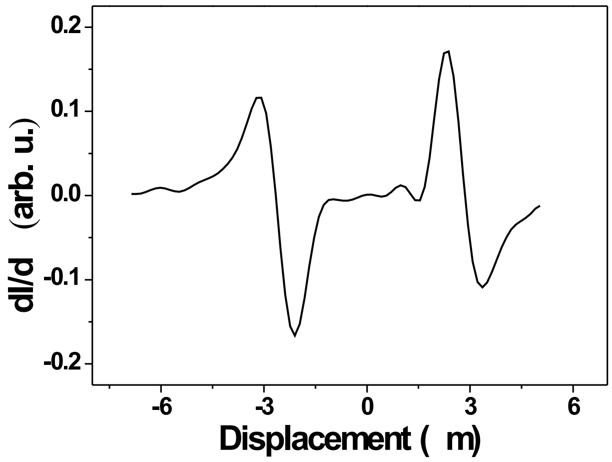

Figure 4.12: The intensity gradient as derived by derivation of the experimental data in figure 4.11 (a) is plotted. The data have been smoothed before derivation by application of a FFT filter to reduce noise fluctuations.

One can give an order-of-magnitude estimation of the light-induced force gradient or force rigidity [HMK04] $\partial F(\theta)/\partial(r\theta)$ by estimating the number of photons which are scattered from the SNOM tip per second: If the tip reduces the initial Q-factor by a factor of two, then approximately 50% of the incident power is scattered. Then the force acting on the tip can be expressed as

$$F = \Delta p R = 2\hbar k R = \frac{4\pi\hbar}{\lambda} R \tag{4.12}$$

where R is the scattering rate. This rate can be derived from the scattered power

$$R = P/\hbar\omega \tag{4.13}$$

so that one obtains

$$F = \frac{4\pi\hbar}{\lambda}\frac{P}{\hbar\omega} = \frac{2P}{c}. \tag{4.14}$$

Most of these photons hit the tip from the side facing the maximum of the mode profile. For our experiment, which was performed 30 times above threshold power, this corresponds to $\partial F(\theta)/\partial(r\theta) = 1.5\, pN/\mu m$. This rather large value should provide a significant mechanical back action on the mechanical oscillation of the tip. Our system may thus be used to study tiny opto-mechanical interaction, which have recently attracted much interested [HMK04].

Chapter 5

Photon Transfer via Shared Whispering-Gallery Modes

Spontaneous emission is the decay of an atomic excitation into the modes of the electromagnetic fields in the surrounding environment. If an excited atom or a classical dipole emitter is located on the surface of a microsphere its lifetime will be influenced by two main factors: the presence of the dielectric itself, which canalizes the emission along preferred directions, and the presence of a high-Q cavity with well defined modes. In this chapter the coupling of a single dipole to the high-Q modes of a microsphere resonator is investigated, and first experimental results concerning coupling of a single emitter are reported. Additionally, an application of the coupled system nanoparticle-resonator is demonstrated, where the whispering-gallery modes are used as an optical path for controlled photon transfer between two individual nanoparticles.

5.1 Emission of a Dipole on a Dielectric Interface: Geometric Approach

A first approach in considering the coupling of a dipole to the WGMs of a microsphere is based on simple geometrical considerations. Only photons which are emitted in directions which overlap to the WGMs will be able to resonate. One can try to define a maximum acceptance angle around the direction of propagation of the WGMs.

Geometrical Considerations on the Whispering-Gallery Modes

The geometry of the problem is described by the figure 5.1.

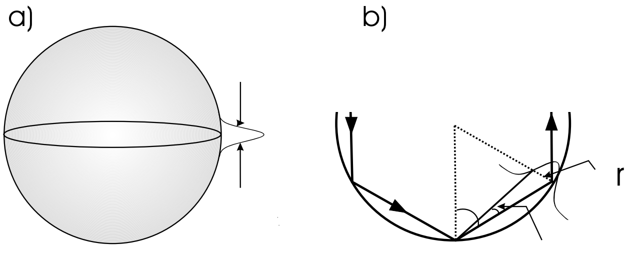

Figure 5.1: a): polar acceptance angle $\Delta\theta$; b): azimuthal acceptance angle $\Delta\alpha$

First, let's consider the polar direction: in a precessional mode approach for modes with $l - m > 0$, the acceptance angle is the same for all modes, and can be described as Gaussian beams having l/n reflections on the surface during one evolution inside the sphere, as shown in section 2.3.1. A simple approximation of the acceptance angle in the polar direction θ is the angular width of the Gaussian beam, which is approximated by [BS91]:

$$\Delta\theta \approx \sqrt{\frac{8}{l}}. \tag{5.1}$$

For example, for a sphere with a diameter of 35 μm it is $\Delta\theta = 10.5°$.

Slightly more difficult to define is an acceptance angle for the azimuthal direction (along ϕ). The condition necessary for a WGM to exist is that the number of reflections is a multiple of the wavelength, so that constructive interference can take place. Let γ be the angle defined by the mode: a photon which is launched into the sphere with an angle deviating by a quantity $\Delta\alpha$ by γ will undergo a phase shift $k\delta$, where $k = \frac{2\pi}{\lambda}$ is the wave vector and δ is the optical path difference. This can easily be calculated as:

$$\begin{aligned} \delta &= \lambda(\frac{1}{\cos\Delta\alpha} - 1) \\ \Rightarrow k\delta &= 2\pi(\frac{1}{\cos\Delta\alpha} - 1) \end{aligned} \tag{5.2}$$

In a round trip, that is after a number of reflection equal to l, the total phase shift $\Delta\phi = l\delta$ should be lower than π, otherwise the mode will interfere destructively. So in a round trip the following condition must be satisfied:

$$\Delta\phi = 2\pi l(\frac{1}{\cos\Delta\alpha} - 1) \leq \pi \tag{5.3}$$

It follows

$$\cos(\Delta\alpha) \geq \frac{2l}{2l+1} \tag{5.4}$$

which defines the acceptance angle in the azimuthal direction ϕ. Next, one has to calculate the overlap of the emission pattern of the dipole with the angular window defined above.

Emission Characteristics of a Dipole Close to an Interface

The problem of a dipole emitting close to a surface was treated first by Drexhage [Dre70], Tews [Tew74] and Silbey [CPS75], and was then extended by Lukosz [LK77]. Consider a dipole embedded in a loss-free medium 1, with an index of refraction N_1, located at a distance z_0 from the plane interface to a homogeneous medium 2, with an index of refraction N_2. Both media are linear, isotropic and nonmagnetic. The dipole orientation is described by the angle θ_0 between its axis and the z axis as sketched in figure 5.2.

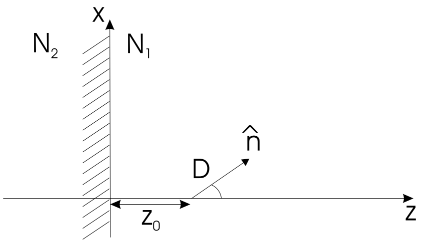

Figure 5.2: The dipole D in front of a plane interface between medium 1 and 2. The unit vector $\hat{n}$ lies in the $x - z$ plane.

The goal is to find the electromagnetic field of the dipole, which is oscillating at a fixed angular frequency ω. One can describe the field emitted by the dipole using two scalar functions, which are one component electric and magnetic Hertz vectors, and from which the field strengths derive. Both these functions have to be solutions of the Helmholtz wave equation with the proper boundary conditions. Without going too much into detail, which can be found in [LK77], one finds out that the dipole field is represented as a superposition of s- and p-polarized waves, and evanescent waves. In the medium 1 the dipole field is a superposition of the field emitted in the infinite medium 1 with the field reflected at the interface. In medium 2 the field is a superposition of plane waves which decay in direction $-z$, if the medium is absorbing. If the medium 2 is loss-free the waves are either homogeneous plane waves or evanescent waves. The evanescent waves emitted by the dipole decay exponentially in the half-spaces $z \geq z_0$ and $z \leq z_0$, and are thus present only in the dipole near-field. The energy transported by these waves is zero, since in the pointing vector $< \mathbf{S} >=< \mathbf{E} \times \mathbf{H} >$ there are contributions from two waves with equal and opposite wave vectors.

However, this holds only if the distance z_0 from the interface is larger than the decay length of the evanescent wave. If $z_0 \leq \lambda_1$ (where λ_1 is the emission wavelength of the dipole) and $N = N_2/N_1 > 1$, then evanescent waves with the proper $k-$vector can reach the interface. The refracted transmitted waves are then propagating plane waves with angle of refraction α exceeding the critical angle $\alpha_c = arcsin(1/N)$: in this way the dipole can effectively radiate energy into the denser medium 2.

Let the unit vector in the observation direction be $\widehat{k}$ with the components:

$$\begin{aligned}\widehat{k}_x &= \sin\alpha\cos\phi \\ \widehat{k}_y &= \sin\alpha\sin\phi \\ \widehat{k}_z &= -\cos\alpha, \end{aligned} \tag{5.5}$$

with α the angle between $\widehat{k}$ and the z axis, and ϕ the azimuth angle. The power emitted in the solid angle element $d\Omega = \sin\alpha d\alpha d\phi$ is denoted by $P^{s,p}(\alpha,\phi)d\Omega$, and is given by the sum of the s- and p-waves (since they do not interfere their contributions just sum up). The integration over the solid angle 4π yields the total power $L(z_0)$ radiated by the dipole at a distance z_0 from the interface, in units of the power L_∞ emitted by the dipole in the unbounded medium 1:

$$\int_{(4\pi)} [P^{(s)}(\alpha,\phi) + P^{(p)}(\alpha,\phi)]d\Omega = L(z_0)/L_\infty. \tag{5.6}$$

With this normalization one derives the final expression for the radiation pattern of dipoles in front of an interface, which are reported in [LK77]. Here only the plots of the expressions are shown in figure 5.3 in the case that the two media at the interface are air and silica glass.

It is apparent that there is a maximum in the emission along the critical angle α_c for total internal reflection. This is due to the presence of the interface, that transforms the evanescent waves emitted with the proper k-vector into propagating waves in the denser half-space. In the case of particular interest to the experiments of this work, where the interface is between air and glass, this critical angle is at $\alpha_c = 43.2°$. When determining the superposition of the emission with the whispering-gallery modes this plays a crucial role, as will become clear later. This effect, due to the evanescent part of the emission, also influences the total radiated power. The dipole will now radiate more than it would without interface. One can calculate this quantity for a dipole randomly oriented in space and close to the interface simply by integrating the area under the curves of figure 5.3. The result is

$$L(z_0 = 0)/L_\infty = 2.1 \tag{5.7}$$

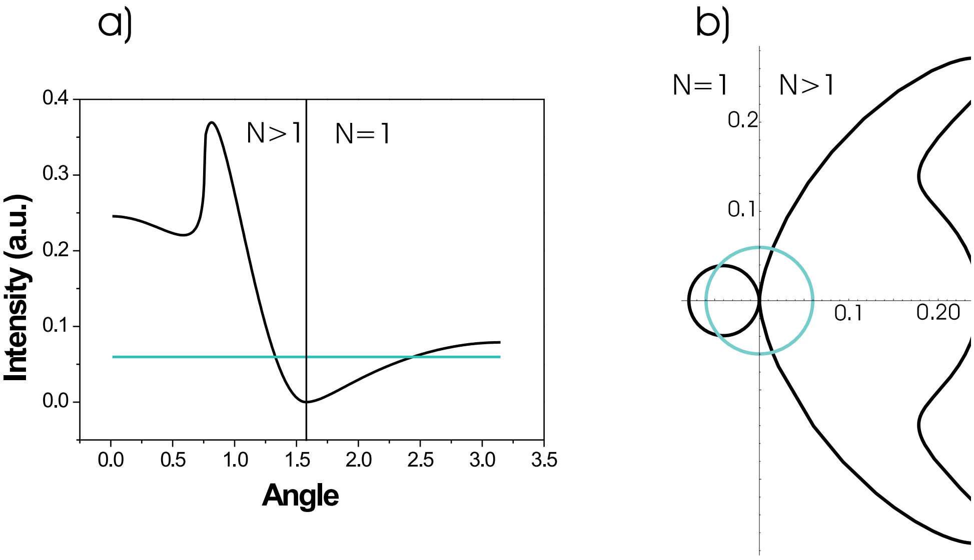

Figure 5.3: a) Black Curve: emission pattern of an ensemble of randomly oriented dipoles sitting at the interface. Green curve: emission pattern of the same ensemble of atoms in free space. b): same plot as in a) but in polar representation

The emitter would thus totally radiate 2.1 times more power than it would in free space.

5.1.1 Overlap of the Emission Pattern of a Dipole with the WGMs Profile

In the preceding section the geometry of the problem was discussed. By integrating over the acceptance angles defined in the former section it becomes possible to calculate how much of the power emitted by the dipole is emitted into the WGMs. First the overlap with the fundamental mode is calculated. There are two main orientations for the dipole, parallel or perpendicular to the sphere's surface. They are calculated separately. All the integrals are calculated with the help of Mathcad Professional.

For a dipole which is perpendicular to the surface there is an additional symmetry since the system is invariant under rotation around the ϕ angle. It is also easy to understand that in this case there will be no contribution from the *s*-polarized waves, since they correspond neither to TM nor to TE modes. Thus the fraction $\beta_\perp$ of power emitted into the WGMs, $P_{\perp,WGM}$

normalized to the total emitted power $P_{\perp,tot}$ (for a perpendicular dipole) is:

$$\begin{aligned}\beta_{\perp} &= \frac{P_{\perp,WGM}}{P_{\perp,tot}} \\ &= \frac{2\int_{\gamma-\Delta\alpha}^{\gamma} P_{\perp,2}(\alpha)d\alpha}{\int_0^{\alpha_c} P_{\perp,1}(\alpha)d\alpha + \int_{\alpha_c}^{\frac{\pi}{2}} P_{\perp,2}(\alpha)d\alpha + \int_{\frac{\pi}{2}}^{\pi} P_{\perp,out}(\alpha)d\alpha} \cdot \frac{\Delta\theta}{2\pi} \qquad (5.8)\end{aligned}$$

Where following notation is used:

- γ is the propagating angle of the whispering-gallery mode (see figure 5.1)
- α_c is the critical angle of total internal reflection defined as $\alpha_c = arcsin(\frac{1}{N})$ with N refraction index of the sphere;
- $P_{\perp,1}(\alpha)$ is the power emitted by the dipole inside the sphere, under the critical angle;
- $P_{\perp,2}(\alpha)$ is the power emitted by the dipole inside the sphere, above the critical angle;
- $P_{\perp,out}(\alpha)$ is the power emitted by the dipole outside the sphere.

To get an idea of the orders of magnitude let's consider a sphere with a radius of 25 μm, and look at the overlap of a dipole emitting at a wavelength of 610 nm. The geometrical restrictions are then $\Delta\theta \approx 8.4°$ and $\Delta\alpha \approx 3°$, while $\gamma = 89.5°$. This gives $\beta_{\perp} \approx 2.8 \times 10^{-5}$.

If the dipole is oriented parallel to the surface, one has to separate the contribution of s-waves and p-waves as $P_{\|}(\alpha,\phi) = 2cos^2(\phi)P_{\|,p} + 2sin^2(\phi)P_{\|,s}$, where ϕ is the angle between the dipole and the plane defined by the sphere's equator. Then one has for $\beta_{\|}$:

$$\begin{aligned}\beta_{\|} &= \frac{P_{\|,in}}{P_{\|,tot}} \qquad (5.9) \\ &= \frac{2\int_{-\frac{\Delta\theta}{2}}^{\frac{\Delta\theta}{2}} \int_{\gamma-\Delta\alpha}^{\gamma} P_{\|,2}(\alpha,\phi)d\alpha d\phi}{\int_0^{2\pi}\int_0^{\alpha_c} P_{\|,1}(\alpha,\phi)d\alpha d\phi + \int_0^{2\pi}\int_{\alpha_c}^{\frac{\pi}{2}} P_{\|,2}(\alpha,\phi)d\alpha d\phi + \int_0^{2\pi}\int_{\frac{pi}{2}}^{\pi} P_{\|,out}(\alpha,\phi)d\alpha d\phi}\end{aligned}$$

where the notation is used in analogy to 5.8. A calculation with the same sphere parameters gives a value of $\beta_{\|} = 5.1 \times 10^{-6}$.

The contributions of these two orientations have to be weighted to obtain the geometrical overlap of a dipole with an arbitrary orientation to the sphere's surface. This gives the following result for the fraction of power emitted by a dipole located at the interface to a microsphere resonator with arbitrary orientation:

$$\beta = \frac{1}{3}\beta_{\perp} + \frac{2}{3}\beta_{\|} = 1.3 \cdot 10^{-5}. \tag{5.10}$$

5.2 Emission of a Dipole on a Dielectric Interface: Modal Approach

The former analysis is an underestimation of the coupling efficiency. In fact, any influence of resonant enhancement due to the presence of the cavity is neglected. Since the WGMs form a complete basis, it is possible to expand the function expressing the dipole emission as a superposition of WGMs. This method was first used by R. Ruppin and [R.R82] to calculate the transition rates of molecules close to a small metal sphere. A few years later H. Chew and successively J.P Barton extended the method to dielectric sphere[Che87, BAS88]. This procedure has also been exploited to calculate the relative frequency shift and linewidth of an atom near a dielectric sphere by V.V. Klimov et. al in [KDL96]. Also based on this method is a proposal of M. Pelton [PY99] for the realization of an ultra-low threshold laser with a single quantum dot coupled to a spherical microcavity. The basic idea is to calculate the coupling factor based on the ratio of the power radiated by one single whispering-gallery mode to the total radiated power of a dipole in free space. The emitter finds itself at a distance d from the sphere, and is considered to emit spherical waves (this is equivalent to saying that the dipole has a random orientation). Then the electric field of the dipole can then be written as

$$E_0 = \xi_0 \frac{1}{|\vec{r}|} e^{i\vec{k}\cdot\vec{r}} \tag{5.11}$$

with ξ_0 amplitude of the field. The radiated power in this case is just

$$P_0 = \frac{1}{2} c_0 \epsilon_0 \int |E_0|^2 d\vec{r} = \frac{1}{2} \epsilon_0 |\xi_0|^2 4\pi c_0 \tag{5.12}$$

where ϵ_0 is the dielectric constant in vacuum and c_0 the speed of light in vacuum (see for instance [Jac89]). Following the procedure given in the paper of J.P. Barton [BAS88] one can calculate which WGMs are excited by such a field. The approach is to represent the electric and the magnetic fields $E(r, \theta, \phi)$ and $H(r, \theta, \phi)$ via a single respective scalar potential $\Pi(r, \theta, \phi)$ which satisfies the Helmholtz equation

$$\nabla^2 \Pi + k^2 \Pi = 0 \tag{5.13}$$

in a similar way as was done in section 2.2.1. The difference is that now the excitation is a spherical wave. The most general solution to this problem is given by [BAS88]:

$$r\Pi(r,\theta,\phi) = \sum_{l=0}^{\infty}\sum_{m=-l}^{l}[A_{lm}\psi_l(kr) + B_{lm}\chi_l(kr)]Y_{lm}(\theta,\phi) \tag{5.14}$$

where k is the wave vector, A_{lm} and B_{lm} are arbitrary constants, ψ_l and χ_l are the Riccati-Bessel functions and $Y_{lm}(\theta,\phi)$ is the spherical harmonic function (see for example [BW64]). From this expression one can calculate the scattered and the internal electric field. The field of a resonator mode is given by:

$$E_{ms}(r,\theta,\phi) = \frac{1}{r^2}l(l+1)c_{ll}\psi_l(k_{int}r)Y_{ll}(\theta,\phi) \tag{5.15}$$

where the k-vector outside the sphere k_{ext} is related to the k-vector inside the sphere by $k_{int} = Nk_{ext}$ (with N being the index of refraction of the sphere). The coefficient c_{ll} can be written as $c_{ll} = \mathfrak{F}\cdot C_{ll}$, where $\mathfrak{F}$ is a linear combination of spherical Bessel functions:

$$\mathfrak{F} = \frac{\zeta_l^{(1)'}(k_{ext}a)\psi(k_{ext}a) - \zeta_l^{(1)}(k_{ext}a)\psi'(k_{ext}a)}{n^2\psi(k_{int}a)\zeta_l^{(1)'}(k_{ext}a) - n\psi'(k_{int}a)\zeta_l^{(1)}(k_{ext}a)} \tag{5.16}$$

where $\zeta_l = \psi_l - \imath\chi_l$. Similar as in section 2.2.1, this factor $\mathfrak{F}$ derives from the matching conditions of the electromagnetic field at the interface between the sphere and the surrounding medium, in this case air (similar as in section 2.2). The factor $\mathfrak{F}$ determines the resonances of the WGM (the primes indicate derivation with respect to the argument), and C_{ll} is a coefficient which takes into account the incident field:

$$C_{ll} = \frac{a^2}{l(l+1)\psi_l(k_{ext}a)\int_0^{2\pi}}\int_0^{\pi}\sin\theta E_0(a,\theta,\phi)Y_{lm}^*(\theta,\phi)d\theta d\phi. \tag{5.17}$$

In calculating $\mathfrak{F}$ the imaginary part of the refractive index plays an important role, since it is the parameter that accounts for the losses of the sphere, i.e. the resonator Q-factor.

The power loss P_{ms} by a whispering-gallery mode in a microsphere resonator of Q-factor Q is given by the loss rate $\frac{2\pi c_0}{\lambda Q}$ (where c_0 is the speed of light in vacuum and λ the propagating wavelength) times the energy density. Thus:

$$P_{ms} = \frac{1}{2}\epsilon_0\epsilon\frac{2\pi c_0}{\lambda Q}\int|E_{ms}|^2d\vec{r}. \tag{5.18}$$

For a microsphere of radius a this will lead to the following expression for the fraction β of power radiated into one whispering-gallery mode:

$$\beta = \frac{P_{ms}}{P_0} = \frac{1}{2\lambda_0 Q}\frac{a^4}{|\psi_l(k_{ext}r)|^2}|\mathfrak{F}|^2\left|\int\frac{e^{i\vec{k}(\vec{r}-\vec{d})}}{|\vec{r}-\vec{d}|}\xi_0 Y^*_{ll}d^3r\right|^2\int\frac{|\psi_l(k_{int}r)|^2}{|r^2|}dr \tag{5.19}$$

While the factor $\mathfrak{F}$ can be calculated with mathematica, the integrals of equation 5.17 are a bit more cumbersome, and were evaluated with a Pascal numerical integration recipe. The dependency of the separation of the dipole to the sphere surface d enters into this term. It can be calculated for different values of d. The result is shown in figure 5.4.

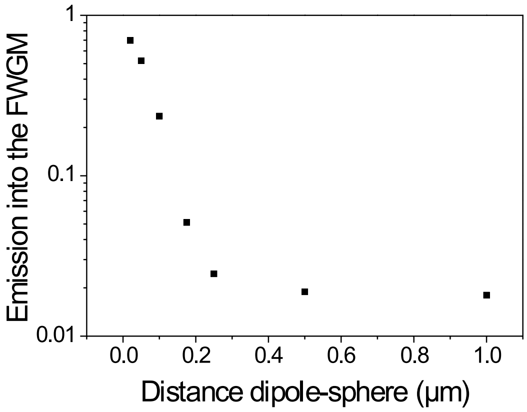

Figure 5.4: Calculated dependence of the β-factor for the fundamental whispering-gallery mode (FWGM) on the emitter separation from the microsphere

It is apparent that the closer the dipole is to the sphere, the more it will emit into the mode of the cavity. It is also clear that the coupling efficiency decays exponentially with increasing distance from the surface. It is important to stress at this point that this calculation holds only for a narrow-band emitter, which spectrally matches the mode of the cavity.

5.3 Controlled Coupling of a Single Nanoparticle to the Whispering-Gallery Modes

The previous calculations show that to efficiently couple a dipole to the modes of a resonator it is very important to have as much control as possible over the position of the dipole itself with respect to the resonator. Coupling of active material to high-Q whispering-gallery mode resonators has already been reported [VFG+98, FLW99], and even lasing [STH+96, CMA+01] or strong coupling of a single atom has been reported [ADW+06]. These experiments, however, all suffered from the deficiency of not being able to control the position of the emitter in the cavity. An ideal tool to have nanometer precision in the positioning of small particles is a near-field probe, where a particle can be attached at the very end of the tip. Such an active probe can be produced in a relatively easy way depending on the dimensions of the particle, as described in section 3.3.2. In this section, active probes with beads (polystyrene spheres, which can be doped with dyes) with diameter down to 100 nm have been produced, and the controlled coupling of these particles to the high-Q WGMs was studied. Some results have been already shown and discussed in [Göt04]. There it is shown how an active probe can be controllably coupled to the high-Q modes of a microsphere by positioning it in the evanescent field of the modes. Here, the goal is to have a better understanding how an ensemble of dipoles localized to sub-wavelength dimension couples to the whispering-gallery modes: for instance to how many modes the bead will couple, and if it is possible to experimentally determine the β factor (as it was defined in section 5.1.1).

In this experiment a dye-doped bead of 200 nm in diameter (doped with Red Fluorescent dye molecules, Molecular Probes Inc.) is used, attached to the end of a near-field probe as described in section 3.3.2. The active probe is then brought into proximity with a microsphere resonator with a diameter of 30 μm, which is coupled to a prism. The experimental setup is shown in figure 5.5.

The bead is excited via the SNOM fiber. Its fluorescence can be detected either via the confocal microscope or, if it couples to the whispering-gallery modes, via the prism.

The following experiment is performed: with the tip far away from the sphere, the bead is pumped and its spectrum is recorded via the microscope. Then, the excitation is turned off, the tip is approached and positioned in the maximum of the fundamental mode. The excitation is now turned on again and a spectrum is recorded, again via the microscope. The result is shown in figure 5.6.

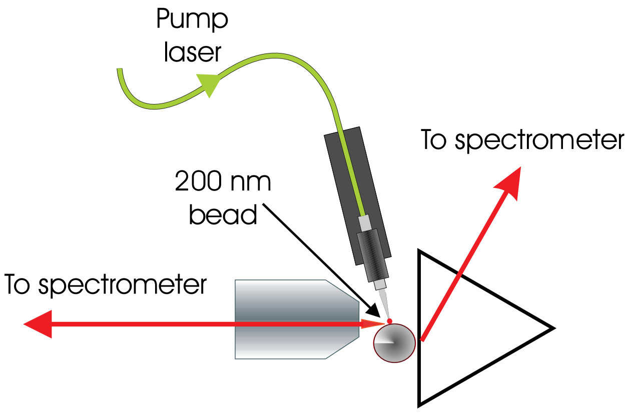

Figure 5.5: Experimental setup for studying the coupling of a single nanoemitter to the high-Q modes of a microsphere resonator

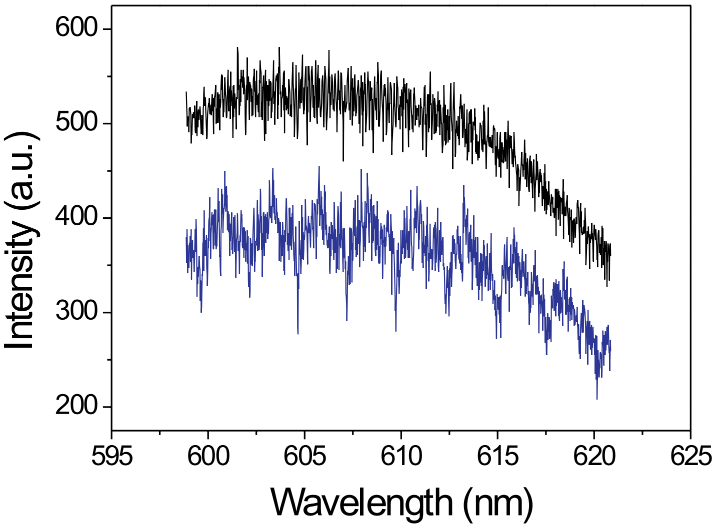

Figure 5.6: Spectrum of a dye doped bead far from the sphere (black curve) or brought close to its surface (blue curve). It is clear that the emission of the nanoparticle undergoes a dramatic change when approached to a microsphere.

It is apparent that when the bead is in proximity of the microsphere the spectrum undergoes a dramatic change. First, there is a reduction of the overall intensity emitted into the free space, as can be also observed in figure

5.6: this can be understood in terms of interference of the dipole emission with the emission of an image-dipole sitting inside the sphere. Second, a modulation appears. The origin of this modulation is the interaction with resonant modes of the microsphere. An enhanced intensity is observed from the light that is stored inside the modes of the resonator and scattered back in the direction of the objective by the bead itself. It is important to note that the emitter used in this experiment has a broad fluorescence spectrum. Thus, it can couple to any mode within the spectral range. The previous chapter has also shown that the geometrical coupling efficiency to an individual mode such as the fundamental whispering-gallery mode is quite small. Therefore it is important to consider also the coupling efficiency to lower order modes. A first hint that the dipole could also couple to other modes becomes clear if one looks at the emission pattern which has been calculated in section 5.1 (figure 5.3). Most of the emission is directed in a cone around the critical angle (defined by the refractive index N: $\alpha_c = arcsin(\frac{1}{N})$). In the case of silica glass, which was used in this case, the critical angle is $\alpha_c = 43.2°$: one might expect the particle to emit preferentially into modes which propagate along this angle α_c. Since this modes have an angle of $\approx 45°$ with respect to the sphere, they could form a closed square mode in one round trip, as depicted in figure 5.7. One can calculate the percentage of dipole emission which would

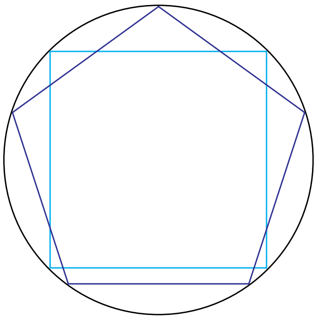

Figure 5.7: In a microsphere cavity not only high-Q whispering-gallery modes can exist, but also modes which are given by a very low number of reflections, e.g. modes propagating along a square trajectory, or a pentagon.

couple to these modes by using the simple geometrical approach similar as that used in 5.1. It is found that about 7% of the dipole emission would couple to these modes. Due to the low Q of these modes resonant enhancement is weak. The FSR for such modes can be calculated as $FSR_{square} = \frac{c}{LN}$, where L is the perimeter of the square. Since $L = 4R\sqrt{2}$, one can compare this to the FSR of the "normal" whispering-gallery modes, and it is:

$$\frac{FSR_{WGM}}{FSR_{square}} = \frac{c}{2\pi RN}\frac{4R\sqrt{2}}{c} = 0.9 \tag{5.20}$$

To gain a better understanding of the coupling process to different modes an additional measurement is performed: the bead is brought again close to the microsphere, pumped, and a spectrum is recorded via the prism and via the microscope. Since the prism is optimized to couple to the high-Q modes, one can be sure that the light detected via the prism is fluorescence of the bead which has coupled to the high-Q whispering-gallery modes. The result is shown in figure 5.8. The blue curve is the spectrum recorded via the prism, while the black curve shows the spectrum recorded via the microscope. Both spectra are recorded while the bead is pumped with the same intensity.

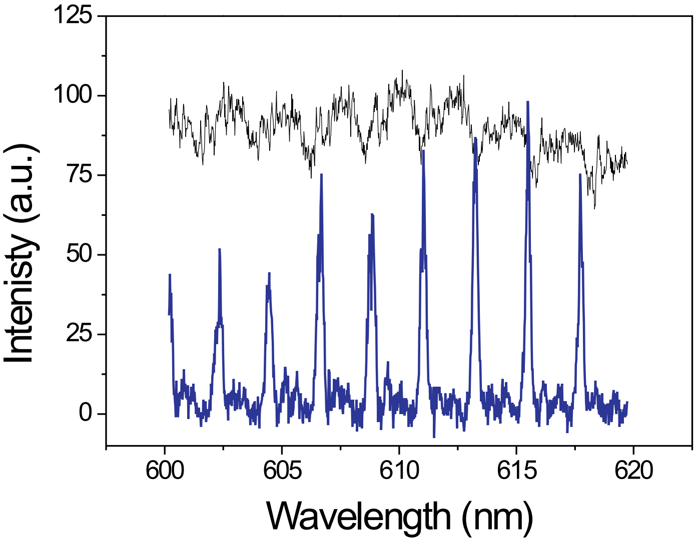

Figure 5.8: Black line: spectrum of a nanoparticle close to the surface of a microsphere resonator recorded via the confocal microscope. Blue line: same spectrum as it appears when the fluorescence is detected via the prism coupler.

The spectrum detected via the prism shows a 100% modulation, as expected since the prism extracts only light coming from the whispering-gallery modes. The spectrum recorded via the microscope shows a similar modulation. With a Fourier-transform one can calculate the FSR of fluorescence light detected via the prism of the peaks to be 2.24 nm, while the FSR of fluorescence light detected via the microscope objective is 2.49 nm. Their ratio is $\frac{2.24}{2.49} = 0.9$, which fits well with the expected value. This means that the nanoparticle will couple not only to the high-Q modes, but also to a large number of modes which cannot be ascribed to the whispering-gallery mode family. An important result of this measurement is that the dynamics of a broad-band nanoemitter will not be influenced significantly by high-Q WGMs. Rather, dominant coupling occurs to geometrical modes, which feature a lower Q-factor. In order to obtain coupling only to the high-Q WGMs, e.g. to observe CQED effects, a narrow-band emitter is required, e.g. molecules at cryogenic temperature.

5.4 Controlled Photon Transfer via Shared High-Q Modes

Somewhat unexpectedly after the conclusions of the previous chapter, high-Q WGMs may very well play an important role in optical processes involving broad-band emitters even at room temperature. Here an experiment is demonstrated, where the whispering-gallery modes are used as an optical link to let two nano-particles interact with each other. The motivation for this experiment derives from fluorescence resonant energy transfer processes (FRET): consider two dipoles, the emission spectrum of the first (called donor) overlapping the absorption spectrum of the second (called acceptor): the ideal situation is shown in figure 5.9. If the distance between the dipoles is on the order of few nanometers, significantly less than the transition wavelength λ, then the excitation of the donor can be transferred directly to the acceptor via dipole-dipole interaction (i.e. in a non-radiative way). The acceptor then relaxes radiative emission of the absorbed energy. The efficiency of such an energy transfer process depends on the spectral overlap of the two emitters, and in a very critical way on the distance between donor and acceptor, since it decays as $(1 + \frac{r}{r_0}^6)^{-1}$ and falls to 50% at a distance $r_0 = 10$ nm [F̈65]. If the two particles are taken apart at a distance $r > \lambda$, a transfer process can still take place, but a real photon is transferred: the donor emits a photon, which can be absorbed by the acceptor. The coupling efficiency in this case drops as $\frac{1}{r^2}$. At a distance of 50 nm, the efficiency of one emitter absorbing a photon radiated by another emitter is as low as merely 3×10^{-13}, considering a typical room-temperature absorption cross section of $\sigma_A \approx 10^{-16}$ cm^2. Even by using optical elements such as lenses or waveguides in order to increase the transfer rate, one still has the disadvan-

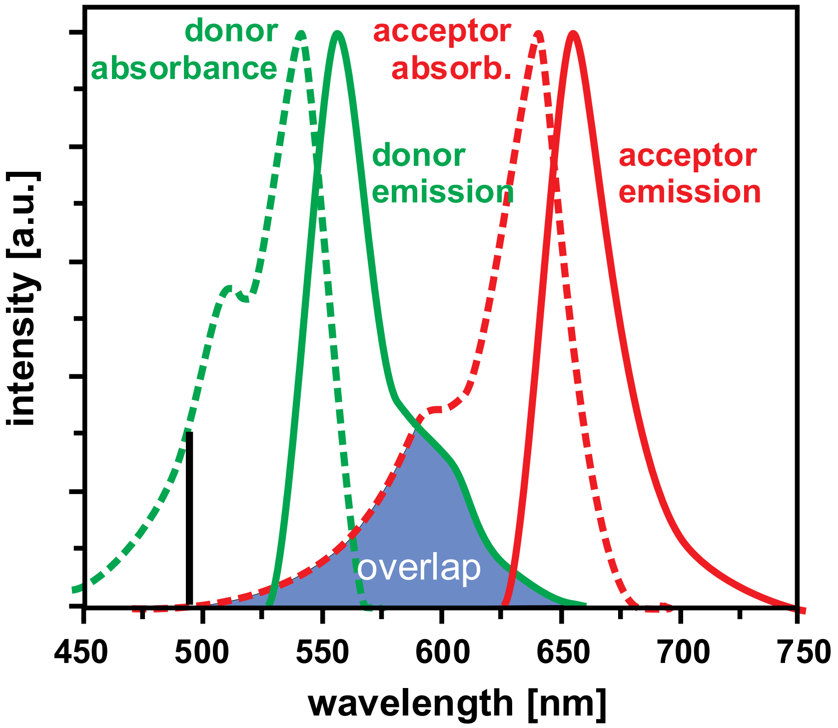

Figure 5.9: Ideal situation for a donor/acceptor couple: the spectral overlap is enough to result in efficient energy transfer, and it is possible to excite the donor at a frequency which is not absorbed by the acceptor, as indicated by the black line.

tage that the photon emitted by the donor flies by the acceptor only once. A resonant structure, however, can then be exploited to provide longer effective interaction times. In a naive picture, consider a microsphere with a Q-factor of 10^7 and Finesse of 10^6 . This means that a photon in the cavity travels 10^6 round trips before escaping the cavity. If the photon has been emitted by a donor, and an acceptor is also interacting with the cavity, this would mean that the photon passes the acceptor 10^6 times - and one could expect the transfer rate to be increased by a factor of 10^7! In addition, the presence of the cavity modifies the density of states of the electromagnetic field, which may further enhance the transfer rate.

Experimental Setup for Photon Transfer

A controlled experiment to study energy transfer via shared modes of an optical microresonator is depicted in figure 5.10. The donor particle is a

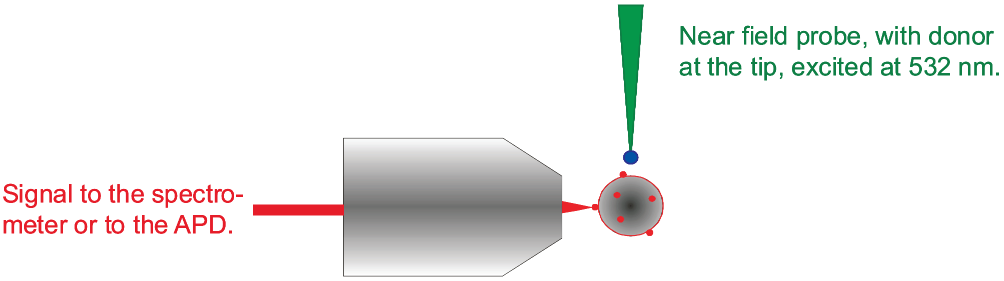

Figure 5.10: Setup for photon transfer experiment. A donor bead is attached to the end of a near-field probe and hold close to a microsphere resonator, which is coated by acceptor particles. The donor is pumped via the SNOM-fiber, its fluorescence couples to the high-Q modes of the resonator and can be absorbed by the acceptor. The detection is done confocally at the position of a single acceptor nanoparticle via a confocal microscope.

bead of 500 nm in diameter, attached at the end of a near field probe, and excited via the fiber by a frequency doubled Nd:YAG laser. A microsphere resonator of 35 μm in diameter is coated with a solution of acceptor beads (Crimson, Molecular Probes, Inc.) of 200 nm in diameter. After coating there was a total of less than 10 particles on the surface of the microsphere. This is important because one wants to avoid having more than one acceptor in the evanescent field of the modes. In figure 5.11 spectra of the naked donor and acceptor molecules are shown. They constitute a good donor-acceptor pair since they are well distinguishable but at the same time have a good spectral overlap. A single nanoparticle close to the sphere equator is located

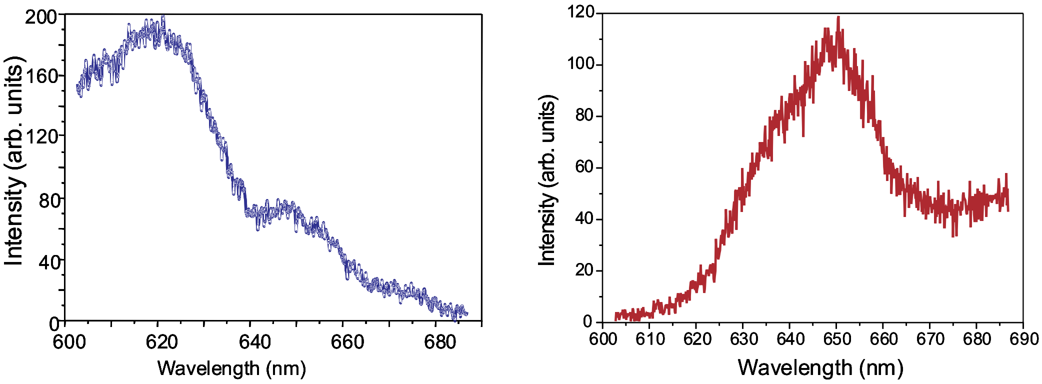

Figure 5.11: Left: spectrum of a Red Fluorescent bead when pumped at a wavelength of $\lambda = 532$ nm. Right: spectrum of a Crimson bead when pumped at a wavelength of $\lambda = 532$ nm.

and centered in the confocal detection path of the spectrometer (see Figure 5.10).

The experiment proceeds as follows: the tip with the donor bead is brought within a distance of a few nanometers from the sphere's surface, and excited via the SNOM-fiber by the frequency doubled Nd:Yag laser emitting at $\lambda = 532$ nm. The emitted photons that couple to the WGMs can be absorbed by the acceptor. To detect this the fluorescence emitted at the position of the acceptor is detected confocally. First, the signal is sent to an avalanche photodiode: the tip is then pulled back while recording the signal. As can be seen in fig. 5.12 the intensity of the fluorescence decreases exponentially. This is a typical signature for evanescent coupling to the WGMs.

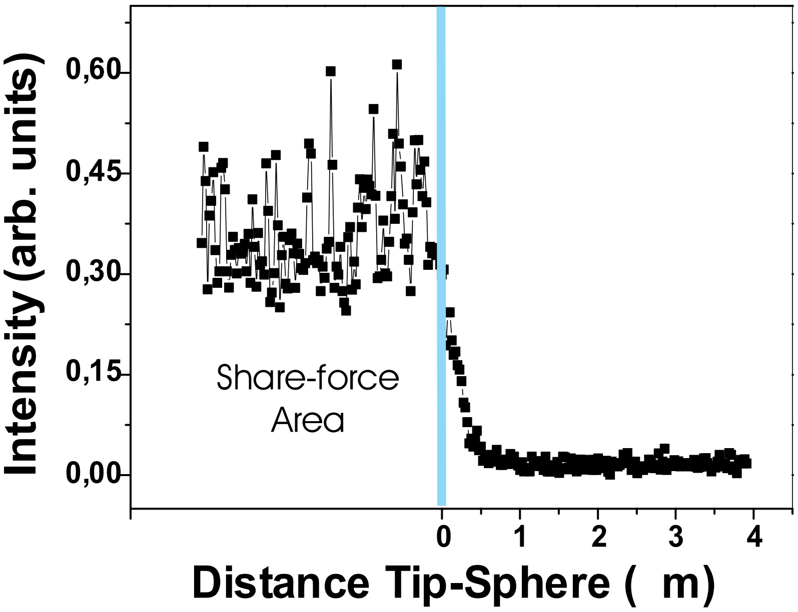

Figure 5.12: In this measurement the evanescent nature of the coupling of the two beads is shown. The tip with the donor bead is pulled away from the resonator, while the donor bead is kept under constant excitation. The signal detected confocally at the position of the acceptor is detected via an avalanche photodiode and plotted as a function of the distance of the donor bead to the sphere's surface.

The tip is then brought close to the sphere's surface again, but this time the signal is sent to a spectrometer. The recorded signal is shown by the red curve in figure 5.13. The spectrum shows a fast modulation, with a period which fits the FSR of the WGMs of the microsphere (2.3 nm for a sphere diameter of 35 μm). This is also a typical signature of coupling to the WGMs. The red curve is the sum of three contributions:

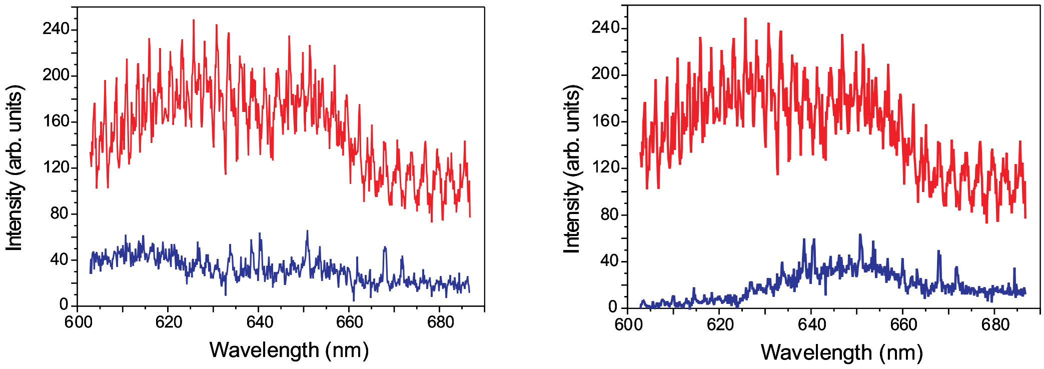

Figure 5.13: Left: Red curve: the recorded spectrum when the donor is brought close to the sphere's surface. Blue curve: the same measurement when the tip is pulled away from the sphere. Right: red curve: the recorded spectrum when the donor is brought close to the sphere's surface. Blue curve: the same measurement after bleaching of the donor

1. Photons emitted by the donor bead which have coupled to the modes and are directly scattered by the acceptor and detected via the microscope;
2. Photons emitted by the acceptor bead after absorption of photons emitted by the donor into the WGMs;
3. Photons emitted by the acceptor bead after direct excitation by some spurious green light from the excitation laser for the donor.

When the tip is at a distance of about 800 nm from the sphere's surface and the pump laser is turned on, only the signal shown by the blue curve in fig.5.13 a) is detected. Together with the measurement shown in figure 5.12, this confirms that the acceptor bead is pumped only through the modes of the microsphere. To distinguish the contribution in point 2 (which is the photon transfer process), from the one on point 3, the following control measurement is performed: the donor bead is taken away from the microsphere and then bleached by pumping at high intensity until fluorescence can be no longer detected. The tip with the photobleached donor is then approached again to the sphere and the pump light is turned on. The measured spectrum is shown by the blue curve in figure 5.13 b): it is clear that this contribution can be neglected in comparison with the red spectrum. As a last control, a normalized spectrum of the donor bead is subtracted form the red curve in figure 5.13: this results in the green spectrum of figure 5.14. In this figure a spectrum of the naked acceptor (brown curve) is also shown for comparison: the good overlap is evident. This controls prove that othe fluorescence emitted by the acceptor was truly excited by the donor's fluorescence which coupled to the WGMs and was guided to the acceptor.

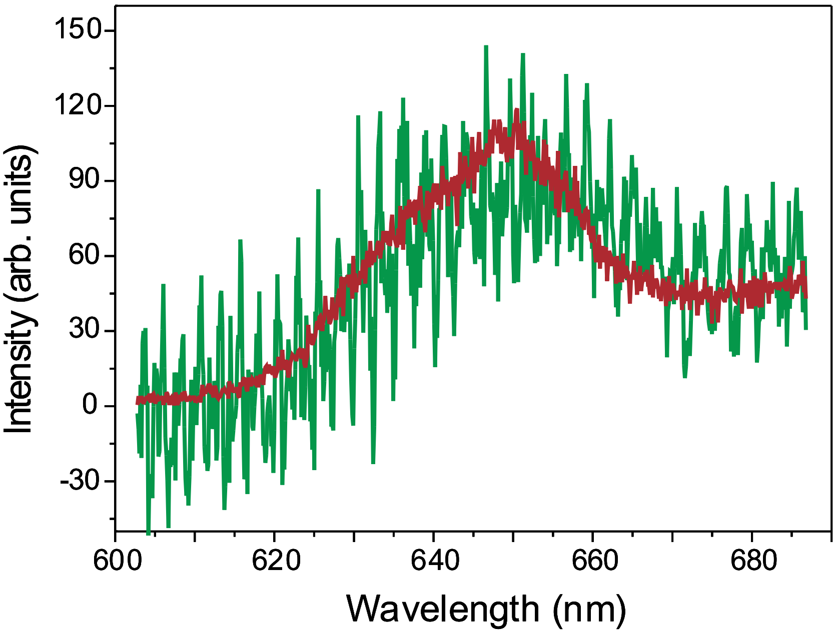

Figure 5.14: The green spectrum is obtained subtracting the spectrum of a donor as shown in figure 5.11 from the red spectrum of figure 5.13. This overlaps very well the spectrum of the naked acceptor (brown curve). The modulation comes from coupling to the whispering-gallery modes

Considerations on the Efficiency

It is interesting now to estimate the transfer efficiency, η_i, of the process. This can be defined as the product of the probability, β_i, of emitting a photon from the donor into the i-th WGM and the probability of subsequently absorbing it from the acceptor. This probability β_i has been calculated as in the previous section for the fundamental WGM. This efficiency, η_i, for a photon that is emitted by the donor to be absorbed by the acceptor can be written as

$$\eta_i = \beta_i \frac{\sigma_{A,abs}}{\sigma_{A,abs} + \sigma_{A,scat} + \sigma_{D,abs} + \sigma_{D,scat} + \sigma_{i,Q}} \tag{5.21}$$

where the quotient stands for the probability of a cavity photon being absorbed by the acceptor before getting lost in other channels. Note that because the emission and absorption processes are independent, a simple multiplication of probabilities is appropriate. The parameter $\sigma_{A,abs}$ denotes the absorption cross section of the acceptor, and $\sigma_{A,scat}$ denotes the scattering cross section of the acceptor, whereas cross sections $\sigma_{D,abs}$ and $\sigma_{D,scat}$ quantify losses out of the mode due to respectively absorption and scattering of a photon by the donor. Finally, $\sigma_{i,Q}$ is a cross section signifying all losses associated with the measured Q of the microsphere, including those caused by scattering from the acceptor. The crucial role of the high-Q modes in this experiment is to increase the absorption probability by storing the photon for a long time. Such an effect is absent if light is transferred merely by a waveguide or optical fiber. The cross sections used in equation 5.21 are, strictly speaking, defined for evanescent illumination, and differ from those commonly quoted for plane wave excitation. The deviation between the two quantities can be notable, but it has been shown that it remains well within a factor of 3, even for strongly scattering silver particles of 200 nm diameter at plasmon resonance [QPW99]. Thus, in this case it is appropriate to use the conventional values of the cross sections to obtain an order of magnitude estimate.

The absorption cross section of the acceptor particle can be taken as $\sigma_{A,abs} = 10^{-11}$ cm^2, assuming $\sigma_{A,abs} = 10^{-16}$ cm^2 per molecule and 10^5 molecules per particle. Since, due to the Stokes shift of molecular fluorescence, the donor does not absorb its own emission very efficiently, we can neglect $\sigma_{D,abs}$. In addition, we obtain $\sigma_{i,Q} = 10^{-12}$ cm^2 for a fundamental mode based on a Q-factor of 3×10^7 (here also $\sigma_{A,scat}$ is taken into account). Because in this experiment the measured Q remained unchanged as the tip approached the microsphere, it can be concluded that $\sigma_{D,sca}$ was negligible compared to σ_Q. One finds, therefore, that for a fundamental mode the quotient in equation 5.21 is about 10^{-4} with regard to a single molecule acceptor.

In the weak coupling regime, the spontaneous emission rate Γ can be written as $\Gamma = \frac{2\pi}{\hbar^2}|\langle e|\ \mathbf{E}\cdot\ \mathbf{D}|g\rangle|^2\rho(\omega)$, where E is the fluctuating vacuum field at the location of the emitter, D is the dipole operator associated with the optical transition at hand, and ρ is the density of photon states. Hence, the strength of emission into different WGMs and consequently β_i are proportional to the projection of each mode's field intensity, $|E_i|^2$, at the sphere surface onto the dipolar axis. This enhancement is reduced if the line width of the dipole is broadened to Γ_b, greater than the cavity line width, Γ_{cav}, as is the case for $\Gamma_{cav} = 6 \times 10^{-5}$ nm and $\Gamma_b = 20$ nm in this experiment. The ratio, β, of the emission into the cavity mode to the total emitted power is thus given by $\beta = \beta_0(\Gamma_{cav}/\Gamma_b)$ [YU85] whereby β_0 represents the fraction for a narrow-band emitter. Note that because $\beta_0 \propto Q$, in this case β becomes independent of Q. An estimate for β_0 can be taken from the previous section:

it was found that $\beta_0 = 0.5$ at a distance of 50 nm from the sphere's surface, leading to $\beta_i = 1.5 \times 10^{-6}$. For other WGMs, higher n and $l - m$ result in an increase of the mode volume and lower $|E_i|^2$ values. By computing the mode functions of the various WGMs, one can determine $|E_i|^2$ on the sphere surface normalized to its value for the fundamental mode. Furthermore, by calculating the diffraction limited Q for various n, the dependence of the quotient in equation 5.21 on this parameter can be determined. Combining these results it is found that for each l the contribution to $\eta = \sum_i \eta_i$ of modes with $n > 10$ drops by an order of magnitude. It is also found that the first 40 modes with different $l - m$ values account for half the contribution of all modes. Considering that the fluorescence spectrum of a bead spans about 20 FSRs (FSR=2.3 nm for $2R = 35$ μm) and taking into account both TE and TM modes, one can conclude that η is about $10 \times 40 \times 20 \times 2 = 2 \times 10^4$ times larger than that of a single fundamental mode. Putting all of the above mentioned information together, one arrives at the conclusion that $\eta = (1.5 \times 10^{-6}) \times 10^{-4} \times (2 \times 10^4) = 10^{-6}$ for a single molecule acceptor, which is more than 6 orders of magnitude larger than the free-space rate for absorbing a photon emitted at a distance of about 35 μm.

This experiment was the first experimental realization of the possibility of coupling different nanoparticles via shared high-Q modes of a microresonator.

Chapter 6

Scattering in Microsphere Resonators: an Analogy to Strong Coupling and Purcell Effect

In this chapter an analogy between scattering in a microsphere resonator and Cavity QED is presented. A SNOM tip is used as a controllable scatterer, which can be inserted in the evanescent field of the high-Q modes at will with nanometer precision, and induce a coupling between two counterpropagating modes. This system is analogous to an atom interacting with a single mode of an optical cavity. The analogy in terms of Cavity QED effects, also gives an explanation for the surprisingly large mode splitting observed before.

6.1 Role of a Scatterer in an Evanescent Field

In chapter 5.1 the emission properties of a radiating dipole close to an interface have been explored with the intent of determining which fraction of the emission of a dipole couples to the WGMs. It was indicated that an ensemble of dipoles which emit inhomogeneously broadened light, will not experience an overall resonant amplification. A single narrow-band radiating dipole can, however, be simulated by a near field probe: when a probe tip with sub-wavelength curvature radius at the apex is introduced into the evanescent field of the WGMs, a dipole is induced. This induced dipole will spectrally match the cavity resonance as well as its polarization. Introducing the tip into the evanescent field of the mode has two main effects: on the one hand it constitutes an additional loss channel, so that the Q-factor of the microsphere is reduced; on the other hand the tip will introduce a coupling between two counterpropagating degenerate whispering-gallery modes. The result is a splitting of the resonance to a doublet, where the frequency spacing between the two peaks is given by twice the coupling rate of the modes. This is analogous to an atom strongly interacting with a single mode of a cavity in the Jaynes-Cumming model. This analogy is sketched in Fig. 6.1.

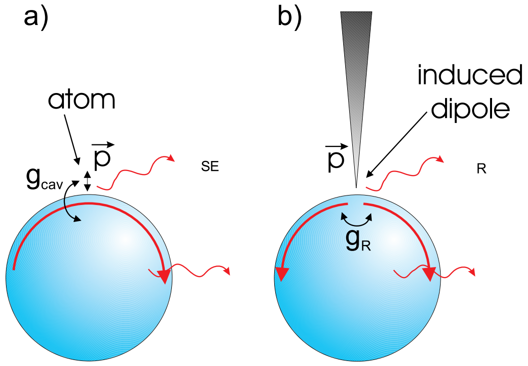

Figure 6.1: Schematic depiction of the two analogous systems with microsphere resonators as optical cavity. In a) a single atomic dipole couples to one WGM of the microsphere resonator. In b) two counterpropagating WGMs are coupled through Rayleigh scattering induced by a single dipole

In 6.1 a) an atom couples coherently to a single cavity mode with a coupling constant g_{cav} as well as to a continuum of propagating modes with spontaneous emission rate Γ_{SE}. κ is the damping rate of the cavity mode. In 6.1 b) a microsphere resonator coupled to a dielectric scatterer is shown. The arrows indicate the two counterpropagating modes. Light in one of the modes, for instance the clockwise (cw) propagating one, induces a dipole in the SNOM tip, which acts as a Rayleigh scatterer. The dipole radiation can couple into the counterclockwise (ccw) propagating mode or into a continuum of propagating modes. The scatterer will thus couple the cw and ccw propagating modes with rate g_R, and also couple these two modes to the continuum with a coupling rate Γ_R. In this sense, a classical optical system shows features typically associated to quantum physics. This kind of analogy is a topic with a long history that has been investigated in many different contests [Kru87, PF89, SW91]. A macroscopic system offers the important advantage that every parameter is accessible and can be experimentally controlled. This kind of analogy-thinking may also lead to new experimental possibilities for investigating current issues in quantum optics and Cavity QED.

First observations of intramodal coupling in microspheres date back to

1995 [WSH+95], where its relation to scattering was pointed out. There it was demonstrated that the modal coupling is due to backscattering of light from impurities in the glass matrix of the resonator. In [GPI00] a more detailed analysis of this scattering was performed. This kind of coupling was also observed in toroidal WGM resonators [KSV02], where the relation to a coupler device for the whispering-gallery modes was investigated. In both cases, the splitting was induced by a collective scattering of a great number of scatterers, distributed inside the whole modal volume. A strong intramodal coupling can however also be obtained by use of a single scatterer, e.g. composed of a great number of atoms all localized in a small portion of the mode volume as addressed in [KLNH06]. Also, in [SP06], an analysis of the intramodal coupling in a microdisk cavity caused by a two-level system has been done.

Coupled Modes Model

The system can be described in a coupled mode model [GPI00], where one can write down the following set of equations for the mode amplitudes a_k:

$$\frac{da_k}{dt} + i\omega_k a_k = \sum_{j\neq k} i g_{R,kj} a_j. \tag{6.1}$$

In this equation ω_k is a frequency, and $g_{R,kj}$ is the coupling rate between the modes a_k and a_j. The electric field of the modes is given by:

$$\vec{E}_j(r,\theta,\phi,t) = e^{-i\omega_0 t}\sum_j \tilde{a}_j(t)\vec{e}_j(r.\theta,\phi). \tag{6.2}$$

The coupling rate $g_{R,kj}$ can be then written as [GPI00]:

$$g_{R,kj} = \frac{\omega_0}{2N^2}\frac{\int \vec{e}_j \delta\epsilon \vec{e}_k^* dV}{\int |\vec{e}_j|^2 dV}. \tag{6.3}$$

Here, $\delta\epsilon$ describes variations in the dielectric constant ϵ of the sphere and is responsible for the intramodal coupling [GPI00]. This system can be solved in two different regimes. On the one hand, there is the so called strong coupling regime, where the intramodal coupling rate dominates over the losses:

$$g_{R,kj} \gg \max(\Gamma_R, \kappa). \tag{6.4}$$

Coupling lifts the degeneracy of the two counterpropagating modes: the resonance will be a doublet with a mode splitting $\Delta\omega$ of twice the coupling constant $\Delta\omega = 2g_R$. On the other hand, there is the weak coupling regime defined by:

$$g_{R,kj} \ll (\Gamma_R, \kappa). \tag{6.5}$$

The equation system is first solved in the weak coupling regime [MI98]. Since the mode amplitude can be written as:

$$\widetilde{a}_j = e^{i\omega_j t} a_j \tag{6.6}$$

the equation 6.1 will be transformed to:

$$\frac{d\widetilde{a}_j}{dt} = i \sum_k e^{i(\omega_k - \omega_j)t} \widetilde{a}_k g_{kj} \tag{6.7}$$

and can be integrated in time to obtain an integral-equation for the mode amplitude $\widetilde{a}_k$:

$$\widetilde{a}_j = \int_0^t i e^{i(\omega_k - \omega_j)t'} \widetilde{a}_k g_{kj} dt'. \tag{6.8}$$

This can be inserted into equation 6.1 to calculate the transition rate to all modes of the reservoir:

$$\frac{d\widetilde{a}_k}{dt} = -\sum_j g_{kj}^2 \int_0^t i e^{i(\omega_k - \omega_j)(t-t')} \widetilde{a}_k(t') dt'. \tag{6.9}$$

The main point of the theory is that the sum in 6.9 can be replaced by an integral over all the modes of the electromagnetic field in the free space:

$$\sum_j \rightarrow \frac{VN^3}{(2\pi c)^3} \int d\Omega\Omega^2 \int_0^\pi \sin\theta d\theta \int_0^{2\pi} d\phi \tag{6.10}$$

where N is the refractive index of the medium and the density of states $D(\omega)$ in the quantization volume V is given by:

$$D(\omega) = \frac{\omega^2 V}{\pi^2 (c/N)^3}. \tag{6.11}$$

The integral equation for $\widetilde{a}_k$ then becomes (evaluating the integration over the whole solid angle as 4π):

$$\frac{d\widetilde{a}_k}{dt} = -\frac{VN^3}{(2\pi c)^3} g_{kj}^2 4\pi \int d\omega_j \int dt' e^{-i(\omega_k - \omega_j)(t-t')} \omega_j^2 \widetilde{a}_k(t'). \tag{6.12}$$

Since the frequency ω_j varies little in the interval for which the integral over t' has appreciable value, another approximation can be made, i.e. that the amplitude of the mode $\tilde{a}_k(t)$ varies slowly in the time, so that in the interval $[0, t]$ it is almost constant and can be evaluated at $t = t'$ and factored outside the integrals. The remaining integral in 6.12 has the highly peaked value:

$$\lim_{t\to\infty} \int_0^t \int dt' e^{-i(\omega_k-\omega_j)(t-t')} = \pi\delta(\omega_j - \omega_k) - \mathcal{P}\left[\frac{i}{\omega_j - \omega_k}\right] \tag{6.13}$$

where $\delta(\omega_j - \omega_k)$ is a delta function and $\mathcal{P}\left[\frac{i}{\omega_j-\omega_k}\right]$ is the principal value of the integral (which represent a frequency shift). Then the equation 6.12 can be evaluated to find (neglecting the frequency shift):

$$\frac{d\tilde{a}_k}{dt} = \frac{V}{2\pi}\frac{N^3 g_{kj}^2 \omega_k^2}{c^3}\tilde{a}_k(t'). \tag{6.14}$$

This means that the mode is damped at a rate:

$$\Gamma_{R,free} = \frac{V}{2\pi}\frac{N^3\omega_k^2}{c^3} g_{kj}^2 \tag{6.15}$$

proportional to the coupling constant g_{kj}^2. This result is obtained in complete analogy to the spontaneous decay of a dipole $\vec{p}$ interacting with a continuum of vacuum modes $\vec{E}_i$, as described within the Weisskopf-Wigner theory [MI98]. For the spontaneous emission rate in the free space this delivers a rate:

$$\Gamma_R = \frac{V}{2\pi}\frac{N^3\omega_k^2}{c^3}|\vec{E}\cdot\vec{p}|^2 \tag{6.16}$$

in analogy to 6.15.

Resonant Enhancement of the Radiating Rate

Now, if a cavity is present, the density of states 6.11 is modified and has to be replaced with the density of states of the cavity:

$$D_{cav}(\omega) = \frac{2}{\pi(\omega/Q)}\frac{(\omega/Q)^2}{4(\omega-\omega_c)^2 + (\omega/Q)^2}. \tag{6.17}$$

The result is that the damping rate in presence of the cavity $\Gamma_{R_{cav}}$ is given by by:

$$\Gamma_{R_{cav}} = \frac{3}{4\pi^2}\frac{Q(\lambda/N)^3}{V}\Gamma_{R,free} = \mathcal{F}\Gamma_{R,free} \tag{6.18}$$

where the Purcell factor $\mathcal{F} = \frac{3}{4\pi^2}\frac{Q(\lambda/N)^3}{V}$ has been introduced. The Purcell effect was first introduced by Purcell [Pur46] in 1946, who pointed out that the spontaneous emission probability of magnetic moments can be strongly enhanced by the presence of a resonant circuit, due to the change in the density of states of the electromagnetic field surrounding the magnetic moment.

Solution of the Coupled Mode System: New Eigenmodes

In the case here presented it is possible to reduce the system 6.1 to only two equation. In fact, coupling between modes with different n or l due to scattering has never been observed in this work. Thus, only two counterpropagating modes identified by the same n and l and opposite m are considered, since these are the modes showing the strongest overlap. The equation system 6.1 can thus be written for the amplitudes a_+ and a_- in the following way [Hau84]:

$$\begin{aligned} \frac{da_+}{dt} &= -i\Delta\omega a_+ - \frac{1}{\tau}a_+ + iga_- + \kappa B_{in} \\ \frac{da_-}{dt} &= -i\Delta\omega a_- - \frac{1}{\tau}a_- + iga_+ \end{aligned} \tag{6.19}$$

where the indices of the intramodal coupling rate g have been dropped for simplicity. Here the phenomenological loss rate $1/\tau$ accounts for scattering in a continuum of lossy modes (as described in the weak coupling regime). Additionally, a pump field B_{in} has been introduced. κ is the coupling rate between the pump field and the mode a_+, which is set to be the mode excited by the coupler and the incoming field. The system can be solved in the stationary case. The following solutions are found:

$$\begin{aligned} a_+ &= \kappa\frac{\frac{1}{\tau} + i\Delta\omega}{\frac{1}{\tau^2} + g^2 - \Delta\omega^2 + 2i\frac{\Delta\omega}{\tau}}B_{in} \\ a_- &= \kappa\frac{ig}{\frac{1}{\tau^2} + g^2 - \Delta\omega^2 + 2i\frac{\Delta\omega}{\tau}}B_{in}. \end{aligned} \tag{6.20}$$

The system presents now two new eigenmodes, which are given by the symmetric and anti-symmetric linear combination of the modes a_+ and a_-, and can be written as:

$$\begin{aligned} s_+ &= \frac{1}{\sqrt{2}}(a_+ + a_-) \\ s_- &= \frac{1}{\sqrt{2}}(a_+ - a_-). \end{aligned} \tag{6.21}$$

At this point the physics of the system is known. In the following section an experiment is described where a Rayleigh scatterer is inserted into the evanescent field of the WGMs at will, so that the coupling between cw and ccw propagating modes can be changed in a controllable manner.

6.2 Observation of Mode Splitting due to Intramodal Coupling

The experimental setup to study controlled coupling of two counterpropagating modes is shown in figure 6.2. Light from a tunable diode laser (emitting at $\lambda_p = 670$ nm, linewidth $\Delta\lambda < 500$ KHz, tuning range ≈ 60 GHz) can be coupled to the whispering-gallery modes of a microsphere resonator with a radius of 15 μm via a prism. Using the procedure described in 3.5 the system can be optimized to efficiently couple light into the fundamental mode.

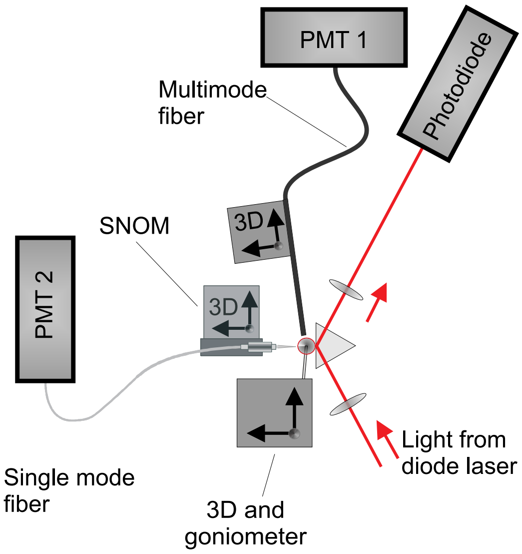

Figure 6.2: Schematic depiction of the experimental setup to study intramodal coupling in a microsphere resonator.

Light scattered from the whispering-gallery modes is detected via a multimode fiber held close to the microsphere. A near-field probe is used as a controllable scatterer: the tip can be modeled as a small sphere with a radius of around 50 nm (which is the radius of the tip at the apex). Exploiting active stabilization via a shear-force control, the tip can be held at a constant distance of a few nanometers from the sphere's surface. The tip is then scanned across the fundamental mode along the polar direction, while the resonance is constantly monitored via the multimode fiber. The result is shown in figure 6.3 as a spatio-spectral map. Figure 6.3 a) shows the resonance for different

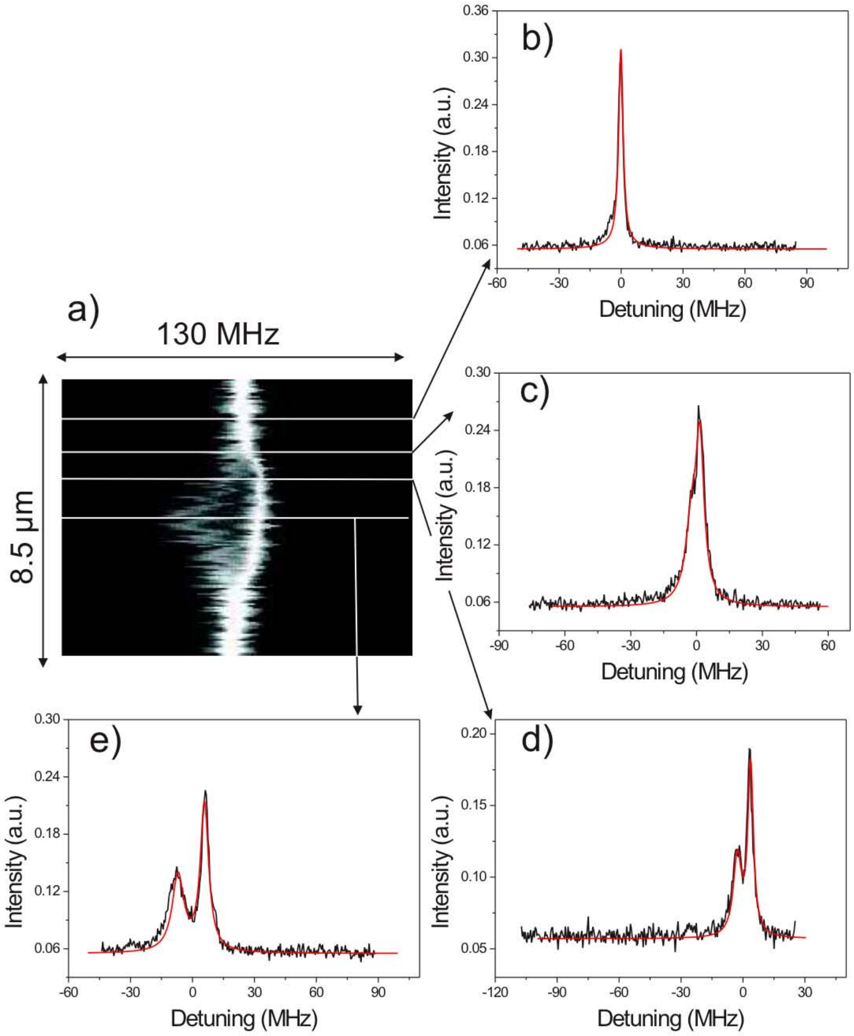

Figure 6.3: Spatio-spectral mode map shpwing the transition from the weak to the strong coupling regimes when scanning a SNOM tip through a fundamental mode along the polar direction. a): Mapping of spectra versus the tip's position. b) to e): Spectra with the tip away from the mode, in two intermediate position, and in the field maximum, respectively.

positions of the tip. The horizontal axis indicates the frequency scan, while the vertical axis is the position of the tip relative to the sphere's equator, which is in the center of the picture. The intensity of the signal detected on PMT1 is shown in gray-scale. As long as the tip is outside the mode one can see a single peak resonance, as shown in the cross section displayed in figure

6.3 b). This means that the coherent coupling between the cw and ccw mode is very weak. But, as the tip enters the mode, the resonance broadens due to enhanced incoherent scattering into the continuum (figure 6.3 c)). This corresponds to the weak coupling regime. Moving the tip further towards the mode intensity maximum gradually increases the coupling constant g_R between the cw and the ccw propagating modes, until the coherent coupling rate exceeds the inhomogeneous loss rate: at this point a splitting is observed (figure 6.3 d) and e)). These two peaks correspond to two new eigenmodes s_+ and s_-: they are symmetric and anti-symmetric linear combinations of waves propagating in opposite directions and represent standing waves [SvDEW90]. An asymmetry between the two peaks can be observed. This derives from the fact that the scatterer introduces not only an intramodal coupling, but also an additional loss channel. Thus, the coupling constant can be written as:

$$g = g_\kappa + iR_{tip} \tag{6.22}$$

where g_κ takes into account the scattering into the counterpropagating mode, while R_{tip} is the rate of the scattering into the continuum of lossy modes induced by the tip. The function that describes the new eigenmodes can be derived from equations 6.20 and 6.21. After some simplification one obtains for the intensity:

$$\begin{gathered} I(\omega) = |s_+(\omega) + s_-(\omega)|^2 = \\ \frac{2}{\tau_c} \times |\frac{1}{g_\kappa - iR_{tip} - \frac{i}{\tau} - 2\omega}|^2 + |\frac{1}{g_{kappa} - iR_{tip} + \frac{i}{\tau} + 2\omega}|^2. \end{gathered} \tag{6.23}$$

From the last equation one can see that there is an asymmetry between s_+ and s_-, due to the fact that the tip induced losses are added to the internal losses for s_+, while they are subtracted from the internal losses for s_-. This derives from the fact that the tip will pin the phase between the two eigenmodes to minimize the total energy. The curves of figure 6.3 b) to e) were fitted with equation 6.23. The fitting parameters for the scattering (R_{tip})and intramodal coupling (g_κ) rates are reported in the following table, where the first column refers to figure 6.3:

Data	g_κ (Hz)	R_{tip} (Hz)	$1/\tau$ (Hz)
(c)	4.0×10^6	6.5×10^5	5.4×10^6
(d)	6.4×10^6	7.6×10^5	5.6×10^6
(e)	13.5×10^6	9.6×10^5	5.9×10^6

The slight increase of R_0 is due to the fact that during the measurement, the sphere has drifted slightly towards the prism: as a consequence the total Q-factor decreases. One can see that the intramodal coupling rate increases by a factor of 3.4, thus overcoming thus the total loss rate given by the sum of R_{tip} and R_0. When the tip is in the maximum of the mode the coupling rate is actually about twice the scattering rate.

Numerical considerations

The observation of splitting induced by a single local scatterer is remarkable. It requires most of the photons scattered out of the cw mode to be re-injected into the ccw mode and vice versa. This is surprising as the tightly confined fundamental WGM has a very narrow acceptance range for scattered photons, as shown in section 5.1, in particular compared to propagating free space modes. The expected fraction of photons which are re-injected into the ccw mode can be estimated, following a geometrical consideration as in section 5.1, by calculating the modified emission pattern for an induced dipole on the sphere's surface (assuming a planar interface as in [LK77]) and then calculating its superposition with the WGM's mode profile. It is found that only a fraction of $\eta = 1.5 \times 10^{-5}$ of the complete radiated power should couple to the mode. The maximum total scattering rate of the SNOM tip can be determined experimentally by the tip-induced reduction of the Q-factor when the tip is in the maximum of the mode profile. The Q-factor is proportional to the life-time of a photon in the cavity $Q_{total} = \omega\tau_{total}$, and is related to the scattering rate by:

$$Q = \frac{\omega}{\Gamma_{tot}} = \frac{\omega}{\Gamma_{sphere} + \Gamma_{tip}} \tag{6.24}$$

where Γ_{sphere} is the loss rate of the sphere without the tip, and Γ_{tip} is the additional scattering rate of the tip.

From the change of the Q-factor induced by the tip, one can calculate Γ_{tip}. With reference to the measurement shown in figure 6.4, one finds Γ_{tip} to be about 60 MHz. This multiplied by η yields a maximum scattering rate between the cw and ccw mode on the order of 1 kHz. This would be far too small to reach the condition for strong coupling (equation 6.4) which requires that the photon exchange between the cw and ccw mode has to be the dominant process. As a result, mode splitting by a single scatterer should not occur. However, a resonant enhancement by the Purcell factor F (equation 6.18) increases the scattering between cw and ccw mode in our case by a factor of $F = 4 \times 10^3$. The large enhancement of almost four orders of magnitude resulting from the small mode volume of $130\,\mu m^3$ (sphere diameter $30\,\mu m$) and the high Q factor of 5×10^7 of the microsphere resonator compensates the small purely geometrical coupling efficiency η. It establishes the coupling between the cw and ccw mode as a process on the same order as photon loss, which in the experiment is observed as the onset of mode splitting. Including the Purcell enhancement factor the value for the modal splitting is 4 MHz. This is still a factor of 5 smaller than the observed splitting induced by the tip, which is 20 MHz. The deviation can easily be corrected by considering that the definition of the acceptance angles given in section 5.1 is very stringent. The geometrical consideration presented there is an estimation. Compared to the exact calculation as shown in section 5.2 it underestimates the coupling efficiency. An agreement within a factor of 5 is therefore satisfactory.

To gain a better understanding in the problem, another experiment is performed, where both the splitting and the Q-factor (derived from the induced broadening of the resonance lines) are simultaneously recorded while the SNOM tip is scanned across the fundamental WGM in polar direction. As can be seen in figure 6.4 an increasing splitting (figure 6.4 a) is accompanied by a decreasing Q-factor (figure 6.4 b). In this measurement an intrinsic splitting of $\Delta\omega/2\pi = 11.5\ MHz$ is present. Solid red lines are results of fitting the experimental data with Hermite polynomials of order l, which reflect the spatial mode profile of the fundamental WGM. The mode number l is related to the radius of the sphere (in this experiment $r = 30\,\mu m$) and the wavelength λ of the mode by $l = 2\pi r N/\lambda$ with the refractive index $N = 1.46$ of the sphere. The coupled mode analysis in analogy to cavity QED predicts that the splitting is proportional to the coupling constant g_R and that the Q-factor is inversely proportional to the loss rate Γ_R and thus to g_R^2 (equation 6.15). Thus, one expects $\Delta\omega = 2g_R \propto Q^{-1/2}$.

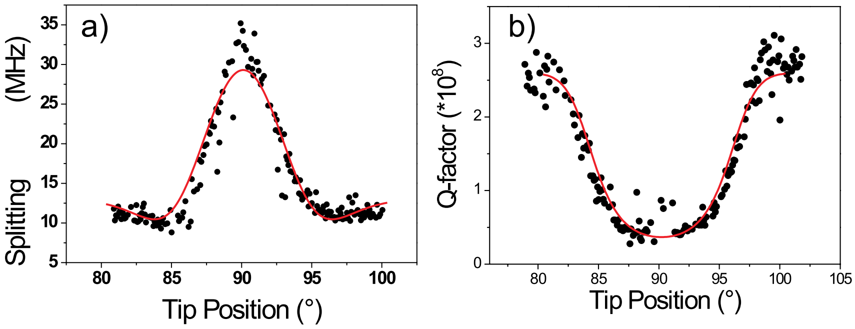

Figure 6.4: Induced splitting a) and Q-factor b) of the fundamental WGM when a SNOM tip is scanned along the polar direction. 90° correspond to the sphere's equator. Red lines are theoretical fits to Hermite polynomials.

In order to further investigate this relation g_R can be changed by controllably pulling back the SNOM tip (initially in the field maximum of the WGM corresponding to 90° in figure 6.4) from the sphere's surface. Figure 6.5 a) shows a logarithmic plot of the measured splitting ($\Delta\omega = 2g_R$) versus the measured Q-factor. Figure 6.5 b) shows the Q-factor as a function of the tip-to-surface distance. The linear fit has the exponent of -0.53 which agrees very well with the expected value of -0.50. This again proves that analogous effects of the weak and strong coupling regimes in CQED can be controllably studied in these experiments.

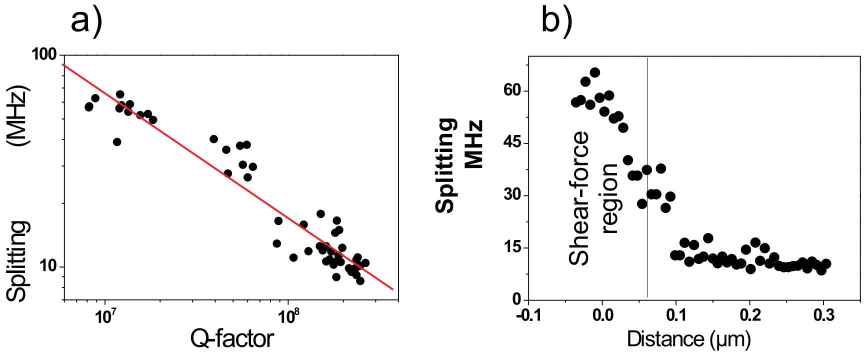

Figure 6.5: a) Splitting of the fundamental WGM as a function of the Q-factor when a tip is inserted in the maximum of the fundamental mode and then pulled back. b) Splitting as a function of the distance of the tip to the sphere's surface.

In fact, coupling of two high-Q modes in a microsphere resonator by a local scatterer can be described in analogy to cavity QED systems. The experimentally observed Purcell enhancement of local Rayleigh scattering also explains previous observations of surprisingly large mode coupling [WSH+95, BKB+01, KSV02].

6.3 Scattering-Interference

In some situations the following phenomenon can be observed: as the tip enters the mode while being scanned along the polar direction, the splitting is first reduced, and then increased until it reaches a maximum when the tip is in the intensity maximum of the mode.

Figure 6.6 shows this for a sphere with a diameter of 70 μm, when the tip is scanned through the fundamental mode. This phenomenon can be explained by assuming coupling by two scatterers in the following way: one scatterer is

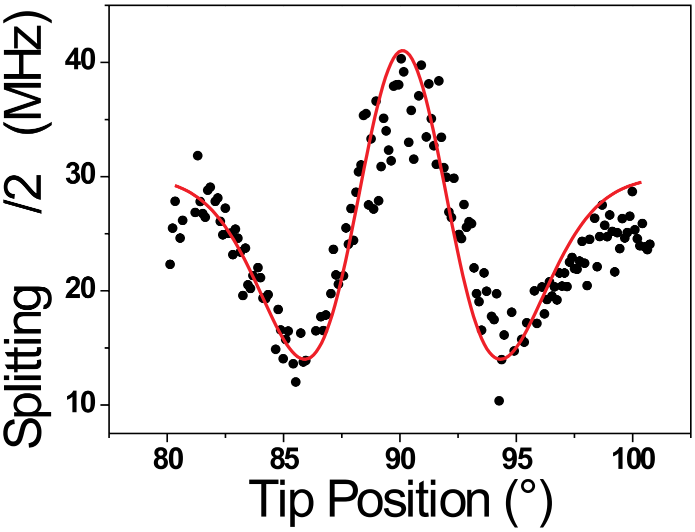

Figure 6.6: Induced splitting of a fundamental WGM when a tip is scanned through the fundamental WGM along the polar direction. 90° defines the optical equator of the sphere. As the tip enters the mode the intramodal coupling is first quenched, then enhanced to reach a maximum in a position corresponding to the intensity maximum of the mode.

present even in absence of the SNOM tip. It can be regarded as an effective scatterer summarizing the effect of the local dielectric inhomogeneities, and it accounts for the observed intrinsic mode splitting. The other scatterer is the SNOM tip. As previously outlined, the new coupled eigenmodes (sine and cosine standing waves) are spatially pinned with respect to a local scatterer to minimize the energy of the system. The scatterer is in the maximum of one mode and thus in the minimum of the other. If an additional local scatterer is now introduced, it contributes coherently to the scattering and an interference phenomenon can be observed There is thus a well defined phase relationship between the tip and the equivalent internal scatterer, and this phase can be controlled by simply moving the tip along the sphere's equator. For this reason one has to introduce a coherent sum of the two coupling rates γ_i due to the internal scatterers plus γ_{tip} due to the tip:

$$g_R = \gamma_i + e^{\imath\phi}\gamma_{tip}(\theta), \tag{6.25}$$

The red curve in Fig.6.6 is the theoretical curve according to the previously written coupling rate. The phase ϕ depends on the position of the tip. To further investigate this interference effect the near-field probe is scanned along the sphere's equator, being constantly in the maximum of the mode in the polar direction. At the same time, the resonance is detected through the multimode fiber. As one can see in Fig 6.7 the coupling rate (and accordingly the splitting) oscillates with a period of 467 nm, which is a clear signature of the interference effect.

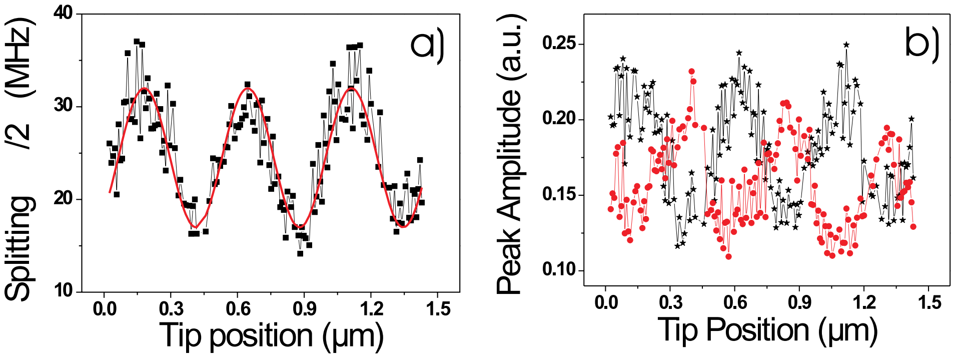

Figure 6.7: a): Scattering interference between a near-field probe and the equivalent internal scatterer. The near-field probe is scanned along the equator, being always in the maximum of the fundamental WGM. Depending on the position of the tip the intramodal coupling rate is either enhanced or reduced. b) Peak amplitudes of the two new eigenmodes formed by symmetrical superposition of the cw and ccw propagating waves. The modes are shifted by $\pi/2$, so that when the tip interacts at maximum with one mode it leaves the other unperturbed.

The oscillation period fits the intensity distribution of the WGM in the azimuthal direction well, as the distribution is proportional to $exp(-\imath m\phi)$, where m is the azimuthal quantum number. This has a period of $\frac{2\pi}{m} = \frac{\lambda}{n} =$ 465 nm. In addition to the oscillation in the coupling rate one can also see how the amplitudes of the two new eigenmodes of the sphere oscillate. This derives from the fact that the two new eigenmodes are shifted by $\pi/2$ [SP06]: when the tip is in the maximum of one mode, it is in the minimum of the other. So the tip will scatter photons from one mode, and reduce its Q-factor, while leaving the other mode unperturbed.

To prove this, the tip is scanned along the equator. For different positions of the tip the laser is scanned and the resonance is recorded. In figure 6.8 b) to d) single frequency scan across the resonance are shown for different

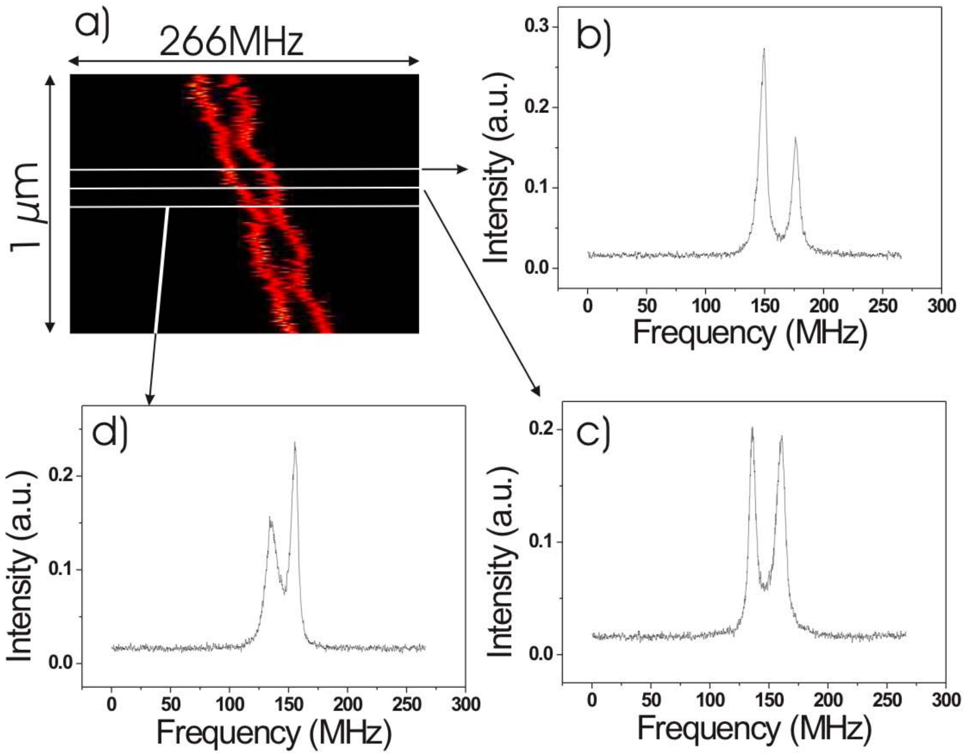

Figure 6.8: Asymmetry of the peak amplitudes: a) A near field probe is scanned along the optical equator while the resonance is detected via a multimode fiber hold close to the sphere. b) to d): spectra recorded for different positions of the tip.

positions of the tip. This means that it is possible to controllably quench or enhance the coupling between the two counterpropagating waves at will. To show this, the tip is scanned in the polar direction through the fundamental mode. The tip is then moved half an interference period to the side and the polar scan is repeated. In figure 6.9 (a) the tip is positioned so that when it enters the mode the interaction with the other scatterer is only a destructive interference, and intramodal coupling is quenched. In (b) the tip is shifted about 230 nm to the side, so that now when it enters the mode the interaction will result in a constructive interference.

In summary, a novel analogy between a classical scattering system and the basic system of Cavity QED has been introduced here. The transition between the regimes of weak and strong coupling was observed, as well as a

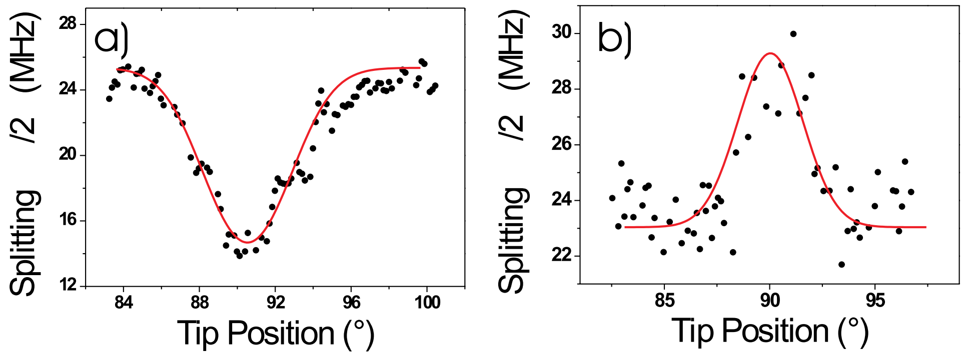

Figure 6.9: Controlled quenching or enhancing of the intramodal coupling with a near-field probe. Both in a) and b) the tip is scanned through the fundamental whispering gallery mode along the polar direction, but in two different azimuthal positions.

resonant enhancement of scattering in microsphere resonators. This might be of crucial importance in devices based on microresonators.

Chapter 7

Conclusions and Outlook

In this work different optical properties and applications of microsphere resonators were studied and demonstrated.

First, a microsphere resonator was used to observe ultra-low threshold Raman lasing, and the effect of a scatterer on the lasing properties has been investigated.

Second, the dynamics of a single dipole coupling to the whispering-gallery modes of a microsphere resonator has also been depicted. It was pointed out that if the emitter emission is much broader than the cavity linewidth, then no cavity modification of the lifetime or no Cavity QED effects will be observable. However, one can still use the cavity to observe resonant enhancement of photon exchange between two emitters. The controlled coupling of two nanoparticles via shared high-Q modes of a microsphere resonator has been then demonstrated as an application of microsphere resonators.

Last, a novel analogy between a quantum system composed by an atom interacting with a single mode of a cavity and a classical system composed by two coupled modes of a microsphere resonator was introduced. A near-field probe was used as a tool to controllably induce a coupling between two counterpropagating whispering-gallery modes. The transition from the weak to strong coupling regime was studied. An interesting interference effect between two scatterers interacting via the whispering-gallery modes was observed and theoretically modeled.

This work opens the way to various new experiments, where one would work with single quantum emitters. However, in order to be able to observe Cavity QED effects, a cryogenic setup is needed. Before doing this, it is important to test at room temperature the feasibility of such an experiment. Next, first experimental results going in this direction are reported. As an outlook, a further system to be implemented in a cryogenic setup is proposed, and some possible experiments are suggested.

7.1 Coupling of a Single Molecule to the Whispering-Gallery Modes

In section 5.3 results on the coupling of a single radiating dipole to the whispering-gallery modes were reported. In this section, the possibility of reducing the number of emitters to only one is exploited. This is the ultimate limit of the experiment performed in section 5.3, where the number of molecules in the nanoparticle was as large as 10^5.

Single terrylene molecules are chosen as the emitter. These molecules can be spin-coated on a glass coverslip, and they are embedded in a crystalline matrix of para-terphenyl (p-terphenyl). This prevents the molecules from photo-bleaching and from blinking [PZH$^+$04], processes that are common when dealing with single emitters at room temperature such as single molecules or nanocrystal quantum dots. The procedure for the production of this kind of probe has been developed at the ETH in Zürich and is described in [PZH$^+$04]. A second advantage of the spin-coating recipe is that within the crystalline matrix the molecules have an orientation that is perpendicular to the coverslip. This is optimal for coupling to the whispering-gallery modes, as was shown in section 5.1.

The experimental setup to investigate single molecule coupling is similar to the one used in section 5.3, but was slightly modified. Since the molecules are spin-coated on a coverslip, the dimension of a prims coupler are too big to allow positioning of a sphere between the prism and the coverslip. To solve this problem a polished fiber is used as coupler instead of a prism. The setup is sketched in figure 7.1. The terrylene molecules are pumped by an argon laser (emission at $\lambda = 514$ nm) via a high NA immersion oil microscope objective (NA=1.4). By looking at the sample via the same microscope objective a single molecule can be identified and selectively pumped. The

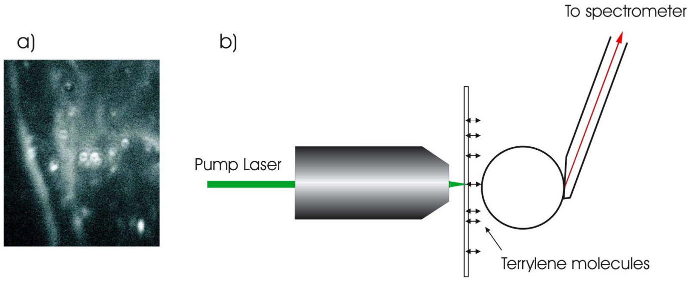

Figure 7.1: a) Wide field image of a coverslip covered by spin coating with terrylene molecules embedded in a p-terphenyl crystalline matrix. b) Setup to couple single molecules to the high-Q modes of a microsphere resonator

fluorescence of the molecule couples to the whispering gallery modes and is collected by a multimode fiber. The fiber output is collimated, the pump light is filtered out with a Raman long-pass filter (cut-off wavelength 538 nm) and the fluorescence is finally analyzed with a spectrometer.

First, a control is made to test the performance of the polished fiber. A sphere is first coupled to a prism while a diode laser is scanned over a wide frequency range ($\approx$ 60 GHz). A multimode fiber is held close to the sphere to detect photon scattered out of the modes, as described in chapter 3.5. Then the sphere is taken away from the prism, and the same laser is coupled into the polished fiber, which approaches the sphere. The laser frequency is scanned over the same frequency range, and again a spectrum is recorded via the multimode fiber. The results for the two situations are shown in figure 7.2. The recorded spectra are basically identical, apart from a slightly higher noise level for the fiber coupler. This means that the polished fiber will in- or outcouple light with the same selectivity as the prism.

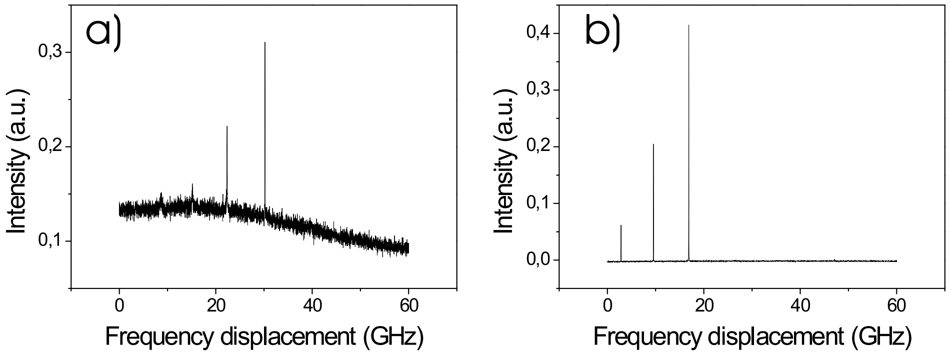

Figure 7.2: Spectrum of whispering-gallery modes detected through a multimode fiber held close to the microsphere. In a) the modes are excited via a polished fiber coupler, in b) via a prism coupler. The two spectra show the same modes, only the noise is higher in the case of the polished fiber.

The following experiment is then performed: a microsphere with a diameter of 40 μm is brought in proximity with a coverslip prepared with terrylene molecules. On the other side of the coverslip the confocal microscope is used to identify and excite a single molecule, as shown in figure 7.1. The fluorescence of the molecule can be detected either via the microscope objective or via the polished fiber, which is brought in proximity with the microsphere from the side opposite to the microscope. The recorded spectra are shown in figure 7.3.

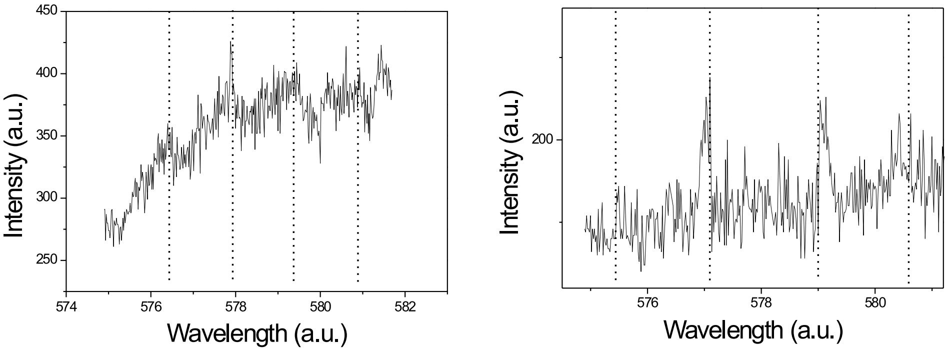

Figure 7.3: a): spectrum of a single terrylene molecule coupled to a microsphere resonator detected via the microscope. b): spectrum of the same molecule detected via the polished fiber. Dotted lines are inserted as a visual aid.

fiber can be interpreted similarly as in section 5.3 for a bead containing a large number of molecules. The distance between the peaks is 2.01 nm, as one would expect for a sphere with a 40 μm diameter for which the FSR is 2.03 nm. These are first results for controlled coupling of a single quantum emitter to a microsphere resonator.

7.2 Further Experiments

A Low Temperature Setup

The observation of Cavity QED effects in a system composed by a dipole and a single mode of a cavity requires precise experimental parameters: long photon storage time, a narrow-band emitter, a strong coupling constant and the ability to control the coupling. While a long storage time can be already achieved at room temperature, there are no emitters which are big enough to allow controlled positioning with respect to the cavity, and at the same time have an emission bandwidth of only a few MHz. For this reason, a low-temperature setup is required if one wants to perform Cavity QED experiments.

Toroidal Resonators

In a cavity, a high Q-factor and a small mode volume produce a strong field enhancement for the modes of the cavity. This results in a stronger coupling constant. In the last few years a new kind of whispering-gallery modes resonator has been produced, which exploits a toroidal form instead of a spherical one [AKSV03]. These resonators offer two main advantages with respect to spherical resonators: they have smaller mode volumes and can be fabricated in a reproducible way on a chip, while offering Q-factors as high as those of silica microsphere. A prerequisite for a reliable experiment setup is an efficient coupling of light to the cavity modes. Different from microspheres, when using toroidal cavities a tapered fiber represent a better choice. It is smaller and more versatile, since it does not define a fixed geometry as a prism coupler does. Besides, it offers the advantage that the light outcoupled from the cavity propagates in a fiber. These couplers have already shown coupling efficiency up to 95 % [CPV00]. The coupled system toroid-tapered fiber is also easier to build in a cryostat, because of its smaller dimensions and bigger versatility. The cavity together with the fiber coupler can be mounted on a low-temperature three-axis stage and a long distance high NA microscope objective can be used to selectively pump emitters on the cavity. Pre-alignemnt can be done at room temperature.

Single Emitters

In the last few years there has been a growing interest around the use of solid state quantum emitters in Cavity QED. Semiconductor quantum dots features nearly lifetime limited spectral width, and can be grown directly into cavities such as micropillars formed by Brag reflectors, or in microdisks [PVZ+02]. In these cases, strong coupling was also observed [RSL+04]. The main problem that remains, however, is the controlled positioning of the dots inside the cavity [GKHW01]. An alternative in order to realize robust systems is offered by quantum emitters embedded in micro- or nanoparticles: examples are nanocrystal quantum dots, terrylene molecules in p-terphenyl, or defects in diamond nanoparticles such as nitrogen vacancies (NV). The advantage in this case is that these emitters can show a stable behavior even at room temperature, where nanomanipulation techniques, e.g. for the positioning on a cavity, are easier to apply. NV defect centers are the most interesting possibility, since they are stable emitters at room temperature, and have a lifetime limited linewidth at low temperature (1.8 K) [BBG+01]. Additionally, tuning of these emitters by DC Stark effect is possible: this is a prerequisite for matching the radiating transition to the cavity modes [TGR+06].

From Weak to Strong Coupling and Single Emitter Lasing

The controlled coupling of an NV center to a toroidal microcavity will provide the possibility for studying the different regimes of *weak* and *strong* coupling, as they were described in section 6. In the weak coupling regime, changes in the lifetime of the excited level as described by Purcell are expected. Considering a lifetime of the first excited level of NV defect centers in diamond nanocrystals of 25 ns, for a toroid with a main radius of 50 μm and a Q-factor of 10^7 lifetime changes up to 10% can be expected. Reducing the dimensions of the cavity will increase the coupling constant, since a small mode volume implies a stronger electric field per photon inside the mode. This allow to enter the strong coupling regime, where the interaction between the emitter and the cavity becomes coherent, and a constant energy exchange between the cavity mode and the emitter can be observed. This phenomenon is known as Rabi oscillations, and can be observed as anticrossing of the cavity resonance and the emitter resonant transition when the two are tuned to overlap. The high collection efficiency of the tapered fiber will also allow photon statistics measurements. It is interesting to note at this point that when the conditions for strong coupling are satisfied, the lasing conditions are also fulfilled for this system, so that a single quantum emitter laser can be realized.

Controlled Coupling of two Quantum Emitters via Shared Modes

Finally, a low temperature system also makes cavity QED experiments with two quantum emitters possible. Here, pre-selection of the emitters at room temperature, and positioning and tunability of the quantum emitters will permit a controlled interaction between the two emitters via shared modes of the cavity. First, one will need to perform experiments similar to the ones described above for the two individual emitters. Then, a first proof of the coupling should be done by selectively pumping one of the two emitters and confocally detecting at the position of the second emitter. Finally, performing photon statistics on the signal outcoupled via the tapered fiber it will be possible to observe weak-coupling regime, while strong coupling will be identified by a doubled mode splitting as in the case of a single emitter. This system also offers a potential scalability: on the one hand, one can increase the number of emitters interacting with the cavity; on the other hand the tapered fiber can also be exploited to let different cavities interact with each other.

Bibliography

[ADW$^+$06] Aoki, Takao; Dayan, Barak; Wilcut, E.; Bowen, W. P.; Parkins, A. S.; Kippenberg, T. J.; Vahala, K. J.; Kimble, H. J.: Observation of strong coupling between one atom and a monolithic microresonator. In: *Nature*, volume 443:pp. 33–35, 2006.

[Agr01] Agrawal, G. P.: *Nonlinear Fiber Optics.* Academic Press Inc., 2001.

[AKSV03] Armani, D. K.; Kippenberg, T. J.; Spillane, S. M.; Vahala, K. J.: Ultra-high-q toroid microcavity on a chip. In: *Nature*, volume 421:pp. 925–929, 2003.

[AS72] Abramowitz, M.; Stegun, I.A.: *Handbook of mathematical functions.* Dover Publications Inc., 1972.

[BAS88] Barton, J.P.; Alexander, D.R.; S.A.Schaub: Internal and near surface electromagnetic fields for a spherical particle irradiated by a focused laser beam. In: *J. Appl. Phys*, volume 64(4):pp. 1632–1639, 1988.

[BBG$^+$01] Beveratos, Alexios; Brouri, Rosa; Gacoin, Thierry; Poizat, Jean-Philippe; ; Grangier, Philippe: Nonclassical radiation from diamond nanocrystals. In: *Phys. Rev. A*, volume 64:p. 61802, 2001.

[BC88] Barber, P. W.; Chang, R. K.: *Optical Effects Associated With Small Particles.* World Scientific, Singapore, 1988.

[Ber94] Berman, P. R.: *Cavity Quantum Electrodynamics.* Ed. Academic Press, San Diego, 1994.

[BGI89] Braginsky, V. B.; Gorodetsky, M. L.; Ilchenko, V. S.: Quality-factor and nonlinear properties of optical whispering-gallery modes. In: *Physics Letters A*, volume 137(7):pp. 393–397, 1989.

[BH98] Bohren, C.F.; Huffman, D.R.: *Absorption and Scattering of Light by Small Particles.* Wiley Science, Paperback Series, 1998.

[BHA+05] Badolato, Antonio; Hennessy, Kevin; Atatüre, Mete; Dreiser, Jan; Hu, Evelyn; Petroff, P. M.; Imamoglu, Atac: Deterministic coupling of single quantum dots to single nanocavity modes. In: *Science*, volume 308:pp. 1158–1161, 2005.

[BK03] Buck, J. R.; Kimble, H. J.: Optimal sizes of dielectric microspheres for cavity QED with strong coupling. In: *Phys. Rev. A*, volume 67:p. 033806, 2003.

[BKB+01] Balistreri, M. L. M.; Klunder, D. J. W.; Blom, F. C.; Driessen, A.; Korterik, J. P.; Kuipers, L.; van Hulst, N. F.: Experimental analysis of the whispering-gallery modes in a cylindrical optical microcavity. In: *J. Opt. Soc. Am. B*, volume 18(4):pp. 465–471, 2001.

[Boy92] Boyd, R.W.: *Nonlinear Optics.* Academic Press Inc., 1992.

[BS91] Bronstein, I. N.; Semendjajew, K. A.: *Taschenbuch der Mathematik.* Teubner Verlagsgesellschaft, Stuttgart, 25th edition, 1991.

[BT92] Betzig, E.; Trautman, J. K.: Near-field optics: microscopy, spectroscopy and surface modification beyond the diffration limit. In: *Science*, volume 257:pp. 189–195, 1992.

[BW64] Born, M.; Wolf, E.: *Principles of Optics.* Pergamon Press, 1964.

[CBB94] Courjon, D.; Bainier, C.; Baida, F.: Seeing inside a fabry-perot resonator by means of a scanning tunneling optical microscope. In: *Optics Communications*, volume 110:pp. 7–12, 1994.

[Che87] Chew, H.: Transition rates of atoms near spherical surfaces. In: *J. of Chem. Phys.*, volume 87(2):pp. 1355–1360, 1987.

[CMA$^+$01] Choi, Y.-S.; Moon, H. J.; An, K.; Lee, S.-B.; Lee, J.-H.; Chang, J.-S.: Ultrahigh-Q microsphere dye laser based on evanescent-wave coupling. In: *Journal of the Korean Physical Society*, volume 39(5):pp. 928–931, 2001.

[CMD72] Carniglia, C. K.; Mandel, L.; Drexhage, K. H.: Absoption and emission of evanescent photons. In: *Journal of the Optical Society of America*, volume 62(4):pp. 479–486, 1972.

[Col94] Collot, L.: *Etude théorique et expérimentale des résonances de galerie de microsphère de silice: pièges à photons pour des expériences délectrodynamique en cavité.* Ph.D. thesis, Laboratoir Kastler Brossel de l'École Normale Supérieur, Paris, 1994.

[CPS75] Chance, R.R.; Prock, A.; Silbey, R.: Frequency shifts of an electric dipole treansition near a partially reflecting surface. In: *Phys. Rev. A*, volume 12(4):pp. 1448–1492, 1975.

[CPV00] Cai, M.; Painter, O.; Vahala, K.: Observation of critical coupling in a fiber taper to a silica-microsphere whispering-gallery mode system. In: *Phys. Rev. Lett.*, volume 85:pp. 74–77, 2000.

[DKL$^+$95] Dubreuil, N.; Knight, J. C.; Leventhal, D. K.; Sandoghdar, V.; Hare, J.; Lefèvre, V.: Eroded monomode optical fiber for whispering-gallery mode excitation in fused-silica microspheres. In: *Optics Letters*, volume 20(8):pp. 813–815, 1995.

[Dre70] Drexhage: Influence of a dielectric interface on fluorescence decay time. In: *J. of Lum.*, volume 1(2):pp. 693–701, 1970.

[F̈65] Förster, T.: *Modern Quantum Chemistry, Vol. III (O. Sinanoglu, ed.) 93-137.* Academic Press, N.Y., 1965.

[FLW99] Fan, X.; Lacey, S.; Wang, H.: Microcavities combining a semiconductor with a fused-silica microsphere. In: *Optics Letters*, volume 24(11):pp. 771–773, 1999.

[GBS01] Götzinger, S.; Benson, O.; Sandoghdar, V.: Towards controlled coupling between a high-q whispering-gallery mode and a single nanoparticle. In: *Appl. Phys. B*, volume 73(8):pp. 825–828, 2001.

[GBS02] Götzinger, S.; Benson, O.; Sandoghdar, V.: Influence of a sharp fiber tip on high-q modes of a microsphere resonator. In: *Opt. Lett.*, volume 27(2):pp. 80–82, 2002.

[GC97] Greffet, J.-J.; Carminati, R.: Image formation in near-field optics. In: *Progress in Surface Science*, volume 56(3):pp. 133–237, 1997.

[GDBS01] Götzinger, S.; Demmerer, S.; Benson, O.; Sandoghdar, V.: Mapping and manipulating whispering-gallery modes of a microsphere resonator with a near-field probe. In: *J. Microsc.*, volume 202(1):pp. 117–121, 2001.

[GdSMM$^+$03] Götzinger, S.; de S. Menezes, L.; Mazzei, A.; Benson, O.; Talapin, D.V.; Gaponik, N.; Weller, H.; Rogach, A.L.; Sandoghdar, V.: Controlled coupling of a single emitter to a single mode of a microsphere: where do we stand? In: *Proc. SPIE*, volume 207:pp. 4969–4977, 2003.

[Ger96] Gerard, J. M.: Quantum boxes as active probes for photonic microstructures: The pillar microcavity case. In: *Appl. Phys. Lett*, volume 69:pp. 449–451, 1996.

[GI94a] Gorodetsky, M. L.; Ilchenko, V. S.: High-q optical whispering-gallery microresonators: precession approach for spherical mode analysis and emission patterns with prism couplers. In: *Optics Communications*, volume 113:pp. 133–143, 1994.

[GI94b] Gorodetsky, M.L.; Ilchenko, V.S.: High-q optical whispering-gallery microresonators: precession approach for spherical mode analysis and emission patterns with prism couplers. In: *J. Opt, Soc. Am. A*, volume 113:pp. 133–143, 1994.

[GI99] Gorodetsky, M. L.; Ilchenko, V. S.: Optical microsphere resonators: optimal coupling to high-Q whispering-gallery modes. In: *Journal of the Optical Society of America B*, volume 16(1):pp. 147–154, 1999.

[GKHW01] Guthöhrlein, G. R.; Keller, M.; Hayasaka, K.; Walther, W. Langem H.: A single ion as a nanoscopic probe of an optical field. In: *Nature*, volume 414:pp. 49–51, 2001.

[GKL61] Garret, C. G. B.; Kaiser, W.; Long, W. L.: Stimulated emission into optical whispering modes of spheres. In: *Phys. Rev.*, volume 124:pp. 1807–1809, 1961.

[GM06] Grudinin, I. S.; Maleki, L.: Ultralow-threshold raman lasing with caf2 resonators. In: *Opt. Lett.*, volume 32(2):p. 166, 2006.

[GMS$^+$06] Grudinin, I. S.; Matsko, A. B.; Savchenkov, A. A.; Strekalov, D.; Ilchenko, V. S.; Maleki, L.: Ultra high-q crystalline microcavities. In: *Opt. Comm.*, volume 265:p. 33, 2006.

[Göt04] Götzinger, S.: *Controlled Coupling of a Single Nanoparticle to a High-Q Microsphere Resonator.* Logos Verlag, 2004.

[GPI00] Gorodetsky, M. L.; Pryamikov, A. D.; Ilchenko, V. S.: Rayleigh scattering in high-q microspheres. In: *J. Opt. Soc. Am. B*, volume 17(6):pp. 1051–1057, 2000.

[GRGH83] Goy, P.; Raimond, J. M.; Gross, M.; Haroche, S.: Observation of cavity-enhanced single-atom sponaneous emission. In: *Physical Review Letters*, volume 50(24):pp. 1903–1906, 1983.

[Hau84] Haus, H: *Waves and fields in Optoelectronics.* Prentice-Hall, Englewood Cliffs, 1984.

[HMK04] Höhberger-Metzger, C.; Karrai, K.: Cavity cooling of a microlever. In: *Nature*, volume 432:pp. 1002–1005, 2004.

[IYM99] Ilchenko, V.S.; Yao, X.S.; Maleki, L.: Pigtailing the high-q microsphere cavity: a simple fibercoupler for optical whispering-gallery modes. In: *Opt. Lett.*, volume 24(11):pp. 723–725, 1999.

[Jac89] Jackson, J.D.: *Classical Electrodynamics.* Jhon Wiley and Sons, 1989.

[Kal02] Kalkbrenner, T.: *Charakterisierung und Manipulation der Plasmon-Resonanz eines einzelnen Gold-Nanoparticles.* Dissertation, Universität Konstanz, 2002.

[KCJB97] Knight, J.C.; Cheung, G.; Jacques, F.; Birks, T.A.: Phase-matched excitation of whispering-gallery mode resonances by a fibertaper. In: *Opt. Lett.*, volume 22(15):pp. 1129–1131, 1997.

[KDL96] Klimov, V.V.; Ducloy, M.; Letokhov, V.S.: Radiative frequency shift and linewidth of an atom dipole in the vicinity of a dielectric microsphere. In: *J. Modern Opt.*, volume 43(11):pp. 2251–2267, 1996.

[KDS+95] Knight, J.C.; Dubreil, N.; Sandoghdar, V.; Hare, J.; Lefévre-Seguin, V.: Mapping whispering-gallery modes in microspheres with a near-field probe. In: *Opt. Lett.*, volume 20(14):pp. 1515–1517, 1995.

[KHS+01] Kühn, S.; Hettich, C.; Schmitt, C.; Poizat, J.-Ph.; Sandoghdar, V.: Diamond color centres as a nanoscopic light source for scanning near-field optical microscopy. In: *Journal of Microscopy*, volume 202:pp. 2–6, 2001.

[Kle81] Kleppner, D.: Inhibited spontaneous emission. In: *Phys. Rev. Lett.*, volume 47(4):pp. 233–236, 1981.

[KLNH06] Klinner, J.; Lindholt, M.; Nagorny, B.; Hemmerich, A.: Normal mode splitting and mechanical effects of an optical lattice in a ring cavity. In: *Phys. Rev. Lett.*, volume 96:pp. 23002–23005, 2006.

[Kra05] Krauter, Hanna: *Diplomarbeit - Ramanlasing in einem Mikrokugelresonator*. Humboldt Universität zu Berlin, 2005.

[Kru87] Krug, Joachim: Optical analog of a kicked quantum oscillator. In: *Phys. Rev, Lett.*, volume 59(19):pp. 2133–2136, 1987.

[KSM+04] Kippenberg, T. J.; Spillane, S. M.; Min, Bumki; ; Vahala, K. J.: Theoretical and experimental study of stimulated and cascaded raman scattering in ultrahigh-q optical microcavities. In: *IEEE Journal of selected topics in quantum electronics*, volume 10(5):pp. 1219–1228, 2004.

[KSV02] Kippenberg, T.J.; Spillane, S.M.; Vahala, K.J.: Modal coupling in travelling wave resonators. In: *Opt. Lett.*, volume 27(9):pp. 1669–1671, 2002.

[LHEC90] Lin, H. B.; Huston, A. L.; Eversol, J. D.; Campillo, A. J.: Double-resonance stimulated raman scattering in micrometer-sized droplets. In: *J. Opt. Soc. Am. B*, volume 7:pp. 2079–2089, 1990.

[LIHM84] Lewis, A.; Isaacson, M.; Harootunian, A.; Muray, A.: Development of a 500 A spatial resolution light microscope. In: *Ultramicroscopy*, volume 13(3):pp. 227–231, 1984.

[LK77] Lukosz, W.; Kunz, R. E.: Light emission by magnetic and electric dipoles close to a plane interface. i. total radiated power. In: *J. Opt. Soc. Am.*, volume 67:p. 1607, 1977.

[LLL+00] Little, B. E.; Laine, J.-P.; Lim, D. R.; Haus, H. A.; Kimerling, L. C.; Chu, S. T.: Pedestal antiresonant reflecting waveguides for robust coupling to microsphere resonators and for microphotonic circuits. In: *Optics Letters*, volume 25(1):pp. 273–75, 2000.

[LMSF01] Lissillour, F.; Messager, D.; Stéphan, G.; Féron, P.: Whispering-gallery mode laser at 1.56 m m excited by a fiber taper. In: *Opt. Lett.*, volume 26(14):pp. 1051–1053, 2001.

[LWFN03] Lacey, S.; Wang, H.; Foster, D.H.; Nöckel, J.U.: Directional tunneling escape from nearly spherical optical resonators. In: *Phys. Rev. Lett.*, volume 91:pp. 033902–033905, 2003.

[MHMS00] Michaelis, J.; Hettich, C.; Mlynek, J.; Sandoghdar, V.: Optical microscopy using a single-molecule light source. In: *Nature*, volume 405:pp. 325–328, 2000.

[MI98] Meystre, P.; III, M. Sargent: *Elements of Quantum Optics*. Springer Verlag, 1998.

[Mie08] Mie, G.: Beiträge zur Optik trüber Medien, speziell kolloidaler Metalllösungen. In: *Annalen der Physik*, volume 25(4):pp. 377–445, 1908.

[MKB+00] Michler, P.; Kiraz, A.; Becher, C.; Schoenfeld, W. V.; Petroff, P. M.; Zhang, Lidong; Hu, E.; Imamoglu, A.: A quantum dot single photon turnstile device. In: *Science*, volume 290:pp. 2282–2285, 2000.

[MLS+91] McCall, S. L.; Levi, A. F. J.; Slusher, R. E.; Pearton, S. J.; Logan, R. A.: Whispering-gallery mode microdisk lasers. In: *Appl. Phys. Lett.*, volume 60(3):pp. 289–291, 1991.

[MPARaC01] Meng, L. S.; P. A. Roos and, K. S. Repasky; ; Carlsten, J. L.: High-conversion-efficiency, diode-pumped continuous-wave raman laser. In: *Opt. Lett.*, volume 26(7):pp. 426–429, 2001.

[MWM85] Meschede, D.; Walther, H.; Muller, G.: One-atom maser. In: *Phys. Rev. Lett.*, volume 54:pp. 551–554, 1985.

[NKR$^+$04] Nobis, T.; Kaidashev, E.M.; Rahm, A.; Lorenz, M.; Grundmann, M.: Whispering-gallery modes in nanosized dielectric resonators with hexagonal cross section. In: *Physical Review Letters*, volume 93(10):pp. 103903–103906, 2004.

[Oht98] Ohtsu, M.: *Near-Field Nano/Atom Optics and Technology.* Springer Verlag Tokyo,, 1998.

[Paw95] Pawley, J.B.: *handbook of confocal biological microscopy.* Plenum Press, New York, 1995.

[PC03] Pan, Yong-Le; Chang, R.K.: Highly efficient prism coupling to whispering gallery modes of a square μ-cavity. In: *Appl. Phys. Lett.*, volume 82(4):pp. 487–489, 2003.

[PDL84] Pohl, D. W.; Denk, W.; Lanz, M.: Optical stethoscopy: Image recording with resolution $\lambda/20$. In: *Appl. Phys. Lett.*, volume 44(7):pp. 651–653, 1984.

[PF89] Prange, R.E.; Fishman, S.: Experimental realizations of kicked quantum chaotic systems. In: *Phys. Rev. Lett.*, volume 63:pp. 704–707, 1989.

[PSM$^+$05] Peter, E.; Senellart, P.; Martrou, D.; Lemaitre, A.; Hours, J.; Gerard, J. M.; ; Bloch, J.: Exciton-photon strong-coupling regime for a single quantum dot embedded in a microcavity. In: *Phys. Rev. Lett.*, volume 95:pp. 067401–067404, 2005.

[Pur46] Purcell, E. M.: Spontaneous emission probabilities at radio frequencies. In: *Phys. Rev.*, volume 69:p. 681, 1946.

[PVZ$^+$02] Pelton, M.; Vuckovic, C. Santoriand J.; Zhang, B.; Solomon, G. S.; Plant, J.; Yamamoto, Y.: Efficient source of single phtons: a single quantum dot in a micropost microcavity. In: *Phys. Rev. Lett.*, volume 89:pp. 233602–233605, 2002.

[PY99] Pelton, M.; Yamamoto, Y.: Ultralow threshold laser using a single quantum dot and a microsphere cavity. In: *Phys. Rev. A*, volume 59(3):pp. 2418–2421, 1999.

[PZH$^+$04] Pfab, R.J.; Zimmermann, J.; Hettich, C.; Gerhardt, I.; Renn, A.; Sandoghdar, V.: Aligned terrylene molecules in a spin-coated ultrathin crystalline film of p-terphenyl. In: *Chem. Phys. Lett.*, volume 387:pp. 490–495, 2004.

[QC86] Qian, S.-X.; Chang, R. K.: Multiorder stokes emission from micrometer-size droplets. In: *Phys. Rev. Lett.*, volume 56(9):pp. 926–929, 1986.

[QPW99] Quinten, M.; Pack, A.; Wannemacher, R.: Scattering and extinction of evanescent waves by small particles. In: *Appl. Phys. B*, volume 68:pp. 87–92, 1999.

[RA96] R.K.Chang; A.J.Campillo: *Optical Processes in Microcovities.* World Scientific Press, Singapore, 1996.

[Ray78] Rayleigh, J.W.S.: *Theory of sound.* Macmillan and co., 1878.

[Ray10] Rayleigh, J.W.S.: The problem of the whispering gallery. In: *Phylosophical magazine*, volume XX:pp. 1001–1004, 1910.

[RK28] Raman, C. V.; Krishnan, K. S.: Temporal behavior of radiation-pressure-induced vibrations of an optical microcavity phonon mode. In: *Phys. Rev.*, volume 121:pp. 3048–3051, 1928.

[R.R82] R.Ruppin: Decay of an excited molecule near a small metal sphere. In: *J. Chem Phys.*, volume 76(4):pp. 1681–1684, 1982.

[RSL$^+$04] Reithmaier, J.R.; Sek, G.; Löffler, A.; Hoffmann, C.; Kuhn, S.; Reitzenstein, S.; Keldysh, L. V.; Reinecke, T. L.; Forchel, A.: Strong coupling in a single quantum dot-semiconductor microcavity system. In: *Nature*, volume 432:pp. 197–199, 2004.

[RTB$^+$91] Rempe, G.; Thompson, R. J.; Brecha, R. J.; Lee, W. D.; Kimble, H. J.: Optical bistability and photon statistics in Cavity Quantum Electrodynamics. In: *Phys. Rev. Lett.*, volume 67(13):pp. 1727–1730, 1991.

[SB91] Schiller, S.; Byer, R. L.: High-resolution spectroscopy of whispering-gallery modes in large dielectric spheres. In: *Optics Letters*, volume 16(15):pp. 1138–1140, 1991.

[Sch93] Schiller, S.: Asymptotic expansion of morphological resonance frequencies in Mie scattering. In: *Appl. Optics*, volume 32(12):pp. 2181–2185, 1993.

[SK89] S.Haroche; Kleppner, D.: Cavity quantum electrodynamics. In: *Phys. Today*, volume 42(1):p. 24, 1989.

[SKV02] Spillane, S.M.; Kippenberg, T.J.; Vahala, K.J.: Ultralow-threshold raman laser using a spherical dielectric microcavity. In: *Nature*, volume 415(6872):pp. 621–623, 2002.

[SP06] Srinivasan, K.; Painter, O.: Mode coupling and cavity-quantum-dot interactions in a fiber-coupled microdisk cavity. In: *quant-ph/0606142*, 2006.

[SPY00] Solomon, G.S.; Pelton, M.; Yamamoto, Y.: Modification of spontaneous emission of a single quantum dot. In: *Phys. Status Solidi*, volume 178:pp. 341–344, 2000.

[SPY01] Solomon, G. S.; Pelton, M.; Yamamoto, Y.: Single-mode spontaneous emission from a single quantum dot in a three-dimensional microcavity. In: *Phys. Rev. Lett.*, volume 86:pp. 3903–3906, 2001.

[STH+96] Sandoghdar, V.; Treussart, F.; Hare, J.; Lefèvre-Seguin, V.; Raimond, J.-M.; Haroche, S.: Very low threshold whispering-gallery mode microsphere laser. In: *Physical Review A*, volume 54(3):pp. R1777–R1780, 1996.

[Sto89] Stolen: Raman response function of silica-core fibers. In: *J. Opt. Soc. Am. B*, volume 6:pp. 1159–1161, 1989.

[SvDEW90] Spreeuw, R. J. C.; van Druten, R. Centeno Neelenand N. J.; Eliel, E. R.; Woerdman, J. P.: Mode coupling in a he-ne ring laser with backscattering. In: *Phys. Rev. A*, volume 42:pp. 4315–4324, 1990.

[SW91] Spreeuw, R. J. C.; Woerdman, J. P.: The driven optical ring resonator as a model system for quantum optics. In: *Physica B*, volume 1752:pp. 96–110, 1991.

[Tew74] Tews, K. H.: On the variation of luminescence lifetimes. the approximations of the approximative methods. In: *J. of Lum.*, volume 9(3):pp. 223–239, 1974.

[TGR$^+$06] Tamarat, Ph.; Gaebel, T.; Rabeau, J. R.; Khan, M.; Greentree, A. D.; Wilson, H.; Hollenberg, L. C. L.; Prawer, S.; Hemmer, P.; Jelezko, F.; Wrachtrup, J.: Stark shift control of single optical centers in diamond. In: *J. Opt. Soc. Am. B*, volume 97:pp. 83002–83005, 2006.

[VFG$^+$98] Vernooy, D. W.; Furusawa, A.; Georgiades, N. Ph.; Ilchenko, V. S.; Kimble, H. J.: Cavity qed with high-q whispering-gallery modes. In: *Physical Review A*, volume 57(4):pp. R2293–R2296, 1998.

[VLMS01] Vuckovic, Jelena; Loncar, Marko; Mabuchi, Hideo; Scherer, Axel: Design of photonic crystal microcavities for cavity qed. In: *Phys. Rev. E*, volume 65:pp. 16608–016618, 2001.

[VY03] Vuckovic, Jelena; Yamamoto, Y.: Photonic crystal microcavities for cavity quantum electrodynamics with a single quantum dot. In: *Appl. Phys. Lett.*, volume 82(15):pp. 2374–2376, 2003.

[Web96] Webb, R. H.: Confocal optical microscopy. In: *Reports on Progress in Physics*, volume 59:pp. 427–471, 1996.

[WSH$^+$95] Weiss, D. S.; Sandoghdar, V.; Hare, J.; V. Lefèvre-Seguin, J.-M. Raimond; Haroche, S.: Splitting of high-q mie modes induced by light backscattering in silica microspheres. In: *Optics Letters*, volume 20(18):pp. 1835–1837, 1995.

[YSH$^+$04] Yoshie, T.; Scherer, A.; Hendrickson, J.; Khitrova, G.; Gibbs, H.; Rupper, G.; Ell, C.; Schenkin, Q.; ; Deppe, D.: Vacuum rabi splitting with a single quantum dot in a photonic crystal nanocavity. In: *Nature*, volume 432:pp. 200–203, 2004.

[YU85] Yokoyama, H.; Ujihara, K.: *Spontaneous Emission and Laser Oscillation in MicrocaVities.* CRC Press: Boca Raton, 1985.

[ZC90] Zhang, J. Z.; Chang, R. K.: Double-resonance stimulated raman scattering in micrometer-sized droplets. In: *J. Opt. Soc. Am. B*, volume 7:pp. 2079–2089, 1990.

[ZMW95] Zenhausern, F.; Martin, Y.; Wickramasinghe, H. K.: Scanning interferometric apertureless microscopy: Optical imaging at 10 Angstrøm resolution. In: *Science*, volume 269:pp. 1083–1086, 1995.

Danksagung

So finally the end! And it would never be a respectable end without thanking all the people who supported and helped me in these years: without them this work would have never been possible.

First of all I would like to thank Prof. Dr. Oliver Benson for giving me the opportunity to work in his group. His tutorship was extremely helpful in all these years, and I can say that without his help many of the problem that had to be faced, would not have found a solution.

Stephan Götzinger will remain in my heart as the father of the experiment. His "pfälzische" precision was a very good example for the experimental work. Thanks to him, I've learned never to trust the experimental results, and to measure everything twice!

Leonardo Menezes was a great motivator. Not only his knowledge in nonlinear optics, but also his creativity and perseverance made everyday life in the lab much more interesting. His ability to keep in touch Berlin with Recife was and will be really helpful for this experiment.

A thank you goes also to Prof. Dr. Vahid Sandoghdar. He kept interesting himself for the experiments, and I was always welcomed in Zürich whenever I had questions and problems. A thank you goes also to Ilja and Robert, who answered all my obsessive questions with a lot of patience.

I sure can say that in the berliner laboratory I've met not only colleagues, but also friends. My life here was definitely influenced by the Pfalz: through Stefan Schietinger I've got to know the front side of the Pfalz, and together we repeatedly explored the south side of Hausvogteiplatz. He also let me use his setup to pick up the small stuff, or to do this and that whenever I wanted. Thomas Aichele taught me how to think "schwäbisch" - and how to cook the best Käsespätzle! The Pascal knowledge of Matthias Scholz was essential to solve some cumbersome problems!

Diplom Ingenieur Klaus Palis was always there, and his help has been determinant for the success of the experiments. Dr. Gerd Zumofen at the ETH Zürich contributed consistently to the understanding of scattering problems in microcavities.

Holger always found the right words to say whenever I was frustrated or depressed. His presence was very special in these years. Through this work I came to know a very special person, Nina, who found the time to read and correct my very Italian English! A big thank you goes to all the people of Hausvogteiplatz, who contributed to create a really pleasant working environment, not only during the coffee breaks. Finally, I should really thank my family, who always took care of me, providing from time to time that special Italian touch in my life during these years in Berlin.

Grazie!!!

Selbständigkeitserklärung

Hiermit erkläre ich, die vorliegende Arbeit selbständig ohne fremde Hilfe verfasst und nur die angegebene Literatur und Hilfsmittel verwendet zu haben.

Ich habe mich anderwärts nicht um einen Doktorgrad beworben und besitze einen entsprechenden Doktorgrad nicht.

Ich erkläre die Kenntnisnahme der dem Verfahren zugrunde liegenden Promotionsordnung der Mathematisch-Naturwissenschaftlichen Fakultät I der Humboldt-Universität zu Berlin.

Berlin, den

Andrea Mazzei